ANL-6099
Metallurgy and Ceramics
(TID-4500, 15th Ed.)
AEC Research and
Development Report

ARGONNE NATIONAL LABORATORY
9700 S. Cass Avenue
Argonne, Illinois

ANNUAL REPORT FOR 1959

METALLURGY DIVISION

Frank G. Foote, Director
James F. Schumar, Associate Director
Haim H. Chiswik, Associate Director

Previous Annual Report:

Annual Report for 1958 ANL-5975

Operated by The University of Chicago
under
Contract W-31-109-eng-38

DISCLAIMER

This report was prepared as an account of work sponsored by an agency of the United States Government. Neither the United States Government nor any agency Thereof, nor any of their employees, makes any warranty, express or implied, or assumes any legal liability or responsibility for the accuracy, completeness, or usefulness of any information, apparatus, product, or process disclosed, or represents that its use would not infringe privately owned rights. Reference herein to any specific commercial product, process, or service by trade name, trademark, manufacturer, or otherwise does not necessarily constitute or imply its endorsement, recommendation, or favoring by the United States Government or any agency thereof. The views and opinions of authors expressed herein do not necessarily state or reflect those of the United States Government or any agency thereof.

DISCLAIMER

Portions of this document may be illegible in electronic image products. Images are produced from the best available original document.

FOREWORD

This report summarizes the major activities of the Metallurgy Division during the calendar year 1959. Following the procedure adopted in the 1958 annual report, work that has been published during the year in either papers in regular technical journals or in topical ANL reports is discussed only briefly in this annual summary report; for details the reader should refer to the original publications, which are listed in Appendix B. The status of programs still in progress is discussed in greater detail.

TABLE OF CONTENTS

	Page
FOREWORD	2
PART I - ENGINEERING METALLURGY	
A. Development Programs for EBR-II	9
1. Fuel Materials	9
2. Development of Processes and Equipment for the Refabrication of Irradiated Fuel	12
3. Development of Welding Processes for Fuel Core Components	17
4. Fabrication of Fuel Elements for First Loading	19
5. Fabrication of Blanket Rods	20
6. Development of Steam Generator and Superheater	26
7. Delayed Neutron Control Rods	28
B. Fabrication of Core and Blanket Components for the Argonne Fast Source Reactor (AFSR)	29
C. Fabrication of Spiked Fuel Rods for EBWR (Core 1A)	32
D. Fuel for TREAT Reactor	33
E. Fuel Elements for EBR-I (Mark-IV)	34
1. Experimental Pu-1 w/o Al Zircaloy-clad Elements	34
2. Development of Fabrication Methods	34
F. Canning of Plutonium Loading for ZPR-III	35
G. Development of Ceramic Fuel Materials	36
1. Uranium and Plutonium Monocarbides	36
2. Urania-Thoria	37
3. ZrO_2-CaO-UO_2	38
4. Uranium Sulfides	42
H. Irradiation Evaluations of Various Experimental Fuel and Control Rod Materials	43
I. Postirradiation Examinations of Full-scale Reactor Fuel Elements	45

TABLE OF CONTENTS

Page

J. Development of Corrosion-resistant Fuel and Jacketing Materials 47

1. High-temperature Corrosion-resistant Aluminum Alloys. 47
2. Uranium Alloys 52
3. Zirconium Alloys for Use in Superheated Steam 53
4. Structural Materials in Acid Environments 53

K. Nondestructive Testing Developments 55

1. Instrumentation for Elastic Constants Measurements. . . . 55
2. Cladding Thickness Measurements. 55
3. Eddy Current Studies. 55

L. Metallurgical Assistance to the Fast Reactor Safety Program . . 56

M. Miscellaneous Developments 59

1. Brazing Alloy for Zirconium. 59
2. Brazed End Closures for CP-5 Core 59
3. Calorimetric Assay of Plutonium-containing Specimens. . 59

PART II - BASIC METALLURGY

A. Preparation of High-purity Materials. 63

1. Plutonium 63
2. Uranium 67

B. Physical Metallurgy of Uranium 68

1. Plastic Deformation of Single Crystals at Elevated Temperatures 68
2. Recrystallization Textures in Deformed Single Crystals. . 68
3. Recrystallization of Room-temperature-rolled Sheet. . . . 69
4. Some Aspects of the Beta to Alpha Phase Transformation 71

C. Uranium and Plutonium Alloys: Constitution and Properties . . . 72

1. Uranium-Carbon. 72
2. Uranium-Niobium-Zirconium 72
3. Uranium-Fissium 73
4. Phase Diagrams of Plutonium with Fissium Elements . . . 75

TABLE OF CONTENTS

Page

D. Alloying Properties 76

1. Studies on Transition Metal Intermediate Phases 76
2. Occurrence and Magnetic Properties of C8 and Sigma Phases. 92
3. Occurrence of the CsCl-Type Structure in Transition Element Alloys. 94
4. Calorimetric Studies of Intermetallic Compounds of Transition Elements. 96

E. X-ray and Neutron Diffraction Studies 97

1. Magnetic Structure of $(Mn,Co)_4C$ 97
2. Diffraction of Neutrons by Krypton in the Liquid State . . . 97
3. Neutron Coherent Scattering Amplitudes 98
4. Structure of Alkali Metals in the Liquid State. 99
5. The Urania-Thoria System 99
6. Neutron Diffraction Spectrometer. 100
7. High-temperature X-ray Diffraction Furnace. 101

F. Problems in Metal Physics. 102

1. Studies on Diffusion in Anisotropic Metals. 102
2. Elastic Moduli 105
3. Theoretical Studies on the Temperature Dependence of Elastic Moduli. 112
4. Interactions of Interstitial Solute Atoms with Dislocations. 116

G. Corrosion Research 118

1. Polarization in Distilled Water 118
2. Corrosion Mechanism of Zirconium 118
3. The Corrosion of 1100 Aluminum in Water. 122
4. Corrosion Film Studies by Electron Microscopy and Diffraction 124

H. Irradiation Effects 136

1. Power Distribution in Uranium Specimens under Irradiation. 136
2. Effect of Irradiation on Phase Transformations 137
3. Fission Gas Research 138
4. Effect of Neutron Irradiation on the Thermoelectric emf and Electrical Resistivity of Metals and Alloys. 139

TABLE OF CONTENTS

Page

I. Ceramic Materials Research 144

1. Sintering Mechanisms of Al_2O_3 Single Crystals. 144
2. Evaporation of Al_2O_3 Single Crystal Spheres in Dry Hydrogen. 145
3. Sintering Mechanisms in Nonstoichiometric Oxides. 147
4. Mechanism of Solid-Gas Reactions. 148
5. Metallographic Techniques for Ceramic Materials 151

APPENDIX A - METALLURGICAL FACILITIES CONSTRUCTION PROJECTS. 153

APPENDIX B - PUBLICATIONS AND REPORTS JANUARY 1, 1959 - DECEMBER 31, 1959. 163

PART I

ENGINEERING METALLURGY

A. Development Programs for EBR-II

1. Fuel Materials

The reference fuel material for the first core loading of the EBR-II is an uranium-5 w/o fissium alloy. For the second loading, the fuel material is an uranium-20 w/o plutonium-10 w/o fissium alloy. Most of the development work on fuel materials for this reactor was centered, therefore, during the past year on alloys bracketing these compositions.

Properties of Uranium-Plutonium-Fissium Alloys (O. L. Kruger)

Hardness data, densities, and solidus temperatures of various arc melted uranium-20 w/o plutonium-fissium alloys are summarized in Table I. The densities and solidus temperatures decrease with increasing fissium concentrations. The substitution of zirconium for an equivalent amount of fissium results in a further decrease in density. The solidus temperatures were determined by metallographic techniques on specimens that were homogenized and held at various temperatures for one-half hour and quenched in NaK. Metallographic examination of the 65 w/o uranium-20 w/o plutonium-15 w/o fissium alloy indicated the presence of appreciable amounts of zeta phase.

TABLE I

Properties of Uranium-20 w/o Plutonium-Fissium Alloys

Composition (w/o)	Hardness (R_A)	Density (g/cc) (Room Temp)	Solidus Temperature (°C)
75 U-20 Pu-5 Fs	75	17.86 ± 0.02	860 ± 10
70 U-20 Pu-10 Fs	95	17.03 ± 0.02	820 ± 10
65 U-20 Pu-15 Fs	76	16 38 ± 0.02	800 ± 10
75 U-20 Pu-3.5 Fs-1.5 Zr	84	17.72 ± 0.02	-
70 U-20 Pu-7 Fs-3 Zr	75	16.84 ± 0.02	-
65 U-20 Pu-10.5 Fs-4.5 Zr	73	16.14 ± 0.02	-

Compatibility of Uranium-Plutonium-Fissium Alloys with Various Canning Materials (J. J. Huet)

A program has been initiated to determine the compatibility of various canning materials with the EBR-II uranium-20 w/o plutonium-10 w/o fissium reference alloy under the thermal conditions anticipated in the reactor. The materials under study include stainless steel Types 347

and 430, zirconium, Zircaloy-2, molybdenum, titanium, tantalum, niobium, and vanadium. The experiments involve diffusion penetration studies in couples of these materials with the reference fuel alloy. Two temperature levels have been tested, 800 and 700°C, for periods of 3, 10, and 30 days. Measurements at 600°C are now in progress for periods of 10, 30, and 60 days. The diffusion anneals are carried out in the helium glovebox atmosphere.

Plots of the log of the width of the diffusion bands, X, versus the log of the time, t, yielded straight lines of the form $X^2 = kt$, where k is a constant. Mean penetration coefficients deduced from these plots were as follows (units: 10^{-12} cm^2/sec):

Canning Material	694°C	794°C
430 Stainless Steel	Molten eutectic formed	Molten eutectic formed
347 Stainless Steel	Molten eutectic formed	Molten eutectic formed
Zirconium	10.76	1239
Zircaloy-2	5.43	640.1
Niobium	16.81	125.8
Tantalum	No diffusion visible	190.7
Titanium	2.71	42.25
Molybdenum	3.24	24.11
Vanadium	No bonding	No bonding

None of the vanadium couples bonded successfully; work at Nuclear Metals[1] indicates that hot pressure bonding in a vacuum would probably give good results.

The stainless steel couples formed a molten eutectic at both 794 and 694°C; this also occurred at lower temperatures. Couples with stainless steel are currently being run at 500, 550, and 600°C to determine the lower temperature limit of eutectic formation.

The diffusion band in the tantalum was visible only in the 794°C couple; at 700 and 600°C, even when the bond was very good, no diffusion was visible. The diffusion is almost entirely on the tantalum side, and the interface between the fuel alloy and the diffusion bond is very weak and brittle. The couple broke at this interface during disassembly and mounting processes.

The couple with the niobium made a very strong bond which did not break during handling and polishing. The diffusion is more than 90% on the niobium side.

---

[1] S. H. Gelles and R. G. Jenkins, NMI-4812 (1959).

The couples with the zirconium and Zircaloy-2 were very similar, the diffusion band with the Zircaloy being approximately 2/3 in width that obtained in the iodide zirconium. The diffusion is more than 95% on the zirconium side. At 800°C, three different bands were present, the one on the zirconium side being about ten times as wide as the two others combined. At 700 and 600°C, the two bands on the zirconium side were roughly equal and the boundary between them very irregular. Some cracks showed evidence of the brittleness of the band on the fuel alloy side.

The titanium diffusion was almost entirely on the titanium side; it consisted of three distinct bands, the middle one being smaller and very irregular.

Molybdenum formed only one band 80% of which was on the fuel alloy side. The band was very brittle and broke often during the handling and mounting; the break was on the fuel alloy interface as well as on the molybdenum interface.

Irradiation Behavior of Uranium-Fissium and Uranium-Plutonium-Fissium Alloys (J A Horak and J H Kittel)

Irradiations of a variety of uranium-fissium and uranium-plutonium-fissium alloys have continued with two objectives in mind (a) to determine the effect of variations in compositions of the alloys on irradiation behavior, and (b) to determine the operational limits of the alloys in terms of maximum burnup and irradiation temperature.

Irradiation studies have been made with cast uranium-fissium alloys containing from 3.3 to 10 w/o fissium, and from 1 7 to 5 w/o additional zirconium. All of the alloys have been found to display excellent stability under irradiation. The most stable compositions were those with higher fissium contents and extra zirconium. Specimens of the EBR-II Core 1 reference alloy, uranium-5 w/o fissium have often shown a small amount of anisotropic growth under irradiation Burnup and temperature limits for the alloys have not yet been definitely determined However, present results indicate that the two compositions of greatest interest, uranium-5 w/o fissium and uranium-5 w/o fissium-2.5 w/o zirconium, will satisfactorily withstand the EBR-II operating requirements of 2 a/o burnup at 700°C.

The addition of plutonium to uranium-fissium alloys has been found to decrease markedly the swelling resistance of the alloys Specimens of the reference composition for EBR-II Core 2, uranium-20 w/o plutonium-10 w/o fissium, have been found to swell excessively at temperatures as low as 400 - 450°C. The swelling characteristics of the alloy are not improved by replacing approximately one-third of the fissium with molybdenum or zirconium. A significant improvement was noted, however, when the plutonium content was decreased to 10 w/o

Thermal Cycling Behavior of Uranium-Fissium Alloys
(W. N. Beck)

The uranium-fissium fuel in EBR-II, as a consequence of reactor startup and shutdown, will undergo thermal cycling between temperatures of approximately 370 and 670°C. Since the alpha-gamma transformation of the Core 1 reference alloy is near 640°C, it is evident that the fuel will undergo repeated phase transformation during service. In order to determine possible dimensional changes, a series of thermal cycling experiments have been performed with the same group of uranium-fissium alloys used for irradiation experiments. Specimens of alloys containing from 3.3 to 10 w/o fissium and from 1.7 to 5 w/o additional zirconium have been cycled between 370 and 670°C. Holding times were 2 hours at 370°C and 1 hour at 670°C, with transfer times of 30 minutes. The long holding times were chosen to permit the alloy to fully transform to and from the gamma phase. Density and dimensional measurements of the specimens after intervals of 58, 150, 300, and 500 cycles showed that all compositions were fairly stable. After 500 cycles, length increases averaged 1 08%, not including an uranium-3.7 w/o fissium alloy specimen that elongated 3.84%. Density decreases after 500 cycles averaged 1.10%. These results indicate that thermal cycling of the fuel in EBR-II Core 1 will not be a serious operational problem.

2. Development of Processes and Equipment for the Refabrication of Irradiated Fuel (N. J Carson. H. F. Jelinek, J. E Ayer, and A. B. Shuck)

The feasibility of producing EBR-II-type fuel pins by a gas pressure, injection-casting process was demonstrated in 1958. During the past year a pilot-plant semiproduction facility was constructed and placed in operation in Building 6 for the dual purpose of fabricating the first EBR-II fuel loading and for testing remote control refabrication processes and equipment. A program of bench testing of component parts was required because of the need for "plug-in" subassemblies constructed of radiation-resistant, unlubricated machine parts The facility was declared operational in late August. It includes an injection-casting furnace; demolding, shearing and inspection equipment, an inert atmosphere glovebox line for fuel element assembly, sodium filling and welding; and a glovebox line housing decanning equipment. The inert atmosphere used is argon recirculated and purified by a DeOxo purifier - synthetic zeolite dryer - turboblower system. The equipment is installed below a General Mills manipulator used for testing remote control features requiring manipulator operation. A simulated shielding window and shielded periscope are used to simulate viewing conditions within the process cell. Remote control stations on the "cold" side of the window are used to operate the various movements of the equipment through electropneumatic controls. Inspection signals are transmitted to recorders at the operator's station. The operations carried out in this facility are shown in the flow diagram of Figure 1.

Figure 1

Flow Diagram of EBR-II Initial Fuel Fabrication

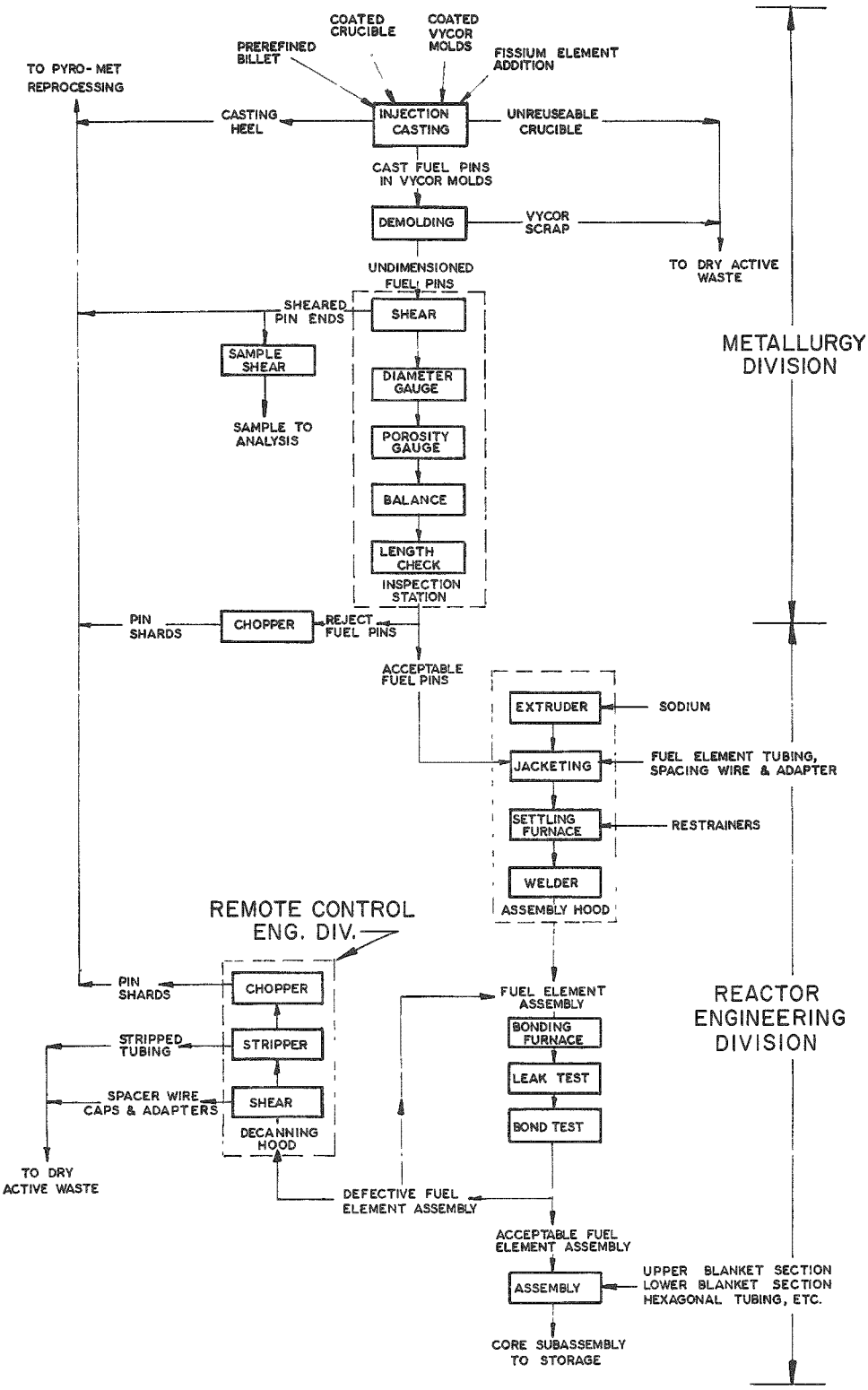

The equipment is very largely of new design and untested. It was not intended that this equipment be operated by full remote control, nor that it would be installed in the EBR-II Fuel Cycle Facility. The purpose of the equipment was to bridge the gap between the improved apparatus used to test process feasibility and the more refined remote control equipment for refabrication.

Process and Equipment Development. The process developed for producing the fuel pins consists of melting billets and return scrap in a shallow crucible. The crucible is mounted on an elevator mechanism in a heating zone below an array of nonpermeable refractory mold tubes which are suspended vertically. The upper ends of these tubes are sealed and the lower ends are open. The furnace is evacuated and the crucible raised to immerse the open ends of the mold tubes in the molten fuel. The furnace is then pressurized, forcing metal into the mold cavities, which are still under vacuum. As soon as the metal in the molds has solidified, the crucible is lowered before the metal in the heel has solidified. Precision-bore, high-silica glass tubes, protected from attack by the molten metal by a thin thoria wash, have been the most successful molds used to date. Spray-coated graphite crucibles have been used for melting.

After cooling, the furnace is opened, the gravid molds are transferred to a process machine where the pins are fed individually through a miniature jaw crusher, the ends are cropped, and the resulting pins are fed progressively through an eddy current sensing coil, pneumatic diametral gage, balance, and length caliper. Auxiliary operations include collection of the sheared ends, sampling, breaking of reject material into short lengths for recharging into the cycle, and loading the pins into a transfer magazine for movement to subsequent assembly and bonding operations.

The injection-casting furnace (Figure 2) consists of a base upon which are mounted the support for an induction furnace, a pneumatic ram for elevating the crucible assembly, a mount for a superstructure carrying the mold heaters, and an adjustable mold pallet receptacle. Each of these items was designed as subassemblies to be plugged into the furnace base. The unit is enclosed in a metal bell jar which is locked against a flange by a contracting ring. Where possible, radiation-resistant materials were employed. Where radiation-resistant components had not yet been developed, they were made replaceable.

The use of radiation-resistant materials and plug-in major subassemblies presented considerable problems in the operation of this equipment. Metallic gaskets were not as satisfactory as conventional synthetic rubber O-rings for high-vacuum seals. The induction coils, which were insulated from the hot crucible with spun alumina, overheated (above 800°C) and the excessive temperatures distorted mountings and threw the closely fitted plug-in assemblies out of alignment Considerable mechanical

Figure 2

Prototype Injection Casting with Bell Removed. A pallet of fuel pins is supported by manipulator to be loaded in the mold heating zone.

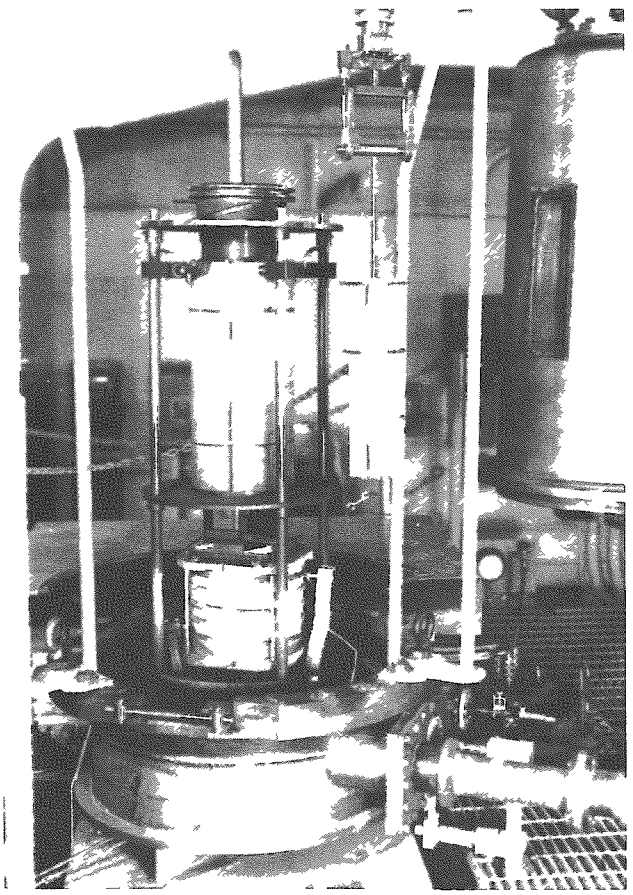

rework was necessary to the furnace support and superstructure. Thin molybdenum reflectors were substituted for the alumina; by rapid melting and reducing the holding time, the temperatures were lowered.

Difficulty was encountered with the mold heater assembly. Because of the exposure of the lower ends of the resistance elements to the high temperature of the melting furnace, the element life was very short. The lower ends of the molds became overheated while the upper ends remained cold. A pair of counterbalanced, reflector-insulated, trap-door covers were installed on the top of the induction coil assembly to reduce these temperatures. These covers are nudged open by the rising crucible.

Tests have been made without added heat to the mold chamber, and successful casts were produced. However, the high percentage of slightly short pins produced in initial tests has indicated the desirability of an electrical heater to control the temperature of the mold tops.

Further work is under way on crucible coatings, molds and mold-coating techniques. Crucibles are now coated with a ZrO_2-ThO_2 binder aqueous solution applied by spraying. Zirconia flame spray-coated crucibles were tested and found to last only from 2 to 4 melts. Some tests were also made with ZrO_2-ThO_2 flame spraying. This was discontinued because of a resulting high air count, and the coatings produced were not satisfactory due to inability to fuse the ThO_2.

Development work is continuing in cooperation with various companies on mold materials. The Corning Glass Company has produced trifluted tubes by a precision redraw process. They have also furnished finely frosted glass tubes and leached, but unfired, Vycor glass tubes in hope of being able to produce a more adherent mold coating on these glasses. Tests on these to date have been inconclusive. The trifluted mold shows

definite promise for the future development of a fuel element with a more efficient heat exchange geometry. The National Carbon Company has furnished graphite molds for testing. To date, these have proved incapable of holding a vacuum long enough for use in the inverted casting process. The Fischer-Porter Company supplied an experimental Vycor mold of hexagonal shape pierced by an array of core tubes. The thoria coating was not satisfactory and the mold was excessively costly; further development was therefore cancelled.

The vacuum system of the furnace has undergone several modifications. Because of the required use of radiation-resistant metallic and solder seals, the in-leakage rate of the furnace was too high. Two 48-cfm mechanical pumps were substituted for the diffusion pumping system. These were to maintain approximately 70 microns of Hg pressure in the furnace, but a considerable oxidation of the crucible heel was noted under these conditions. A technique whereby initial heating and melting are done under one atmosphere of argon pressure was therefore developed. When the metal has nearly reached the casting temperature, the vacuum pumps are started and the furnace is rapidly evacuated for the casting operation. This has reduced oxide formation and has assisted materially in controlling induction coil temperatures.

Figure 3

Prototype Fuel Pin Processing Equipment for Depalleting, Demolding, Shearing and Inspecting.

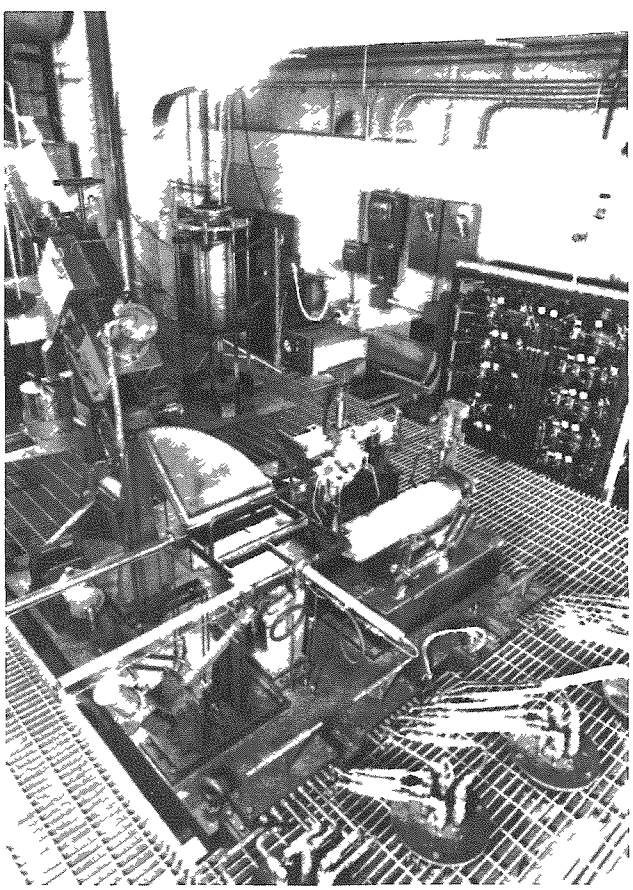

As originally installed, the pin-processing machine (see Fig. 3) consisted of an inclined frame upon which were mounted (1) a rotary index subassembly which received an inverted mold pallet from the casting furnace, (2) a pair of steel crusher wheels in series with two pairs of wire brushes, (3) a pneumatically powered double-guillotine shear, and (4) an inclined sector trough for changing the position of the pin 90° and dropping it into a transfer shuttle. The pallet index device limited the number of pins which could be cast per batch to 60. Since this batch size must be doubled or possibly tripled, a new feed device was required. A cylindrical hopper which may be rotated about a horizontal axis perpendicular to its cylindrical axis was designed.

Each end of the cylinder has a hinged cover which is held tightly closed when the end of the can is tilted below horizontal. A cam causes the uppermost cover to open when the cylinder is in the vertical position. The pallet of pins is removed from the furnace and placed in the hopper, which is then inverted. This allows the pallet to be withdrawn, leaving the pins in the hopper. The hopper is then inclined to the 45° incline position, aligning a shutter slot with the pass line of the crusher and shear. A single mold delivery shutter-agitator feeds the molds individually into the demolding crusher.

The demolder originally consisted of a pair of grooved and serrated crushing rolls in line with two pairs of circular wire brushes. Two gear trains and a rack driven by a pneumatic cylinder imparted a reversing rotary motion to the rolls and brushes. The gravid molds were fed between the crushing rolls, which were set to crush the mold but to allow the pin to pass freely into the brushes which were supposed to clean the surfaces of glass particles and thoria. The unit did not work satisfactorily because of the tendency of the glass particles to become packed firmly between the rolls, locking their movement. The equipment was redesigned to consist of a single moving crusher jaw driven by a small pneumatic cylinder which oscillates against a fixed jaw This effectively crushes the glass and, because of its vibratory action, does not become packed with glass. A fully effective method for removing the thoria powder is yet to be developed.

The guillotine shear is still in use in spite of its tendency to bind with the accumulation of adherent fuel alloy material. A lever blade shear has been designed which is hammer driven in both directions with more easily replaceable blades.

The transfer table will probably require only minor revisions. The pneumatic actuator originally used to drive the fuel pin through the scanning eddy current coil and pneumatic gage has been replaced by a synchronous motor. This motor is powered by a variable frequency oscillator which also will furnish a signal to power a similar synchronous motor on the dual pen recorder. This allows direct coordination of defect position with the plots of the eddy current signal and diametral measurements.

The inspection module has been changed by the redesign of the component units for easier plug-in replacements. This development work is still under way. The precision and repeatability of the remote signals have been generally satisfactory.

3. Development of Welding Processes for Fuel Core Components

Welding of Spiral Spacer Wires (D. E. Walker, C. C. Stone and R. A. Noland)

A Type 304L stainless steel wire, 49 mils in diameter, is helically wrapped around each EBR-II fuel jacket (0.174 in. x 0.009 in. wall thickness) to provide a means for spacing the individual elements when

placed in the fuel assembly The wire is fastened at its ends only: to the solid, cast stainless steel tip at the bottom, and to the 9-mill stainless steel jacket tube at the top. No significant problems were anticipated or encountered in inert-gas tungsten-arc welding the wire at the bottom. Prior experience has indicated, however, some difficulty in making the top fastening. These difficulties have been solved effectively by the use of a stored energy, condenser-discharge-type spot welder wherein maximum advantage is taken of the contact resistance between the parts to be welded. A commercial condenser discharge spot welder has been redesigned and incorporated as part of a machine which also wraps the wire tightly and accurately around the jacket. Successful welds have been made on this machine without perforating the jacket. The welds are stronger than the tube wall, and photomicrographs show them to be free from porosity and cracks The weld nugget extends into the tube wall a distance of 1 to 1 5 mils

End Closure Welds (C C. Stone and R A Noland)

The bottom end closures on the EBR-II fuel elements are made by the inert-gas tungsten-arc welding method The bottom end closure, which involves welding a solid cylindrical plug of Type 304L stainless steel to the 0.174 in. OD x 0 009 in. wall tube of the same material, is more complicated because it will have to be done in a strong gamma flux, using remotely operable equipment. A novel method of inert-gas tungsten-arc welding has been devised for this purpose, wherein electrical energy stored in a bank of capacitors is discharged through a gap between a tungsten electrode and the end of the closure plug An arc is thereby produced, which fuses together the closure plug and the tube without movement of either the electrode or the work. A high-frequency device in the welding circuit makes arc starting automatic. The method (called SEA welding) is fast, produces leak-free welds, and electrode life is long. The electrode spacing is not critical to the same degree as in ordinary arc welding. Control of the electrical conditions is readily and simply achieved. The method has been incorporated into a fully automatic machine capable of full remote operation. The machine has a minimum of moving parts and is driven by inert gas-powered devices. It has been tested through many mechanical cycles without maintenance or repair. The machine is now considered ready for use in the manufacture of the first loading for EBR-II

Welding of Outer Hex Tube to Pole Piece (C. C Stone and R. A. Noland)

The outer hexagonal tube which contains the fuel elements and the upper and lower blanket elements is spot welded at six places at its bottom end to a solid Type 304 stainless steel pole piece which positions the fuel element in the reactor grid plate Welding tests have shown that welds stronger than the tube can be made reliably by the inert-gas tungsten-arc straight polarity spot welding method with helium as the inert gas Welding equipment has been designed to perform this operation remotely and

completely automatically. The equipment employs materials and features consistent with a high degree of resistance to mechanical and radiation-induced failure. To avoid radiation-induced electrical problems, gas mechanisms have been used in this equipment in preference to electrical devices. As an example, the spot welding guns are individually gas driven into and out of the welding position by forcing inert gas into a bellows built into each gun. Reliability of the welding guns and of the electrical control system has been demonstrated.

4. Fabrication of Fuel Elements for First Loading
(N. J. Carson, H. F. Jelinek, and A. B. Shuck)

The fuel requirements for the first loading of the EBR-II call for a total of 3000 normal uranium-5 w/o fissium alloy pins and 9100, 48.13% enriched uranium-5 w/o fissium alloy pins assembled into fuel elements. Although it was recognized that further process development was required to raise the yield of acceptable pins and to increase the throughput rate and reliability of the pin-process equipment, production was started in late September on "as is" equipment to satisfy the needs for fuel pins for development of bonding, welding and testing techniques.

To date, a total of 17 normal uranium-fissium melts have been made, representing a total of 1763 pins. Of these, 813 pins (46.1%) were too short to merit further inspection processing. The double guillotine shear requires a casting length of about $15\frac{1}{4}$ in. to produce a pin 14.22 in. long. In many cases, casting length was over 14.22 in. but less than $15\frac{1}{4}$ in. Salvage of these castings by lathe or hand shear cutoff is possible and will be used in the enriched uranium operation to increase yield.

Of the remaining 950 pins that were processed, 709 (74.6%) were found acceptable. The surface inspection by eddy current coil, air gage, and visual observation was extremely stringent. Pins were rejected for slight surface imperfections or depressions. Adoption of a practical inspection standard, rather than an absolute standard, which would normally require machining or grinding, would result in salvage of many castings.

Several conditions have been found to influence the lengths of the castings. (1) If the melt and the molds are both too cold, the metal does not penetrate to the top of the molds. (2) If the molds are cold, the metal may be made to penetrate to the top of the mold by greatly superheating the melt. In this case, the metal may not solidify in the lower end of the tube and may run back out. The superheated castings may also be expected to show more internal shrinkage. (3) The length of time of immersion also affects the solidification at the lower end of the mold. Too short a period of immersion can also cause run-out. (4) If the rate of pressurization is too slow, the metal will solidify before reaching the top of the molds; if too fast, molds may be broken. (5) The integrity of coating affects casting length. All of these conditions require careful adjustment for each furnace

and for each composition. The furnace and controls are being modified to allow closer control of melt temperatures, mold temperatures, pressure rates, and time cycles.

5. Fabrication of Blanket Rods (W. R. Burt, Jr., R. L. Salley, R. D. McGowan and C. H. Bean)

Development work on the fabrication of uranium-molybdenum alloys as blanket material for EBR-II was discontinued in 1959 when it was decided to use unalloyed, beta-treated uranium for this purpose. Unalloyed uranium was selected because of the greater ease with which it can be reprocessed for measuring breeding gains. The total requirements for the blanket, including sufficient material for a second fuel loading and some spares for mock-up work in the Fuel Recycle Facility, are as follows: (a) 7000 upper and lower rods requiring 14,000 uranium slugs, 0.3160 ± 0.0005 in. diameter x 9.000 ± 0.005 in. long; and (b) 16,400 inner and outer rods requiring 82,000 slugs, 0.4330 ± 0.0005 in. diameter x 11.000 ± 0.005 in. long. The uranium is depleted and contains 0.22 ± 0.02 w/o U^{235}. The manufacture of the uranium slugs is being done by outside vendors. Inspection of the slugs, their assembly into rods, and the sodium bonding are carried out at ANL.

Fabrication of Uranium Slugs: Melting is done in 1500-pound steel shell, induction-heated vacuum furnaces in mullite-coated graphite crucibles, and the metal is bottom poured into mullite-coated, split graphite molds. Castings are water quenched after removal from the furnace and their hot-tops and pipes cropped. Castings of good surface quality and with all visible pipe removed have generally yielded sound rods. Chemical analyses were run on each billet; the data for the first 180,000 pounds of ingots produced are shown in Table II.

For rolling, the billets are preheated in a carbonate salt bath (75% K_2CO_3 + 25% Li_2CO_3) at 625-650°C for 60-80 minutes, and are broken down on a 22 in., 2-high Birdsboro blooming mill. A roll schedule of 19 passes is employed for the 1000-pound billets and the billets are finished as 1.5 x 2.5 in. oval bars. Each oval bar is hot sheared into two 17 ft lengths.

The bars are then transferred to an equalizing salt bath furnace for a minimum soak of 12 minutes at 650°C prior to reduction on a continuous bar mill. The mill consists of six Birdsboro stands in tandem. Mills #1, 3, and 5 are vertical mills with oval rolls, while mills #2, 4, and 6 are horizontal round rolls. The oval bars are reduced to 1.5 in. diameter rounds with a nominal reduction of 15% per stand. The bars enter at 90 feet/minute and leave the #6 mill at 250 feet/minute. The temperature of bars leaving the #6 mill is approximately 590-620°C. The 40 ft, 1.5 in. diameter bars leaving the #6 mill are fed into a Birdsboro flying shear where they are cut into 20 ft lengths and run onto a cooling bed.

TABLE II

Specifications and Analyses of Ingots

Element	Specification	Ingot Analyses, ppm[1]		
		High	Low	Average
U^{235}	0.22 ± 0.02 w/o	0.2201	0.2087	0.2130
Boron	1 ppm maximum	1	-	< 0.5
Cadmium	1 ppm maximum	< 0.7	-	< 0.7
Carbon	750 ppm maximum	740	60	298
Chromium	100 ppm maximum	< 20	-	< 20
Copper	100 ppm maximum	70	4	13
Iron + Nickel	300 ppm maximum	290	90	171
Magnesium	25 ppm maximum	10	-	< 7
Manganese	150 ppm maximum	140	30	58
Nitrogen	100 ppm maximum	58	10	24
Silicon	150 ppm maximum	160[2]	15	76
All Others[3]	400 ppm maximum	400	20	87
TOTAL (excluding U^{235})	2077 ppm maximum			755

[1] Based on 168 ingots

[2] One ingot analyzed 160 ppm; all others below 150 ppm.

[3] Includes Al, Be, Co, P, Pb, Sn, V, and Zn.

Rolling of the bars, first to 7/8 -in. diameter and then to 1/2 in. is performed in the same mill, using the same preheat temperatures and the same rolling speeds. The surface quality of the 1/2 in. diameter bars is good; some spots are out of round, but the bars finish within the ±0.007 in. limits set on the as-rolled diameter.

Beta heat treatment is performed by heating 20-ft lengths in the beta-phase temperature range for 5 minutes and quenching in water. The bars are then straightened, turned to approximately 0.017-in. over-finished diameter, and rough cut to length. Following centerless grinding to size and finish machining to length, the slugs are inspected visually for surface defects such as pits, seams, burrs, etc., length and diameter dimensions, and straightness. The slugs are also given an ultrasonic velocity test for the detection of any alpha phase structure.

Attempts were made to develop hot swaging techniques for processing the 1/2-in. diameter bars to stock for the small (0.316-in.) diameter slugs. However, this method of fabrication was abandoned, since it resulted in excessive variations in grain size. The small-diameter slugs are therefore being made by turning and grinding from the 1/2-in. bar stock, similar to the fabrication of the large (0.433-in.) diameter slugs.

To date, a total of 16,050 slugs have been received. These were further inspected at ANL visually, weighed to insure a minimum density of 18.7 g/cc, and given an ultrasonic through-transmission test for internal defects. Spot checks on every twenty-fourth slug were made for length, diameter, and warp. Of the slugs that were inspected, 13,895 (86.6%) were found acceptable, 1827 (11.4%) were rejected for surface pitting or machining marks, and 325 (2.0%) were rejected for defects found in ultrasonic testing. The ultrasonic transmission technique, developed by the Nondestructive Testing Group (R. H. Selner and R. B. Perry) will locate flaws greater than 1/32-inch in any direction, and is effective in revealing abnormal grain size conditions.

Loading and Sodium Bonding: The loading and sodium-bonding processes are being carried out according to procedures developed and recommended by E. Sowa of the Reactor Engineering Division. All loading operations are performed in an atmosphere of 90 v/o argon-10 v/o helium, which is also the gas mixture surrounding the compression spring above the sodium at the top of each rod. The work is performed in a glovebox designed to permit four operators working simultaneously to extrude the necessary sodium, load, and cap a total of 216 rods per day. The box was fabricated with an extruded and welded aluminum angle frame, clear glass windows on two sides, glass windows at the top, transfer locks at each end, and a 3/4-in. thick stainless steel base containing three 9-in. diameter nozzles for inserting tubular bundles containing the blanket tubes. Each nozzle has an individual cover to seal the box while tube bundles are being transferred to and from the bottom of the glovebox. The box is mounted on a steel frame 7 ft above floor level to allow clearance for positioning the 61-in. long tube bundles of inner and outer tubes under the box. Operators' platforms are located on each side of the box with separate control stations at the ends of the platform for each operator. A general view of this equipment is shown in Figure 4. Equipment for evacuating and purging the bottom nozzles and vacuum locks is located under the operators' platforms.

Three portable tank-type oil furnaces heated with external electric resistance type elements are located in a 6-ft deep pit under the box. Each furnace is positioned directly under one of the nozzles in the bottom of the glovebox so that it may be raised to surround the tube bundle suspended from the nozzle. The bath of heated silicone oil is used to melt the sodium inside the blanket tube. The oil bath temperature and elevation of each furnace is controlled at each operator's separate control station.

A horizontal direct pump hydraulic extruder is used to extrude solid sodium slugs inside the glovebox. This extruder is built up with a 6-in. bore x 17¼-in. stroke, 1500-psi, double-acting hydraulic cylinder which is coupled to a vacuum-tight container opening to the inside of the glovebox at one end of the box. A 17-in. long, 3½-in. OD x 2½-in. ID steel liner is filled with sodium, inserted in the container, and a steel die in a die holder

Figure 4

Glovebox Facility for Loading EBR-II, Mark I Blanket Rods

Shown in this view are the elevated inert atmosphere glovebox, operators' platform, control stations, and vacuum pumping systems under the platform.

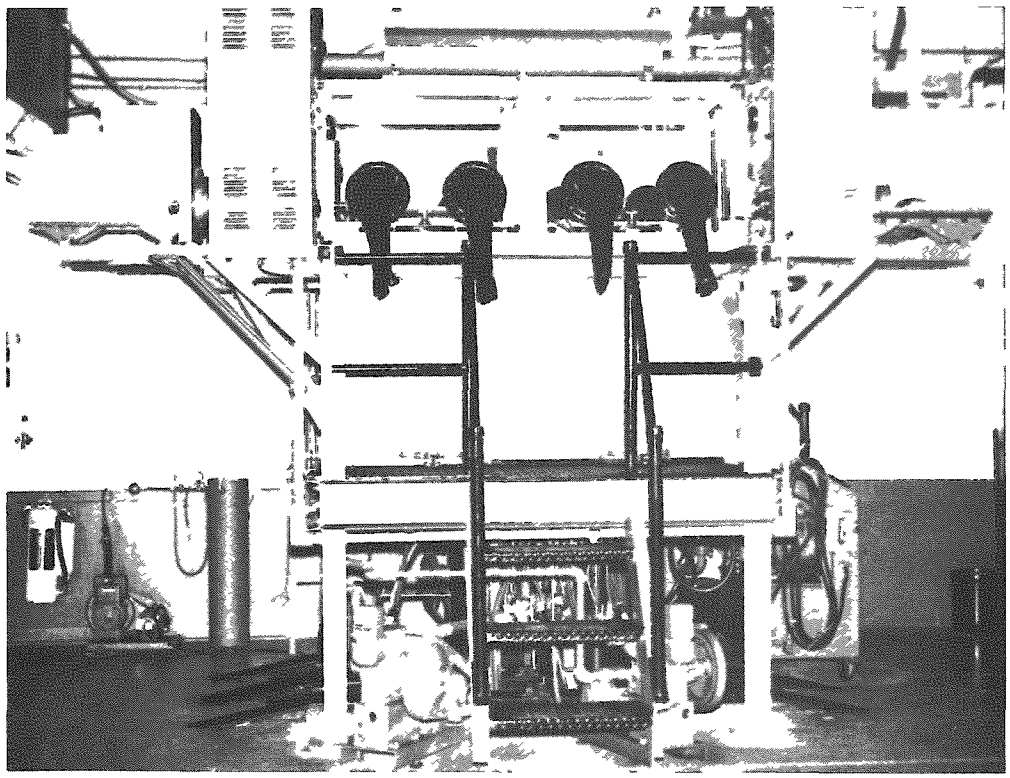

is clamped in position in front of the container and liner. The hydraulic ram then extrudes the sodium through the die and onto a run-out table. When the extruded sodium reaches its proper length, it trips a limit switch which actuates a flying shear that cuts the sodium to length without interruption in the smooth flow of sodium from the extruder. In this way sodium of uniform length and diameter can be prepared for loading into the blanket tubes.

In loading blanket rods, stainless steel tubes, with the bottom end plug welded in place, are placed in a tube bundle which is capable of holding 36 tubes. The tube bundle is then inserted and sealed in a loading port on the underside of the glovebox. The bundle is then evacuated to 25 microns of Hg, purged with the inert gas mixture, evacuated, and purged again before opening to the glovebox.

Polyethylene ferrules are inserted at the top of each tube and sodium slugs inserted as shown in Figure 5. The ferrules serve a twofold purpose: (1) to prevent contamination of the top portion of the tube with

Figure 5

Inserting Extruded Sodium Slug in Blanket Tube with End Protected by Polyethylene Ferrule.

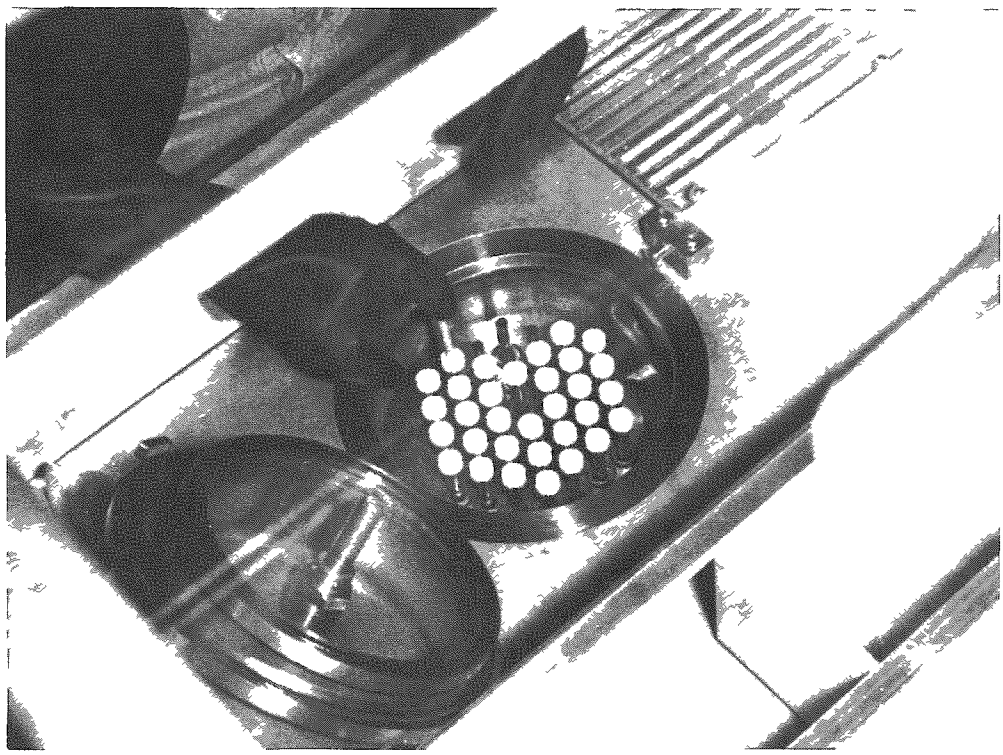

sodium, which could result in a poor or defective weld; and (2) to prevent the possibility of inserting two or more slugs of sodium in the same tube. This is accomplished by removing the ferrule from the tube immediately after inserting the sodium slug.

The sodium slugs are extruded in two sizes: 0.250 in. diameter x $3\frac{7}{8}$ in. long for the upper and lower blanket rods, and 0.400 in. diameter x 9.25 in. long for the inner and outer blanket rods. The sodium is extruded at a rate of approximately 20 in./minute and the reduction in area for the two sizes is approximately 100:1 and 40:1, respectively.

After all the tubes in the bundle have been loaded with sodium, the port cover is secured in place and the bundle is evacuated to 25 microns of Hg. The oil bath is then raised until the bottom 6 in. of the tube bundle are submerged in oil. The sodium melts and thereby frees any entrapped gases. The oil bath is then lowered and the sodium allowed to solidify before purging with the inert gas mixture and removal of the port cover.

The uranium slugs are then loaded into the tubes. To prevent contamination of the uranium, canvas gloves are worn over the rubber gloves. The chief source of contamination is vacuum grease which can be picked up from the "O" rings of the port and bundle covers. After the uranium has

been loaded in all of the tubes, the oil bath is raised until all but 2 in. of the tubes are submerged in oil. The sodium then melts and allows the uranium to settle to the bottom of the tubes.

Compression springs are then inserted in the tubes. The springs, when completely settled in the molten sodium, are even with the top edge of the tube. When all of the springs have settled, the oil bath is lowered and the top end plugs snapped in place. This is done by clamping two tubes at a time, inserting end plugs in the openings in the clamp, and snapping the plug in the tube with the aid of an argon gas-operated hammer. The plug is held in place by a rolled groove in the tube which matches a corresponding groove in the plug. The compression spring is compressed 1/4 in. at a load of 10 pounds.

After all of the plugs have been inserted, the bundle and port covers are positioned securely in place and the bundle removed from the glovebox. The end plugs are then welded and the welds leak checked with a helium mass spectrometer. Thirty-six rods are checked simultaneously by placing them in a tube bundle and evacuating the bundle with the vacuum pumps at the leak detector A leak in a tube is readily detected since the atmosphere at the top of the sealed tubes contains 10 v/o helium.

Upon completion of the leak testing, the rods are loaded into racks for transfer to the bonding furnace. Each rack holds 6 rods; the furnace holds 36 racks. The rods are heated for 4 hours at 475°C and vibrated at 1800 cycles per minute. At the end of 4 hours, the rods are removed from the furnace, one rack at a time, and water quenched. The rods are then removed from the racks and placed on pallets for transferring to the eddy current testing station. This test provides a permanent trace from which the sodium level is measured and voids are detected.

Immersion-type salt baths were originally designed and installed for bonding the sodium to the tubes following the outgassing operation. This heat treatment, which was to be conducted at 550°C, proved unnecessary, as satisfactory bonding in the bottom portion of the tube is achieved in the normal bonding operation.

To date, 3276 upper and lower blanket rods have been assembled. Of these, 51 have been rejected because of poor welds, 45 in the loading and bonding operation, and 11 as a result of eddy current testing. A total of 2526 rods have been sodium bonded; of these, 1968 were found acceptable as determined by eddy current testing. Nonbonded rods rejected by eddy current testing are recycled through the sodium bonding process.

6. Development of Steam Generator and Superheater (R. A. Noland)

All purchasing arrangements have been completed for the procurement of the approximately 80,000 feet of seamless cold drawn alloy steel tubing in four sizes that are required for the evaporators and superheaters. The Tubular Products Division of Babcock and Wilcox Corporation has been selected as the vendor. The tubing is required to conform with ANL Specification SGT-IC, a modification of ASTM Specification A213-57T. The modification consists of more stringent tolerances on diameter, straightness, and wall thickness, plus the requirement that ID and OD defects may not exceed 4 mils in depth. Mill tests include dye-penetrant inspection of the outer diameters of all tubes, and shear-wave ultrasonic testing in both directions at a sensitivity sufficient to indicate a 4-mil notch machined on the ID and OD of a tube having the same wall dimensions as the lot being tested. At the laboratory it is planned to reinspect material ultrasonically to a 3-mil notch, and to inspect the outer diameter surfaces by means of eddy current examination.

At the present time, an amount of tubing sufficient to manufacture five evaporators is on hand. Enough steel was originally made by Babcock and Wilcox for the entire order, but unfortunately the cleanliness of a large fraction of the ingots was beyond the maximum limit acceptable under the SGT-IC specification. Material of acceptable cleanliness has been made recently in an amount sufficient to complete the order, and the tubes are now being processed at the mill.

Duplex Tube Bonding (L. C. Hymes and R. A. Noland)

Work on the development of the bonding technique is being concluded. With the process in its present state of development, bonds which have strengths approaching that of the 2.25 w/o Cr-1.0 w/o Mo steel tubes can be obtained consistently. The bonding procedure consists of nickel plating the outer diameter of the inner tube with a 3- to 5-mil layer of nickel, coating the inside of the outer tube with 0.3 to 0.5 mil of a nickel-phosphorous coating (Kanigen),* and after cleaning the mating surfaces the inner tube is slipped into the outer tube and the pair drawn together over a mandrel and through a die. To improve the mechanical fit between the tubes, the duplex is next expanded by pulling a mandrel through its inner diameter. Duplexing is followed by three successive heat treatments: one at 927°C (1700°F), the second at 1120°C (2050°F), and the third is an anneal at 760°C (1400°F).

Processing of the superheater tubing at the mill has not proceeded beyond the hot-rolling operation, pending negotiations with the Superior Tube Company. These negotiations are contingent upon

*Kanigen is a trade name of the General American Transportation Corporation for an electroless nickel-plating process.

demonstration of the capability of their proprietary process to produce small-diameter, bonded duplex tubing. They are presently manufacturing a small-size development test lot of full length tubing.

Tube to Sodium Tube-Sheet Welding (C. C. Stone, R. A. Noland and O. Wortman)

The steam tubes are to be welded to the sodium tube-sheets in the EBR-II steam generators. Because of the stringent and rigorous manufacturing and service requirements of these units, a great amount of attention has been paid to the development of a welding device capable of producing the large number of high-quality welds reproducibly. A welding device has been tested through several stages of development. Welds made with the current model are leak-free and are stronger in tension than the tubes. The welding cycle is initiated by the operator, but once initiated the cycle is under complete electronic control. The welding process utilizes the inert-gas, consumable-electrode, reverse-polarity technique using 0.035 in. diameter wire as the electrode, and argon-5% oxygen as the cover gas. Fillet welds are made in a single pass without prior joint preparation. The time to make a single pass weld is about 10 seconds after the welding gun is put in position on the tube. The welds are smooth and do not require machining or grinding.

A production gun is being built to make the welds on the evaporator. These will be made with the tubes in the horizontal position and the work will be moved beneath the welding electrode by rotating the entire steam generator in a special fixture To reduce the possibility of weld cracking, the work will be preheated to approximately 300°C, and 1.25 w/o chromium-0.5 w/o molybdenum, low alloy steel welding wire will be used. Following the welding of all of the tubes into each tube-sheet, the weldment will be stress relieved at 745°C.

Construction of Steam Generators (R. A. Noland, C. C. Stone and D E. Walker)

To date, all of the process engineering has been completed and the fixtures and tools necessary for manufacturing are being built. All of the components have been ordered and some are presently on hand. Wherever possible, these components have been ordered as finished parts.

Ultrasonic Inspection (R. H. Selner and C. J. Renken)

Ultrasonic techniques have been developed for inspecting the EBR-II evaporator and steam exchanger tubing. One technique is used to inspect the tubing for flaws. The other technique is used to inspect the bonding of the duplex tubing.

For inspecting the tubing an immersed shear wave technique is being used. In this technique a transducer is positioned over the tube and mode conversion at the surface of the tube converts the transmitted longitudinal wave into a shear wave. The shear wave is reflected between the

inner and outer surface of the tube. If a defect in the tubing on the outer and inner surface of the tube is encountered by the wave, a portion of the ultrasonic energy is reflected back to the transducer. The amplitude of the reflected signal is used as a basis for determining the relative size of the defect. Using this technique, it is possible to detect a flaw 3 mils deep and 1/4 in. long at a scanning speed of 2 feet/minute. In order to inspect the 30-foot tubes, it was necessary to design and fabricate a 35-foot scanner assembly. Many of the design features were patterned after similar equipment developed at the Oak Ridge National Laboratory. A Sperry Reflectoscope and Monitor are used to generate, display and monitor the reflected signal. The monitor is adjusted so that a signal from a flaw operates an audible alarm circuit.

An immersed through-transmission technique will be used on the bonded duplex tube. In this technique, two separate transducers are required. The transducers are positioned so that the ultrasonic beam passes through the center axis of the tube. A lack of bond or variations in bond quality will decrease the amplitude of the beam. The monitor can be adjusted to detect the loss in transmission and sound the alarm.

The tubing is also being inspected with an eddy current technique. This test was incorporated to detect circumferential type flaws near the surface.

7. Boron Control Rods (D. E. Walker, R. A. Noland and S. J. Matras)

A number of boron-10-containing control rods were requested by the Reactor Engineering Division for the EBR-II. Specifications called for 29.3 grams of elemental boron-10 encapsulated in a stainless steel tube over a length of 7 in. The tube diameter was to be the same as that of the inner and outer blanket tubing (0.493 in. OD x 0.020 in. wall thickness).

The approach used to produce the rods was the cold swaging process currently used to make stainless steel and/or Zircaloy-clad UO_2. Preliminary examination of several rods has indicated that cold swaging followed by annealing will produce a satisfactory product with the required weight of boron.

B. Fabrication of Core and Blanket Components for the Argonne Fast Source Reactor (AFSR) (W. R. Burt, Jr.)

The Argonne Fast Source Reactor consists of a right circular cylinder of highly enriched uranium, 4.53 in. in diameter and approximately 4.53 in. long. The core is comprised of three sections, approximately $1\frac{5}{16}$ in. thick. Each uranium disc which makes up these sections is sealed in evacuated, 0.005 in. thick nickel can. Two of the sections are each composed of a single disc, 1.302 in. thick, machined from an uranium casting. The third section can be made up of various combinations of discs ranging in thickness from 0.565 to 0.050 in. The 0.565 in. thick disc was machined from a casting while the discs below that thickness were made from rolled plate.

The blanket or reflector of the AFSR consists of a stack of five rings of depleted uranium which form a thick-walled right cylinder, 20.63 in. OD, 4.70 in. ID and 20.63 in. high. Two end plugs complete the blanket of depleted uranium around the core. Located vertically in the blanket are two 2 in. diameter safety rods, two 2 in. diameter shim rods, and one 1 in. diameter control rod.

There are three experimental holes in the blanket. One $\frac{1}{2}$-in. diameter hole is located on the horizontal center line of the core and blanket. A $2\frac{1}{8}$-in. diameter radial beam hole terminates 2 in. from the inner edge of the blanket, and a $1\frac{1}{16}$ in. diameter grazing hole passes horizontally through the blanket.

Casting of Enriched Core Components: Initial development work was performed to establish techniques for casting $4\frac{1}{2}$-in. diameter, $1\frac{1}{2}$-in. thick, enriched discs in a vertical manner such that a core rod could be used to cast a disc with a $\frac{1}{2}$-in. diameter hole. All attempts to make a vertical casting were unsuccessful due to internal porosity at the top of the casting, and this method was abandoned in favor of casting the disc in a horizontal plane without the core rod.

Melting and casting were done under vacuum in a quartz tube furnace with an external induction coil. Graphite molds, stopper rods, and crucibles were used throughout. The molds were flame sprayed with mullite, and the crucibles and stopper rods received a brush-applied base coating of $MgOZrO_3$, followed by an air-spray coating of ThO_2. The crucibles and stopper rods were oven dried prior to use in the furnace.

As biscuit uranium was used in the charges, the melts were frozen and remelted prior to pouring at 1215 to 1240°C. The preliminary freezing was used in hopes of reducing the impurity content of the final casting. In all cases the vacuum prior to pouring was 2×10^{-4} mm of Hg or better.

Three discs and three slab castings were made. Two of the disc castings were machined to 1.302 in. thickness, and the third disc casting was machined to 0.565 in. thickness. The slab castings were rolled to various thicknesses to provide stock from which discs 0.300, 0.150, 0.100 and 0.050 in. could be made.

In order to reduce the amount of enriched uranium scrap generated, chips from machining were compacted into briquettes and remelted, the resultant casting then being charged to the disc-casting process. No pretreatment of chips was employed. The machining chips were compacted into $\frac{3}{4}$-in. diameter briquettes ranging from $\frac{1}{4}$ to $\frac{1}{2}$ inch in height. One development casting was made using chip briquettes, the resulting casting analyzing 11 ppm N_2, 0.85 ppm H_2, 35 ppm O_2, and about 200 ppm C. Melting and casting were done in a Vycor tube, vacuum induction furnace utilizing a MgO crucible and stopper rod with a mullite-coated graphite mold. Casting yield was 88% of the charged weight, the balance being a heavy skull of oxidized chips. Two enriched castings were made by remelting of chip briquettes and resulted in yields of 83.8 and 88.4%.

Rolling, Shearing and Heat Treatment. Three castings were hot rolled into plates of various thicknesses from which the $4\frac{1}{2}$-in diameter discs were machined. The hot rolling consisted of a 30-minute preheat to 600°C in a carbonate salt bath with a 5-minute reheat per pass. All billets were cross rolled to a width of $4\frac{7}{8}$ in. prior to long rolling to the final thickness. One of the $6\frac{5}{8}$-in. long castings and the $9\frac{1}{4}$-in. long casting were rolled to a nominal 0.35-in. thickness and sheared into squares 5 in. on a side. The remaining $6\frac{5}{8}$-in. long casting was rolled to various thicknesses and sheared at appropriate stages into 5-in. squares for machining discs of 0.300 (five discs), 0.150 (two discs), 0.100 (one disc), and 0.050-in. (two discs) thickness. The latter two discs were cold rolled to the 0.050-in. final thickness from 0.060 -in. thick hot-rolled plate stock. The 5-in. squares were subsequently sheared into octagons; sheared scrap was used for remelt stock in casting the large discs.

Each sheared octagon was given a beta heat treatment followed by a water quench. The discs were spray coated with a graphite suspension prior to the heat treatment. The heat treatment consisted of immersion in 735°C lead for 10 minutes. The 0.050-in. thick discs were placed in a heavy copper jacket which was evacuated and sealed prior to the beta heat treatment and water quench. The copper jacket restrained warp and prevented lead contamination. All the sheared octagons were hand straightened on an arbor press.

Machining Enriched Uranium Components. Machining and drilling of the cast discs and the hot-rolled octagonal discs were done by conventional methods. No liquid coolants or lubricants were used; argon gas was directed at the cutting tool to reduce burning of the chips and to afford slight cooling. Drilling was also done under an argon gas blanket.

Nickel Canning. The two cast and machined discs and a group of discs of various thicknesses were sealed into three 0.005-in. thick nickel cans, deep drawn into two sections. These two sections surrounded the uranium core and provided an overlapping joint around the circumference of the uranium. The two cast discs also had nickel tube inserts for passage of the reactor core thermocouple One cast disc had a $\frac{1}{2}$-in. diameter hole which was sealed by a duplex tube of nickel inside Zircaloy-2. The tube inserts and the can joints were sealed by silver soldering A small pinhole punched in one face of the nickel can provided a means of vacuum checking the silver-soldered joints for possible leaks after the joints had been hand filed to size. The sealed can containing the enriched uranium was placed into a chamber which was evacuated to a minimum vacuum of 10^{-4} mm of Hg and the pinhole in the can face sealed with silver solder, using a tungsten electrode for heat input into the evacuated chamber

Blanket Components. The depleted uranium blanket components, consisting of five rings, five rods (for control, safety, and shim rods), and two end plugs, were procured as rough machined castings from the National Lead Company at Albany, New York. All castings were made by conventional induction vacuum melting techniques. The rough machined castings were finish machined at ANL by standard uranium machining practices. Three of the ring castings which exhibited areas of severe porosity had the defective areas drilled out and depleted uranium plugs inserted to insure sound metal in the blanket.

Figure 6

Final Assembly of Depleted Uranium Blanket Components With Top Plug Suspended Above its Location in the Blanket.

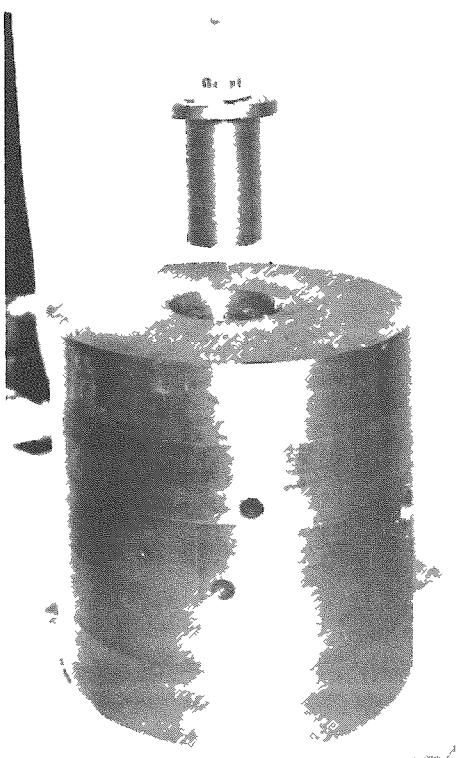

The small $\frac{1}{8}$-in. diameter thermocouple holes (approximately $10\frac{1}{4}$ and 8 in. long) and the $\frac{1}{2}$-in. diameter hole passing horizontally through the blanket were made by drilling 1-in diameter holes and plugging them with 1-in. long slugs containing the required diameter hole. This was done to insure straightness and correct diameter of the finished holes.

After all components were finish machined and inspected, the blanket was assembled and shipped to the Idaho Division. The assembled blanket is shown in Figure 6, the top plug being suspended above its location in the blanket.

Yields. A total of 36,336.56 grams of highly enriched uranium were used in fabricating the 16 finished discs weighing 24,688.58 grams, a yield of 67.9%. The balance consisted of melt residue (11.7%), machining chips and fines (18.3%), solid scrap (1.8%), and losses in rolling and heat treating media (0.3%). The total charge to melts was 47,856.36 grams, 75.9% being virgin metal and 24.1% being recycled material.

The 12 depleted uranium blanket components received from National Lead Company weighed 2,805 kilograms, and the finished components shipped to Idaho weighed 2,083 kilograms, representing a yield of approximately 75%.

C. Fabrication of Spiked Fuel Rods for EBWR (Core 1A)
(W. C. Kramer and C. H. Bean)

The spiked fuel for the Core 1A loading of the EBWR is to be jacketed in small-diameter (approximately $\frac{3}{8}$ in.) Zircaloy-2 tubing. To procure this tubing, an order was placed with the Wolverine Tube Division of Calumet & Hecla Company in February to fabricate 1000 feet of seamless tubing, 0.385 in. OD x 0.335 in. ID, in $6\frac{1}{2}$-ft lengths, from material supplied by ANL. The first tubing received in March was inspected by means of a dual-frequency eddy current instrument and was found to contain large numbers of severe longitudinal cracks radiating from the ID of the tube. Some of the cracks completely penetrated the wall. A second batch of tubing inspected in June also gave evidence of internal cracks which, although not quite as severe, still extended through as much as one-third of the wall thickness. Attempts at altering the fabrication process by the supplier on a third batch of tubing in September showed no improvement. It was thought that the cracking was probably due to excessive cold working introduced during processing of the material to the size ordered Based on specifications which limited processing steps to 90% total reduction from extruded to finished tube, orders were placed with Wolverine in October to fabricate 1000 feet of tubing for development work at ANL and for 15,000 feet of tubing for production of the spiked fuel rods This tubing is being fabricated from 3400 lb of vacuum-melted ingot material which ANL has procured from Mallory Sharon Metals Company. Of the first six lengths of tubing received and inspected in December by eddy current techniques, four lengths indicated no defects. Internal cracking in the remaining two lengths was not as extensive as in the tubing examined earlier; however, metallographic examination showed one crack to have penetrated as much as seven-eighths of the wall. Further development is required to determine to what extent these defects can be eliminated, and attempts are being made in cooperation with Wolverine Tube to improve the yield.

The fully enriched U_3O_8-aluminum core material for Core 1A is 0.325-0.326 in. in diameter and each element contains two equal lengths of fuel material separated by a $\frac{1}{4}$-in. Zircaloy-2 spacer. A drawing operation is therefore necessary to reduce the annulus between core and jacket. It

was anticipated that difficulty would be encountered in keeping both fuel sections in contact with the center spacer, and in preventing the tubing from galling in the die After several experimental drawing operations using simulated core material, satisfactory results were obtained. X-ray examination indicated that spring loading the trailing end of a loaded tube provides sufficient force to maintain contact between each fuel section and the center spacer. Spray coating the tubing with a suspension of copper powder in Krylon prior to drawing prevented galling and resulted in an excellent surface finish. A 0.376-in. die opening will cause the jacket to just come into contact with the core material; however, the Zircaloy-2 tubing has a tendency to spring back somewhat, leaving as much as a one-mil annulus after drawing

Preparation of equipment is under way for vapor blasting and leak detecting of the completed elements.

Zircaloy-2 strip stock of various thicknesses is required for fabrication of structural components to contain the bundles of fuel rods in the reactor, as spacers for the long rods, and as back-up effort for control rod followers in the event that suitable fuel followers cannot be obtained on schedule. Sufficient strip was required to justify ordering from Westinghouse Electric Corporation (Blairsville Plant) the fabrication on a conversion basis of 2 ingots weighing a total of 3075 lb. Finished strip of the following sizes has been promised for delivery by January 15, 1960

0.062-in. stock	625 lb
0.081-in. stock	800 lb
0.125-in. stock	260 lb

The forging, conditioning, and hot breakdown of forged slabs for this material is progressing on schedule

D. Fuel for TREAT Reactor (R. A Beatty and C. H. Bean)

The production of the required number of fuel elements for the TREAT reactor was completed during 1959. In addition approximately 300 graphite-urania dispersion-type fuel blocks in excess of the number required for the initial TREAT core loading were outgassed, loaded in Zircaloy-3 cans, evacuated, sealed, and stored for possible future use in the reactor. In order to can these extra blocks and also to provide stock for use in various development activities in connection with the Fast Reactor Safety Program, additional 0.025-in. thick Zircaloy-3 strip stock was procured. This strip was obtained by converting two Zircaloy-3 ingots (3138 lb) into strip. Due to the extreme care and close supervision given these ingots during their fabrication by Superior Steel Company, a yield of 2157 lb (68.7%), of finished strip was realized. Material not used for canning TREAT fuel blocks will be used in the Fast Reactor Safety Program.

The following fuel elements were completed in 1959:

166	Type 1 elements (fuel assembly)
26	Type 1a (fuel thermocouple assembly) Type 1b (mid fuel, reflector, and skin thermocouple assembly) Type 1c (transient thermocouple fuel assembly)
20	Type 3 (access hole fuel assembly)
23	Type 4 (control rod fuel assembly).

There were no changes in any of the fabrication procedures which were established in 1958.

E. Fuel Elements for EBR-I (Mark IV)

1. Experimental Pu-1 w/o Al Zircaloy-clad Elements (R. J. Dunworth and O. L. Kruger)

Four test fuel elements were made for the EBR-I reactor. The elements contained rods of Pu-1 w/o Al alloy and will be loaded into EBR-I, so that the alloy may be evaluated for the Mark IV loading.

The rods, 9 in. long and 0.220 in. in diameter, were made by injection casting the alloy into Vycor tubes. Thermocouple holes, 3 in. deep and 0.086 in. in diameter, were drilled in two rods for accurate irradiation temperature measurement. The uranium blanket rods and the plutonium-aluminum rods were loaded through a plastic pouch into the Zircaloy-2 tubes. The tubes were filled with NaK and welded in a Blickman hood. The assembled rods were tested for NaK bond integrity and NaK level by eddy current methods. Each of the four rods was heat treated in vacuum at 325°C for 2 hours. The rods have been shipped to Idaho for insertion into the EBR-I.

2. Development of Fabrication Methods (A. B. Shuck)

Preliminary studies have suggested that the EBR-I fuel slugs may be made either by centrifugal casting into precision permanent molds or by gas pressure injection into precision high-silica glass molds. It may not be possible to establish the final dimensions of the fuel slugs until a critical assembly is made in ZPR-III and the thermal conductivity of the fuel material has been determined. A reference slug dimension of 0.220 in. diameter x 2.125 in. long has been established for developmental studies. Tooling for both methods has been designed. Both methods will be tested to determine which will produce the most satisfactory fuel elements.

F. Canning of Plutonium Loading for ZPR-III (C. C. Stone, R. A. Noland and G. B. O'Keeffe)

Approximately 27 kg of alpha-stabilized plutonium in the form of thin (around 0.090 in.), flat, nickel-coated slugs have been encapsulated in tight-fitted, Type 304 stainless steel cans. The slugs were fabricated and nickel coated by the Dow Chemical Company. Canning was carried out by Metallurgy Division personnel. All slugs were 0.084 ± 0.001 in. thick, and 1.765 ± 0.002 in. high, but were of three different lengths: 0.930 ± 0.007, 1.930 ± 0.007, and 2.930 ± 0.007 in. All were coated with about 1.5 mils of nickel to protect them against oxidation, and to permit their being loaded into the cans while outside of a glovebox. Fabrication, including nickel coating and the subsequent welding, was to micrometric tolerances of the order indicated for the slug dimensions above. The cans were flat tubes of 0.013 ± 0.001-in. wall thickness, closed at each end by a flat and narrow end-closure strip.

Welding was by the inert-gas tungsten-arc method with the electrode mechanically driven. It was done in a simple, vacuum-tight chamber which contained a number of loaded cans and means for feeding the loaded cans, one at a time, from a hopper into a mechanically driven clamping chill which precisely held and positioned the cans for welding. The vacuum system enabled evacuation of air from the chamber and from the inside of the loaded cans contained therein. In operation, the hopper was first loaded with about 12 loaded cans, the chamber was sealed and pumped down to around 1×10^{-3} mm Hg, and the chamber back-filled to 16 in. Hg absolute with an equal volume mixture of helium and argon. The cans were then welded on one end, the chamber was opened, and the above cycle was repeated to make the final closure welds. In this way the cans contained a sealed-in charge of dry, inert gas which provided helium for leak testing as well as a protective atmosphere for the slugs.

A total of 397 slugs have been canned: 104 1-in. slugs, 198 2-in. slugs, and 95 3-in. slugs. All were well within the dimensional tolerances specified, e.g., 0.121 to 0.125 in. thick, 1.970 to 2.000 in. high, and ±0.010, -0 in. on the 1, 2, or 3-in. nominal length dimensions.

G. Development of Ceramic Fuel Materials

1. Uranium and Plutonium Monocarbides

Preparation by Powder Metallurgy Techniques (R. C. Lied and J. H. Handwerk)

Experimental test pieces of uranium monocarbide have been prepared by compacting mixtures of UO_2 and carbon and heating the compacts to 1600°C in vacuum. During reaction, carbon monoxide gas, which tends to slow the reaction due to the increased pressure in the system, is evolved. The product is a soft clinker containing 4.95 to 5.26 w/o carbon (stoichiometric UC has 4.80 w/o C) and 0.01 to 0.14 w/o oxygen. Tungsten arc melting of the clinker yielded a fused material with a bulk density of 13.25 g/cc (97% of theoretical), and carbon and oxygen contents of 5.1 w/o and 0.10 w/o, respectively. X-ray diffraction patterns contained strong UC lines plus weak UC_2 lines.

In a similar manner, plutonium oxide and carbon have been reacted in an attempt to form PuC. The powders were compacted and sintered at 1200°C. Some sintering was evident, but the treatment did not produce ware of good density or mechanical strength. Chemical analysis of the reacted material indicated a carbon content of 5.42 w/o.

Preparation by Arc-melting Techniques (O. L. Kruger)

Pieces of plutonium and spectrographically pure carbon were arc melted in an interchangeable hearth arc furnace. A deep hearth was used to melt the plutonium and carbon into 30-gram buttons. This hearth was then replaced with a casting hearth containing a graphite insert of the type used at BMI [2] for casting uranium monocarbide. The hearth was designed to eliminate contact of the melt with graphite until casting. The graphite insert was used for many castings without replacement. Cooling of the copper was enhanced by clamping the hearth to its holder with screws.

Skulls of the castings were cut off with a SiC wheel and the ends of the remaining pins were ground flat. The finished pins were about 1 in. long and 0.300 in. in diameter with a good surface. Chemical analysis indicates that an increase in carbon can be expected during melting. X-ray patterns and metallographic examination of arc-melted buttons containing 4.16 w/o C and 4.72 w/o C showed the presence of PuC and Pu_2C_3, with a small amount of another phase at the grain boundaries. The higher carbon alloy contained more of the Pu_2C_3 phase. In the lower carbon alloy the PuC formed as dendrites. The multiphase structures are presumably due to

---

[2] F. A. Rough and W. Chubb, Progress on the Development of Uranium Carbide-type Fuels, BMI-1370 (1959).

incomplete peritectic reaction. There was no indication that the material was pyrophoric; chips exposed for 3 weeks in an air atmosphere were only slightly oxidized.

Melting and Casting of Fuel Elements (R. M. Mayfield and J. K. Koeneman)

A study has been made of the feasibility of melting and casting plutonium-uranium monocarbide fuel elements in the Plutonium Fabrication Facility (Building 350). A review of power requirements and existing equipment indicated that a resistance furnace might be both easier to construct and more quickly attainable than an induction furnace. An existing bell jar and vacuum system furnace in Hood Line PF-14 is being modified for the high temperature required. Two sizes of double graphite helix resistance elements have been ordered from National Carbon Company. A five-layer tantalum-molybdenum-stainless steel heat reflector has been designed and bids for its construction have been solicited. A ring segment containing water-cooled and mineral-insulated power fittings was constructed and fitted to the bell jar furnace in PF-14. Temporarily, a 75-KVA welding transformer is being modified to power this furnace. Since fine control cannot be attained from this transformer, it may be desirable to replace it with a more easily controlled and instrumented power supply.

2. Urania-Thoria

Sintering and Oxidation Studies (E. D. Lynch and J. H. Handwerk)

The formation of solid solutions between U_3O_8 and ThO_2 upon heating in air was examined by weight loss and X-ray methods. Solid solution formation begins at 1000°C and the process is completed above 1250°C. Solid solution formation was accompanied by an increase in oxygen loss. Upon heating, mixtures of 70.4 m/o UO_2 (as U_3O_8)-29.6 m/o ThO_2 had an O/U ratio of 2.29 at 1350°C; upon cooling, the O/U value was 2.43 at room temperature. This corresponded to a solid solution composition of $U_{0.7}Th_{0.3}O_{2.30}$.

The change in O/U ratio during thermal cycling in air between 250 - 1250°C was determined for sintered solid solution specimens in the compositional range 30.5 m/o UO_2 (as U_3O_8) to 70.4 m/o UO_2 (as U_3O_8). Prior to cycling, these specimens had O/U ratios in the range 2.43 to 2.52. Thermal cycling resulted in O/U ratios of 2.34 to 2.38. These values correspond to solid solution compositions of $U_{0.3}Th_{0.7}O_{2.10}$ and $U_{0.7}Th_{0.3}O_{2.26}$.

A study of the densification behavior of air-sintered U_3O_8-ThO_2 and H_2-sintered U_3O_8-ThO_2 and UO_2-ThO_2 mixtures was initiated. The purposes were to determine the bulk density changes of 10 to 90 m/o UO_2-ThO_2 mixtures during sintering and to study the effects of composition and temperature on the stoichiometry of the solid solutions that are formed. Results

of this investigation are not yet complete, but preliminary studies show that additions of UO_2 or U_3O_8 up to 10 m/o promote the densification of thoria, while additions above 10 m/o and up to 50 m/o UO_2 or U_3O_8 retard the densification of ThO_2.

Irradiation Behavior (L. A. Neimark and J. H. Kittel)

Specimens of ThO_2 containing additions of 10, 30 and 50 w/o UO_2 and of 10 w/o molybdenum or niobium fibers have been irradiated, both bare and with lead or helium bonding in Zircaloy-2 jackets. Burnups were as high as 24,000 MWD/T, with calculated central fuel temperatures ranging from 2300 to 4000°C. Postirradiation examinations of the specimens have shown that, although a large percentage of the metal fibers melted at these temperatures, they effectively increased the thermal conductivity to allow greater cladding heat fluxes without damage to the pellet. It was found that the lead bonding between the pellet and clad allowed a greater average cladding heat flux before cladding burnout occurred than did helium bonding. Dimensional changes were of the order of 2% or less. Capsules containing the bare specimens will be sampled for fission gas release. A more detailed report of the above work was published in Nuclear Metallurgy, AIME, Vol. VI, 83-85 (1959).

Assemblies of ThO_2 pellets containing 6.36, 12.7 and 25.4 w/o UO_2, lead bonded to aluminum-1 w/o nickel alloy cladding, have been irradiated directly in MTR-ETR process water. Burnups ranged up to an estimated maximum of 50,000 MWD/T, with central fuel temperatures near 2000°C. Two specimens containing 25.4 w/o UO_2 were found to have developed longitudinal cladding failures. Metallographic examination is under way to determine the nature of the failures. Total fission gas release measurements on similar specimens with burnups to 20,000 MWD/T, showed approximately 14% release of the theoretical yield. The gas release from the lead-bonded assemblies appeared to be a function of the integrity of the lead bonding.

3. ZrO_2-CaO-UO_2 (D. C. Hill and J. H. Handwerk)

An investigation of fabrication techniques, solid solution formation, oxidation characteristics, and water corrosion behavior was conducted on a wide range of compositions of the ternary ZrO_2-CaO-UO_2 system in both oxidizing and reducing environments. Special emphasis was given to the zirconia-rich portion of the system.

Fabrication of specimens was performed by first sintering mixtures of U_3O_8, ZrO_2, and $CaCO_3$ in air at 1400 to 1700°C, crushing the sintered compacts by wet grinding in a porcelain pebble mill for 18 hours, followed by dewatering and drying of the slurry. The dry material was then

compacted at pressures ranging from 10,000 to 50,000 psi, and sintered in air or in H_2 at 1650 to 1750°C. The resulting sintered compacts had densities between 5.14 and 5.18 g/cc.

Microscopic examination reveals that the sintered compacts contain an estimated 8-10 v/o of phase which had been a liquid at the sintering temperature. This was attributed to alumina and silica contamination introduced in the milling operation. Figure 7 shows a typical microstructure of the liquid phase in these sintered compacts. To minimize the liquid phase, subsequent compacts were wet milled in rubber-lined pebble mills, using stabilized zirconia grinding media. Using this procedure of milling, specimens were obtained having densities greater than 90% of theoretical values, with essentially no liquid phase in them.

Figure 7

As-polished Microstructure of a ZrO_2-9.5 w/o CaO-5 w/o UO_2 Composition Sintered in Air at 1725°C for 4 Hours.

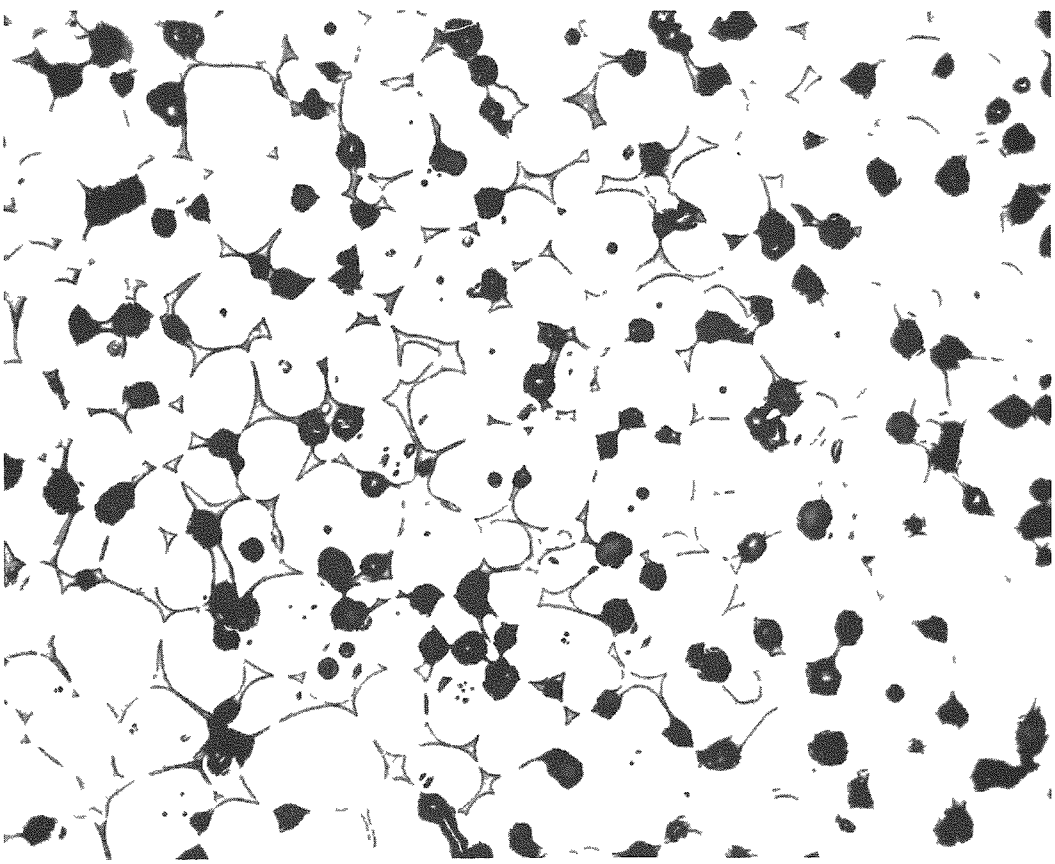

Micro 26065 250-X

Mixtures containing more than 40 w/o U_3O_8 were difficult to fabricate by air-sintering techniques. An intermediate reaction of U_3O_8, CaO, and oxygen takes place at temperatures as low as 900°C to form rhombohedral $CaUO_4$. This reaction has been noted to occur even in compacts containing as little as 10 w/o U_3O_8. The compound showed signs of instability at temperatures above 1300°C and its decomposition appeared to be dependent on compact composition and sintering temperature. Once decomposed, however, and a solid solution was formed at the high temperatures, no reformation of the compound was noted on cooling.

An extensive cubic fluorite solid solution area was found over a considerable portion of the ternary system for specimens sintered in a hydrogen atmosphere at 1750°C. Its limits are plotted on a mol percent basis in Figure 8. Unit cell dimensions for the system UO_2-$(Zr_{0.80}Ca_{0.20})O_{1.80}$ were found to obey Vegard's law (Figure 9). Air-sintered compositions showed a relatively small range of solid solubility in the stabilized ZrO_2 portion of the system. Solid solution area limits found by air sintering at 1450°C are shown in the cross-hatched portion of Figure 8.

Figure 8

Limits of Fluorite Solid Solutions in the ZrO_2-CaO-UO_2 System

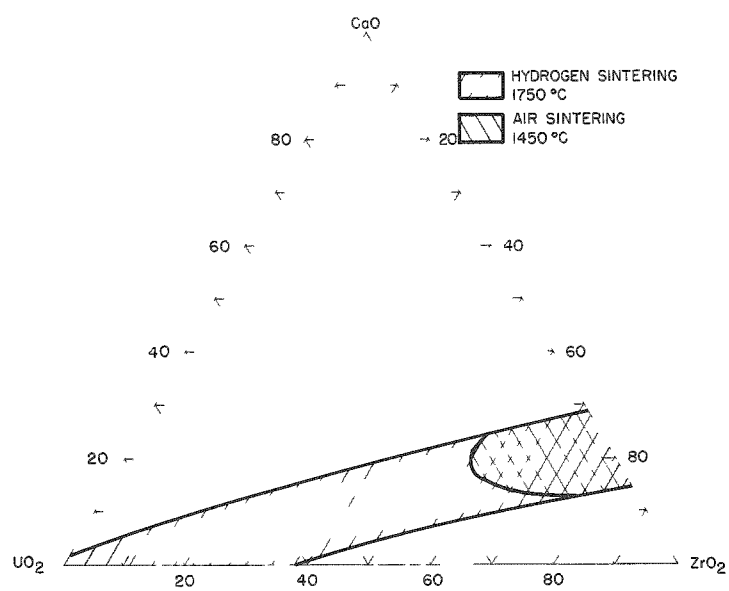

Compositions containing from 1.8 to 81.2 m/o UO_2, balance $(Zr_{0.80}Ca_{0.20})O_{1.80}$, and prepared by hydrogen sintering at 1650°C for 4 hours were crushed and oxidized in air at 800°C for 126 hours. The relation between mol percent $(Zr_{0.80}Ca_{0.20})O_{1.80}$ additions and resulting oxygen-to-metal ratios (calculated from weight gain data) is shown in Figure 10. The oxygen-to-metal ratio was found to increase approximately linearly to a value near 2.00 with increasing UO_2 contents up to about 25 m/o.

Compositions from 25 to 65 m/o UO_2 were found by X-ray diffraction to contain only the fluorite structure, even though the metal-to-oxygen ratio was greater than 2.00. Compositions containing more than 65 m/o UO_2 gave patterns indicating the presence of both orthorhombic U_3O_8 and the fluorite solid solution structure.

Figure 9

Unit Cell Dimensions for UO_2-$(Zr_{0.80}Ca_{0.20})O_{1.80}$
Solid Solutions Sintered in Hydrogen at 1750°C

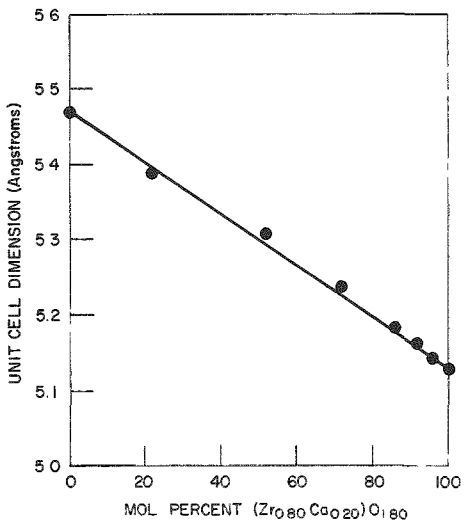

Figure 10

Oxidation Behavior of UO_2-$(Zr_{0.80}Ca_{0.20})O_{1.80}$
Solid Solutions

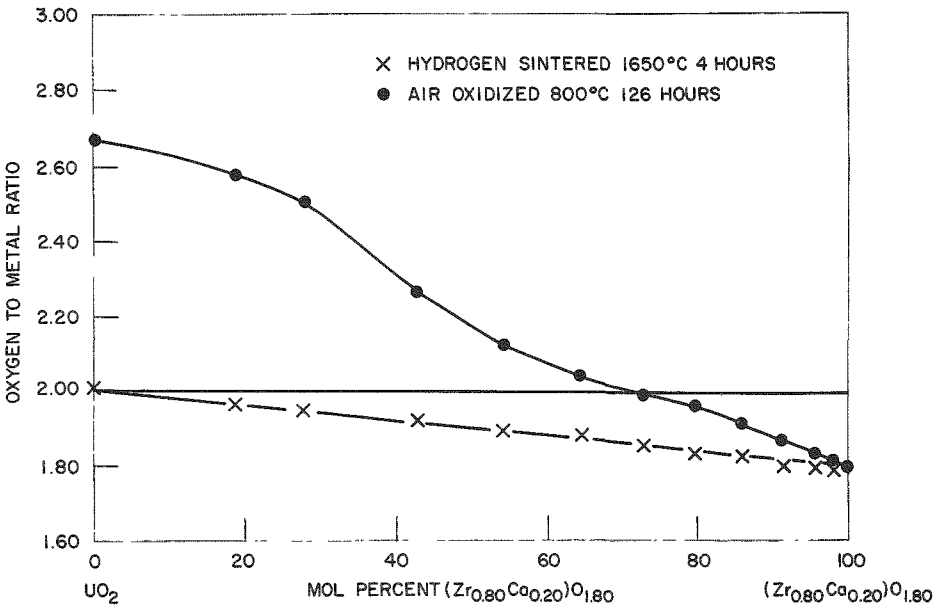

Low urania solid solution compacts exhibited good corrosion resistance to water and steam at elevated temperatures. Corrosion data for a ZrO_2-9.5 w/o CaO-5 w/o UO_2 specimen sintered in air at 1725°C are as follows:

Water Environment	Temperature (°C)	Exposure Time (days)	Average Rate of Weight Loss ($mg/cm^2/day$)
Degassed and Distilled	360	45.3	0.0050
Air-saturated Distilled	360	45.3	0.0019
Saturated Steam	540	41.4	0.0020

The samples tested had microstructures similar to that shown in Figure 7.

4. Uranium Sulfides (P. D. Shalek)

Uranium monosulfide powder was prepared by hydriding uranium at 245°C, dissociating it under vacuum at 550°C to yield a fine uranium powder, and then reacting it with a measured amount of H_2S at 550°C. The resulting mixture contains stoichiometric amounts of uranium and sulfur, but the main phases present are γ-US_2, UH_3 and α-U. The mixture was then heated to approximately 1800°C in a vacuum to homogenize it and to form the US phase. The homogenized powder contained 94.0 - 96.5 w/o US with some UO_2 or UO_2-U(OS) mixed phases.

The powder sintered readily. Pellets isostatically pressed at 55,000 psi have been vacuum fired at temperatures ranging from 1700 to 2150°C to densities from 66.5 to 95.1% of theoretical values. The high-density pellets showed a large grain size and sustained a 6 - 10% weight loss on sintering; both phenomena indicate overfiring.

H. Irradiation Evaluations of Various Experimental Fuel and Control Rod Materials

Restrained and Vented Uranium-2 w/o Zirconium Alloys
(J. A. Horak and J. H. Kittel)

Metallic fuels have been shown by numerous investigations to be subject to catastrophic swelling damage when irradiated above some critical temperature. For uranium-2 w/o zirconium alloys, the critical swelling temperature appears to be near 500°C. Swelling in metallic fuels normally is characterized by uniformly distributed porosity. Under severe irradiation temperature gradients, however, experiments at ANL have shown that a large central void can also be formed in specimens of various fuel alloys, including uranium-2 w/o zirconium alloy (ANL-5406).

With the above facts in mind, a group of uranium-2 w/o zirconium specimens were made to evaluate: (a) the ability of stainless steel cladding to restrain swelling of EBR-II size fuel pins, (b) the effectiveness of an axial core hole in preventing formation of a large central void, and (c) the ability of various types of vented end closures of the jacket to retain solid fission products released by the fuel pin. The diameter of the fuel in the specimens was 0.219 in. In order to achieve the desired temperature distribution, each specimen contained a 20% enriched, 0.094-in. diameter core. The axial core hole was 0.031 in. in diameter. The cladding was 0.010 in. thick and was NaK bonded to the fuel pin. It was separated from the fuel by a barrier of 0.001-in. thick zirconium foil. End closures included porous metal having effective pore sizes of 5, 20, and 65 microns, nonporous metal with drilled holes 0.005, 0.010, and 0.020 in. in diameter, and solid, leaktight closures.

Irradiations were made with calculated core burnups ranging up to 8.9 a/o and calculated temperatures ranging up to 820°C. Although the post-irradiation examinations are not yet completed, certain conclusions can be drawn from the experiments. Compared to unclad specimens, it was evident that the cladding enabled an approximate increase of 300°C in fuel irradiation temperature before excessive swelling occurred. The vented specimens released significant quantities of fission gas. Radiochemical analyses which will establish the ability of the various vented end closures to retain nonvolatile fission products have not yet been completed.

Aluminum-17.5 w/o Uranium-2 w/o Nickel-0.5 w/o Iron Alloys
(J. H. Kittel, R. Carlander and C. C. Crothers)

Although aluminum-uranium alloys have been used extensively for fuel in research and low-temperature test reactors, the alloys have not been used to any great extent in power reactors. Within the last few years, however, sufficient improvements have been made in the corrosion properties of aluminum alloys to merit interest in their use in fuel elements in power

reactors operating at moderate temperatures. The first power reactor to use these materials is the SL-1 reactor (formerly ALPR). Fabrication of the fuel elements is described in the 1958 Annual Report (ANL-5975).

In cooperation with the Reactor Engineering Division, an aluminum alloy plate similar to those fabricated for the SL-1 reactor was irradiated in the ANL-2 loop at MTR under nucleate boiling conditions. The purpose of the experiment was to determine the effects of heat fluxes and power densities a factor of 10 higher than those encountered in SL-1. The plate was 16 in. long, 2 in. wide, and 0.12 in. thick. The core was 0.050 in. thick and had a composition of aluminum-17.8 w/o uranium-2 w/o nickel-0.5 w/o iron. The cladding was an aluminum-1 w/o nickel alloy.

The plate was irradiated in water at 215°C for approximately 7 months. The maximum heat flux was approximately 700,000 Btu/hr-ft^2. Maximum analyzed burnup was 1.3 a/o. The irradiation was terminated because of a fission break which occurred after several days of operation in water at pH 9. The high pH value resulted from a defective ion exchange column.

A postirradiation metallographic examination of the plate indicated that the fission break occurred as a result of corrosive attack by the high pH coolant. The metallographic examination also disclosed an area near the hot end of the plate where fuel swelling had occurred. As far as it is known, no previous observation of swelling in aluminum-uranium alloys has been reported. The irradiation temperature of the swelled region was calculated to be 530°C, based on the measurements of fuel burnup, water velocity and temperature, scale thickness, and postirradiation measurements of scale thermal conductivity.

Zirconium-Plutonium Alloys (J. A. Horak)

Two zirconium-5 w/o plutonium and one zirconium-7 w/o plutonium specimens were irradiated to 1.4 and 1.9 a/o burnup, respectively, at a calculated initial temperature of 530°C. The alloys were cold rolled to size. According to the equilibrium diagram, the above compositions would be alpha-phase zirconium containing dissolved plutonium. All three specimens elongated considerably under irradiation, by approximately a factor of 3. Their ribbon-like appearance was very similar to irradiated pseudocrystals of alpha uranium. Pronounced longitudinal surface striations were evident.

Uranium-Molybdenum Alloys (J. A. Horak)

Irradiation studies with alloys of uranium with 2.5, 4, 6, 11, 14, and 17 w/o molybdenum will be started in 1960. The 2.5, 4 and 6 w/o alloys were fabricated by rolling at 850°C, the 11 w/o alloy was rolled at 725°C, and the 14 and 17 w/o alloys were cast to size. A variety of heat

treatments are being used for each alloy to produce all possible types of microstructures. The objective of the irradiation experiments is to determine the effect of composition and microstructure on the swelling temperature near 0.5 a/o burnup.

Aluminum-Dysprosium Oxide Dispersions (C. F. Reinke)

Compacts of Dy_2O_3 and aluminum-1 w/o nickel alloy powder containing 25 and 38 w/o Dy_2O_3, respectively, have been hot rolled. The resultant materials have densities 95% of theoretical. A metallographic examination of the finished plates indicated that there was no reaction between the Dy_2O_3 and the matrix. The irradiation stability and mechanical and nuclear properties of the materials are being evaluated.

I. Postirradiation Examinations of Full-scale Reactor Fuel Elements

A significant part of the engineering irradiation studies during 1959 was concerned with examinations of fuel elements removed from operating reactors. These examinations serve two very useful purposes. First, they enable comparisons to be made concerning actual fuel element performance compared to that which was predicted from prior irradiations of small specimens. Second, they provide information that is required in order to establish the additional useful life of a given operating reactor core. The following fuel element examinations were performed in 1959.

Borax-IV Fuel Plates (L. A. Neimark)

Five failed Borax-IV fuel plates, previously found to be leakers by bubble testing, were sectioned and the released fission gas was collected. The fuel elements for Borax-IV are tube-plates of aluminum-1 w/o nickel alloy containing pellets of ThO_2-6.36 w/o UO_2, lead bonded to the aluminum alloy cladding. Absence of fission gas and helium in many tubes indicated that more tubes had leaked gas then the bubble testing method had revealed. The average total gas release from those tubes that yielded gas, including approximately 1.1 cc of helium filler gas, was 3.3 cc at STP per tube. The gas will be assayed for Kr^{85} content. Microscopic examination of the failed areas verified the presence of cracks in the collapsed tubes that showed leaks during the bubble test. No cracks were evident in those tubes that yielded little, if any, fission gas, indicating that the leak in these tubes is of a different nature. Further metallography on the failed sections is in progress. The estimated burnup of the fuel was 980 MWD/T.

EBWR Fuel Elements (C. F. Reinke)

Two fuel assemblies were removed from the EBWR and examined in a hot cell. The assemblies had burnups of 0.11 and 0.37 a/o, respectively. Both were disassembled and sampled for the evaluation of the effects of

in-pile operation and radiation damage to the fuel. The assemblies were in good condition with no ruptured cladding, core-clad nonbonds or excessive fuel plate swelling or warpage present. After 0.37 a/o burnup, the fuel cores were hard, brittle, and highly stressed. The rate of fuel plate volume increase due to the fission of uranium was 6 to 7% per a/o burnup. Hydrogen was picked up by the fuel plates under reactor operating conditions with preferential deposition at the colder edges of the plates and resultant hydride formation. Annealing studies on sections of irradiated fuel plates at 500 and 550°C indicated bulk volume increases of 1 to 2% and 5 to 10%, respectively, after 500 hours. A 600°C anneal resulted in a bulk volume increase of 18% after 50 hours. The annealing studies were made to help evaluate the ability of the present irradiated core to operate at the recently authorized increased EBWR power level of 100 Mw.

Elk River Reactor Element (L. A Neimark)

A full-size prototype assembly for the Elk River Reactor was supplied by American Car and Foundry, and after irradiation in the EBWR it was examined in the hot cell facilities. The assembly consisted of 25 stainless steel tubes, containing ThO_2-3 w/o UO_2 pellets surrounded by a helium annulus, arranged in a five-by-five array. The burnup has not yet been analyzed, but was relatively low. Dimensional changes of the assembly and tubing were insignificant, the greatest diametrical increase in any one tube being 2.0%. Transverse fracture sections through representative tubes showed no central melting or void formation in the ceramic fuel. The average total gas content of representative tubes, including approximately 4.3 cc of helium filler gas, was 7.6 cc at STP per tube. The gas will be assayed for Kr^{85} content.

EBR-I Core-3 Fuel Elements (J. A. Horak)

The fuel in the third core of EBR-I consists of uranium-2 w/o zirconium alloy rods coextruded with 0.020-in. thick Zircaloy-2 cladding. After approximately 0.1 a/o burnup, measurements performed by the Idaho Division showed that diameter increases of the fuel rods had occurred. The diameter increases ranged up to approximately 0.005 in.

In order to determine the source of the diameter increase, two irradiated rods were sectioned for density measurements and metallographic examinations. It was found that only about one-third of the increase in diameter could be accounted for on the basis of the measured decreases in density of the fuel resulting from irradiation. It appears, therefore, that most of the diameter increase is due to "upsetting" of the fuel. This could be caused by the weight of the extension rod on the fuel section, or because the fuel rods have been so rigidly clamped in the core that longitudinal thermal expansion has been prevented.

J. Development of Corrosion-resistant Fuel and Jacketing Materials

1. High-temperature Corrosion-resistant Aluminum Alloys (W. E. Ruther and J. E. Draley)

As discussed in the 1958 Annual Report, alloys of apparently equal nominal compositions have shown considerable variation in corrosion resistance to 350°C water. Possible variables were studied during the past year and the significant factor was shown to be the trace silicon concentration.

A vacuum-melted Al-1 w/o nickel-0.5 w/o iron-0.1 w/o titanium alloy was prepared using 99.99+ aluminum. It was chill cast, rolled, and then cut into pieces. Remelts of this material with minor additives were made in an inert gas tungsten-arc furnace. Corrosion tests were performed in a 350°C autoclave (water saturated with O_2 at room temperature). Samples were removed after about 1-month and 2-month exposures. The alloys were evaluated by the slope of the line connecting the metal loss values for these two time periods. The corrosion results for some of the alloys are shown in Figure 11.

Figure 11

Effect of Small Additions of Alloying Elements on the Corrosion of Al-1 w/o Ni-0.5 w/o Fe-0.1 w/o Ti Alloy in Water at 350°C

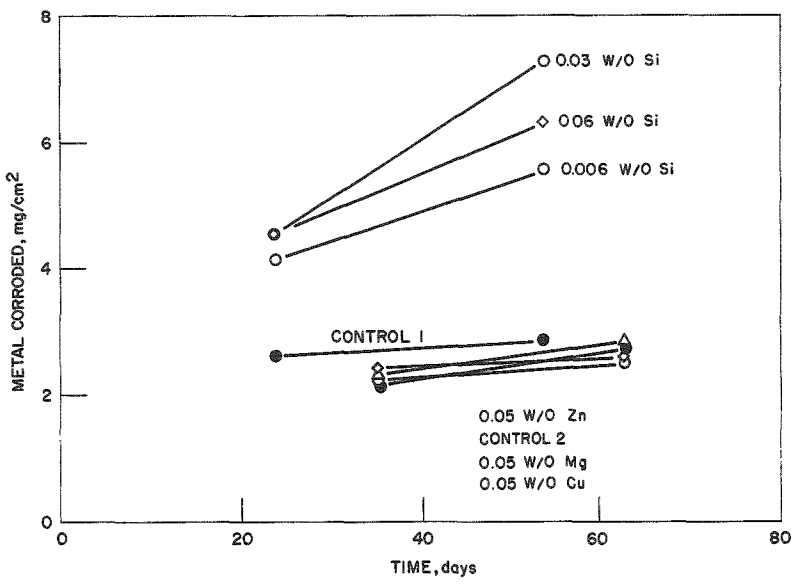

The influence of traces of magnesium, zinc or copper (common impurities in aluminum) on the corrosion rate was very small. By contrast, the influence of silicon was very large. The marked corrosion

transition range was from zero to 0.006 w/o silicon. At concentrations of about 0.002 w/o, a slope of ~½ mdd was noted. At 0.006 w/o, the rate had increased to about 5 mdd. Additional silicon makes relatively smaller changes in the rate. For example, a 10% alloy (not shown) had a rate of ~ 6 mdd.

Since the content of silicon is of some importance, a long-time continuing test of an aluminum-1 w/o nickel-0.5 w/o iron-0.01 w/o titanium alloy made with very pure aluminum (0.001 w/o silicon) was started in June. The autoclave was operated at 350°C, with constant refreshment with water saturated with oxygen at room temperature. Samples have been removed at 1-month intervals and the metal loss determined by defilming. The values obtained show a usual small scatter but the slope of the line connecting the points is very low or even zero. Total metal loss is about 0.0005 in.

Unfortunately, the low metal loss rates at 350°C are not obtained at 290°C (and presumably lower temperatures). Coriou[3] has shown that the heat treatment of Al-Fe-Si alloys greatly influences their corrosion behavior due to the redistribution of the silicon. It was hoped that some effect of this nature might be responsible for the difference in behavior between tests at 290 and 350°C. There was also the possibility that the formation of a different oxide film (diaspore or corundum) next to the metal was essential to the low rates and that these oxides formed slowly or not at all at 290°C. To check this point an alloy was corroded for one month at 350°C (to establish the film) and then transferred to a 290°C test. The various pretreatments were as follows:

Alloy	Treatment
Al-1 w/o Ni-0.1 w/o Ti (A198x)	29 days at 350°C; air cool
	6.8 days at 400°C; air cool
Al-0.9 w/o Fe-0.6 w/o Ni-0.1 w/o Ti (A297)	6 days starting at 400°C and reducing slowly to 275°C; furnace cool
	Corroded 35 days in 350°C water
Al-1 w/o Ni-0.5 w/o Fe-0.1 w/o Ti (A293)	7 days at 400°C; air cool

Subsequent corrosion tests at 290°C did not show any improvement for the pretreated specimens over the controls, except for the 350°C precorrosion. In this case there was a brief induction period before the samples corroded at a rate equivalent to the controls.

[3] H. Coriou, L. Grall, A. Hauptman and J. Huré, Rev. de Met. Vol. LV, 968 (1958).

The corrosion product film was investigated for clues to this inverse temperature-corrosion rate relationship. Microscopically, the difference in the oxide-metal interface for the better alloys is pronounced between metal corroded at 290 and at 350°C. At 290°C the film is duplex, with a glassy layer adjacent to the metal and friable porous layer attached to the water side of the glassy layer. Metallic particles of an uncorroded phase are frequently seen in the glassy layer. A maximum number of particles are noted near the metal, and the number diminishes to zero near the interface between the two oxide layers. The attack on the metal is relatively smooth. The above description fits the low silicon alloys at 290°C and the "high" silicon (>0.01 w/o) poorer alloys at both 290 and 350°C.

The low silicon alloys at 350°C show a completely different corrosion interface. A dark compact layer is adjacent to the metal but with no imbedded metallic particles. Intergranular penetration takes place to the depth of a few grains. Fingers of dark oxide have been shown to follow the lines of the second phase compound into the sample. On the water side of the compact corrosion product, a loosely attached plate of white boehmite is formed. Since the attack appears to concentrate on the second-phase areas, a fine dispersion of this phase prevents serious penetration of the metal at any point, and seems to effectively stifle the overall corrosive attack.

Chemical analyses of corrosion films prepared at the two temperatures also indicated differences. The adherent oxide film from 350°C corrosion contained up to 6% more aluminum and up to 100% more nickel and/or iron than would be calculated from the composition of the alloy. The products of corrosion were assumed to be $\alpha Al_2O_3 \cdot H_2O$, NiO, and FeO. One corrosion product was analyzed (after removal of the uncorroded metal by the methanol-iodine method), then pulverized and treated again in the methanol-iodine solution. The analysis of the oxide after the second treatment was much lower in aluminum than after the first treatment. This suggested that the films contained pieces of uncorroded metal.

The loosely attached plate of corrosion product was shown to have the exact aluminum content of boehmite and to be very low in nickel content. The aluminum, iron and nickel contents of corrosion product prepared at 290°C were only slightly higher than the calculated values. It may be that the presence of relatively large amounts of uncorroded metal in the film are essential to the low rates. Currently, a test with an alloy containing palladium (to supply uncorroded metal) is being performed at 290°C to check this hypothesis.

Dynamic Testing: Data for a continuing dynamic test of X8001 alloy in 315°C, pH 3.5, H_3PO_4 solution at 18 feet/second have been obtained through 188 days. The average metal loss of four specimens which have been in test for the entire period is shown in Figure 12. The metal loss has

Figure 12

Dynamic Corrosion of X8001 Aluminum in pH 3.5 Phosphoric Acid at 315°C and 18 feet/second

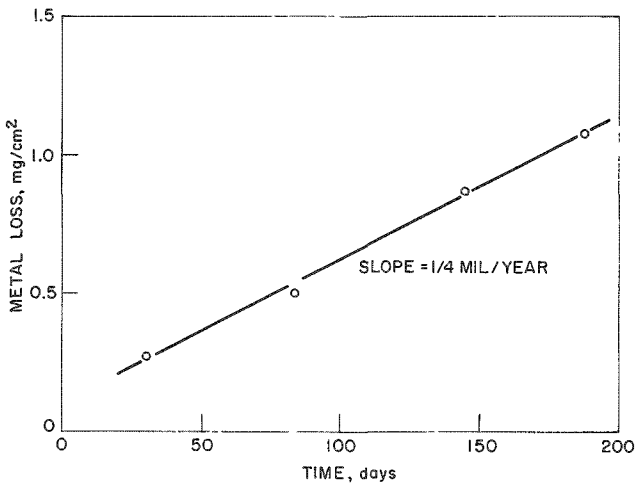

been calculated from nondestructive eddy current measurements and checked by actually defilming other test specimens. The corrosion rate is about $\frac{1}{4}$ mil per year. The only unusual corrosion feature noted was a pit between two of the specimens. It did not enlarge after the specimens were removed for the first inspection.

Powder Metallurgy: Because of the difficulty of securing laboratory-size batches of atomized aluminum alloys, a small atomizer was built and used to produce low-silicon atomized aluminum alloy powders. The atomized powder, with or without additives, was made into corrosion test specimens by hot rolling in an aluminum can. These products have the same adherent dark oxide as the wrought low-silicon alloys, and in a five-month continuing test they showed the same very low corrosion rate at 350°C. Samples made from commercially supplied X8001 powders were removed from test after 2 months due to severe edge swelling.

Mechanism: Dillon's[4] interesting hypothesis concerning the role of the intermetallic particles as stress relief points in the aluminum oxide film has inspired some experimentation. Powder metallurgy was used as a method of preparing a product with a relatively fine dispersion of "grit." In one case the grit was nonconducting fused ZrO_2 powder and in a second product it was electrically conducting fused TiO2 powder. If the stress relief hypothesis is correct, one would expect that these two products would corrode similarly. If an electrochemical mechanism operated, as we have previously suggested, the TiO_2 should provide some measure of protection. The results tend to favor the electrochemical hypothesis, as shown in Table III, as far as protection is concerned. The lower weight gain of the ZrO_2 product at 150°C is not in keeping with the other results, and may represent some product lost to the solution.

Corrosion in Superheated Steam, 540°C, 600 psi: Two interesting effects were found in this corrosion medium. First, many different aluminum alloys will resist destruction in short tests when they are sitting on a perforated stainless steel plate and will disintegrate in the same

[4] R. Dillon, Private Communication, HAPO.

location when they are suspended by a rod through a hole in the specimen. The hole is not the important factor as control samples have shown. Since the metal is very weak, it is believed that the strain resulting from the tensile or shear stresses due to the weight of the specimen initiates the disastrous attack. Specimens of Al-5.5 w/o Ni-0.3 w/o Fe-0.1 w/o Ti (203 composition) with low silicon content are able to withstand the hanging specimen test much better than specimens with silicon contents of 0.03 and 0.06 w/o.

TABLE III

Corrosion of Aluminum with Oxide Additives

Sample	Corrosion
99.99+ Al powder, passed #100 sieve but not # 325, plus 6.6 w/o fused TiO_2 powder which passed #325 sieve (44 microns). Reduction in area 36:1	150°C H_2O, 1 day - metallic appearance; Weight gain = 2.0 mg/cm^2. 200°C H_2O, 1 day - grey film; large blisters filled with solid oxide; sample not distorted. 290°C H_2O, 1 day - completely converted to powdery oxide.
99.99+ Al powder of same size as above plus 6.6 w/o fused ZrO_2 of same size as above. Reduction in area 24:1	150°C H_2O, 1 day - metallic appearance; Weight gain = 0.3 mg/cm^2. 200°C H_2O, 1 day - completely converted to oxide layers, partially split apart. 290°C H_2O, 1 day - completely converted to powdery oxide.
Control, 99.99+ Wrought Al.	150°C, 1 day - dark grey film; Weight gain = 3.4 mg/cm^2. 200°C, 1 day - very distorted; sample appears to be all white oxide. 290°C, 1 day - completely converted to white powder.

A second effect was noted with respect to the hydrogen content of the corroded specimens. Previous test results have indicated contents between 2 and 3 ppm after various exposure times. There has been a question as to whether this represented an equilibrium value. However, all the previous tests were made with specimens of approximately the same size; hence the surface of the sample to volume of the metal remained nearly constant. An experiment in which this ratio was deliberately varied

produced the results shown in Figure 13. Since the final hydrogen content is shown to be dependent on the surface-to-volume ratio, it is now assumed that the hydrogen in the specimen is some fraction (to be determined) of the corrosion product hydrogen which is prevented from escaping by an impervious oxide film.

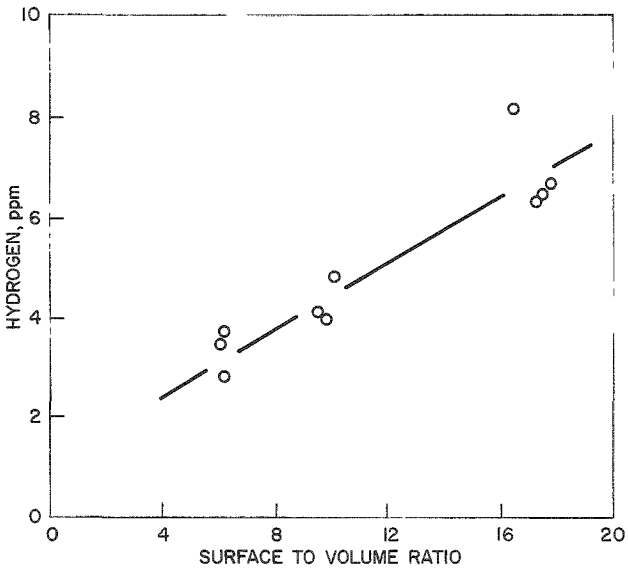

Figure 13

Hydrogen Content as a Function of the Surface-to-Volume Ratio of Samples Corroded in Superheated Steam at 540°C, 600 psig.

2. Uranium Alloys (S. Greenberg and J. E. Draley)

Uranium-Titanium Alloys: Additions of niobium to uranium-3 w/o titanium alloys have been found to lower the corrosion rate in 260-290°C water when the alloys are in the gamma-quenched condition. The optimum niobium content is about 0.5 w/o. Larger amounts (up to a few percent) showed no further improvement in observed corrosion rates, and the alloys were more subject to cracking during corrosion testing.

Although such gamma-quenched alloys have low corrosion rates, cracking or other failure occurs during corrosion following annealing thermal treatments. The addition of as little as 0.1 w/o ruthenium was found to provide considerable resistance to the loss of corrosion properties during heat treatment. A sample of the optimum composition (U-3 w/o Ti-0.5 w/o Nb-0.1 w/o Ru), heat treated 2 hours at 400°C following gamma quenching, has been corroding in water for 80 days at 260°C plus 20 days at 290°C with no cracking or other damage. Corrosion rates have been about $1\frac{1}{2}$ mcd at 260°C and 4 mcd at 290°C. The ruthenium has a similar stabilizing influence on the U-3 w/o Ti alloy in the absence of niobium. In this case, corrosion rates are slightly higher.

Effect of Radiation on Corrosion: Sections of an EBWR plate, clad on two faces with edges bare, have been tested in degassed, distilled water at 260-270°C. The results are summarized below. The results for

an unirradiated sample of the core alloy (U-5 w/o Zr-1.5 w/o Nb) are included for comparison. The burnups are based on radiochemical analysis. The "corrosion rates" are based on the original exposed area of the uranium alloy. Because of the rapid decrease in area accompanying the high corrosion rates, the reported rates are much lower than the actual corrosion rates; however, these "rates" are useful for purposes of comparison.

Sample No.	Burnup (Total a/o)	Corrosion Rate (mcd)
--	0.000	9470
1	0.005	2500
15	0.009	2780
13	0.017	2310
12	0.024	1880
10	0.088	1890
6	0.14	5160

Additional samples are now available to continue this interesting study. At the present time, however, there seems to be sufficient evidence to indicate that radiation-induced changes improve the corrosion resistance of the U-5 w/o Zr-1.5 w/o Nb alloy that has been heat treated for dimensional stability.

3. Zirconium Alloys for Use in Superheated Steam (S. Greenberg and J. E. Draley)

It has been shown that zirconium and the Zircaloy alloys have poor corrosion resistance in steam at 540°C, 600 psi. Since Zircaloy-3 was better than Zircaloy-2, it is concluded that the presence of tin is deleterious; since these alloys are not as bad as unalloyed zirconium, it is inferred that one or more of the other alloying constituents are beneficial.

Some binary and ternary alloys have been tested using arc-melted, as-cast samples. The best alloying constituents tested to date are nickel, iron, and copper. For example, a ternary alloy containing 3 w/o nickel and 0.5 w/o iron had an average rate of weight gain of 1-2 mdd after 35 days, and was covered with a black film. Zircaloy-3, the best commercial alloy, was covered with heavy loose white oxide after 10 days. After an initial period of weight loss, the rate of weight gain was greater than 265 mdd.

4. Structural Materials in Acid Environments (S. Greenberg and J. E. Draley)

1100 aluminum has been found to have a very high corrosion rate in nickel-containing acid solutions, as indicated in Table IV.

TABLE IV

Corrosion* of 1100 Aluminum at 315°C in Nickel-containing Acid Solutions

Time (days)	Condition	Corrosion Rate (mils/year)
26	pH 3.5; 4 ppm Ni as sulfate	7
15	pH 4; 1.8 ppm Ni as sulfate	12

*Refreshed system. Static conditions. Corrosion rate determined by stripping in methanol-iodine.

The samples were severely blistered, especially around the drilled mounting holes, and there was considerable salt deposit on them. Blistering and salt deposition were more severe in the solutions of higher pH. Under these conditions, the 18-8 stainless steels (304 and 347) and Zircaloy-2 and -3 showed no measurable weight changes during the last two weeks of exposure. For the first week, the rate for the stainless steels was 0.2 to 0.4 mil/year. The Zircaloys gained weight during the initial period at a rate of 1 to 2 mdd.

Stainless steel and the Zircaloy alloys have also been tested in a refreshed system at 315°C for about 6 months in degassed phosphoric acid of pH 3.5. The corrosion rates of the 18-8 stainless steels (304, 316, and 347, annealed and sensitized) were very low under these conditions. As measured by weight changes of the samples, the rates were less than 0.1 mil/year. The test has been stopped and the samples will be stripped in an effort to obtain corrosion rates. Under the same conditions, Zircaloy-2 and -3 also have weight loss rates less than 0.1 mil/year. Couples of stainless steel and X8001 aluminum show no adverse effects in this solution.

K. Nondestructive Testing Developments

1. Instrumentation for Elastic Constants Measurements (R. A. DiNovi, R. Peterson and C. J. Renken)

Design and construction of electronic equipment to be used in the precise determination of elastic constants of single crystals are under way. The equipment is based on the system developed by Bell Telephone Laboratories using ultrasound in the range from 12 to 150 megacycles/sec. The master oscillator and gate generator have been built and tested. The gated harmonic generator is complete up to the 25 megacycle stage. The velocities of the various modes of propagation can be determined from precise frequency measurements.

2. Cladding Thickness Measurements (W. J. McGonnagle and R. Perry)

Beta backscatter has been investigated for measuring cladding thickness. When beta rays impinge on materials, the electrons are reflected or backscattered, and the number of backscattered particles is proportional to the target thickness. The intensity of backscattered radiation increases with increasing thickness of target material until the thickness equals approximately one-fifth of the range of the electrons in the material. A further increase in the thickness does not increase the intensity of the backscattered radiation. If a second layer of material having a different atomic number is placed upon the first material, the counting rate will change. The counting rate will increase for the second material with a higher Z and will decrease if the Z is lowered, provided the thickness of the base material is at least one-fifth of the range of electrons in the base material. The greater the difference in atomic number between the two materials, the greater the difference in the counting rate and consequently the sensitivity of the measurement.

3. Eddy Current Studies (C. J. Renken)

Early in 1959, an extensive series of experiments was undertaken to determine the ability of eddy current test systems to detect flaws in metals. Flaw size, metal resistivity, and frequency of the eddy current fields were used as the test variables in these experiments. From the results, it was concluded that one of the most important faults in conventional eddy current equipment was the lack of resolution of the test probe. By resolution is meant the ability to detect separately closely spaced defects, or to detect defects small in all directions. A search was undertaken for ways to improve resolution. After a considerable number of unsuccessful experiments it was discovered that the fields generated by the test probe could be masked down to a very small cross-sectional area by the use of masks of special design. At the same time, the peak power of the field was increased by using high-amplitude short-time duration driving currents in the test coil.

One use for these fields of small cross sectional area is in the through-transmission technique. In this technique the pulsed fields are transmitted through the metal and are detected by a pick-up coil on the opposite side. Either the attenuation of the field, or the amount it is delayed in passing through the metal, can be used as an index of conditions inside the metal; however, the delay measurements are singularly free from the influence of all test variables except those which relate to the inside of the metal. Automatic delay measurements have been used in a successful through-transmission test of a quantity of X8001 aluminum tubing for use in an experimental subassembly of the EBWR.

The discovery of a method of masking the low-frequency fields used in eddy current testing has also made it possible to develop a test of improved sensitivity and resolution for use on tubing. In this technique, the masked field is caused to impinge on the surface of the tube. It travels around the circumference of the tube for some distance and is detected by a pick-up coil. The amplitude of the voltage induced in the pick-up coil is a function of the internal condition of the metal under the aperture of the mask. An auxiliary pulsed field is used to balance out any effect of changes in the diameter of the tubing on the main field. This method is applicable to tubing of practically any diameter. It has been highly successful in detecting cracks in Zircaloy-2 tubing of the type to be used in experimental elements of the EBWR.

L. Metallurgical Assistance to the Fast Reactor Safety Program
(R. A. Beatty and C. H. Bean)

The Metallurgy Division rendered assistance to other divisions in the Laboratory in connection with the Fast Reactor Safety Program by providing services in the fabrication, testing, and evaluation of a variety of experimental structural, reflector, control, and fuel materials. A summary of the work on this program during the past year follows.

Structural Materials

Two Zircaloy - 3 ingots weighing 3138 lb have been ordered converted to strip by Superior Steel Company in anticipation of requirements for 100 fuel test cans, 9 ft long, to be used in TREAT. The yield of finished material was higher than anticipated, with the result that 2157 lb of strip were obtained. Because of a change in handling test containers and delay in starting meltdown tests on EBR-II-type fuel pins, only four of the 9-ft long test containers have been fabricated to date. Additional containers will be needed in the future.

A total of 36 ft of $1\frac{1}{2}$-in. OD x $\frac{1}{8}$-in. thick wall Zircaloy-2 tubing was fabricated for use by the Reactor Engineering Division for meltdown specimen containers. Inspection of the tubing was performed by the Metallurgy Division; the tubing was found free from internal defects.

Three series of graphite cylinders with inserts and end plugs to be used as containers for TREAT meltdown specimens were outgassed under vacuum for 12 hours at 900°C.

Reflector Materials

Concern about possible excessive moisture content in reflector graphite, which had been stored without protection from the weather prior to installation in the reactor, led to a series of measurements on moisture content from a random sampling of blocks removed from the reactor. Information received from National Carbon Company indicated that graphite which had been stored in this manner could absorb from 0.5 to 3 w/o water. A series of eight reflector blocks, 4 in. square x 24 in. long, were dried for 24 hours in an evacuated container at 200°C. Measurements were made of weight losses from each block and weight gains in a zeolite-type desiccant used to collect the moisture removed from each block. Good correlation was obtained between the two measurements. Moisture content in the blocks ranged from 0.007 to 1.81 w/o.

In another test it was established that, under ideal conditions for saturating the graphite with water, graphite could be made to absorb as much as 13.5 w/o.

Control Materials

Eight batches of graphite-poison dispersion-type compacts were outgassed in vacuum prior to being sealed in aluminum cans for testing in the core of the reactor. Weight losses for each type of material were as follows:

Poison Material	Outgassing Temp. (°C)	Wt. Loss (grams) (Avg. for 8 Blocks)
Pure Graphite (standard)	900	Not measured
CdO	300	0.49
In_2O_3	800	1.86
Sm_2O_3	800	1.65
Gd_2O_3	800	1.89
Dy_2O_3	800	1.61
Er_2O_3	800	1.10

Fuel Materials

A variety of uranium and uranium alloy pin-type specimens for meltdown and metal-water reaction experiments were requested by the Chemical Engineering Division. The following specimens have been fabricated and delivered during the past year to the Chemical Engineering Division:

	Uranium Type	Quantity
Unalloyed uranium without cladding	Normal	12
Unalloyed uranium without cladding	20% Enriched	12
93.5 w/o U + 5 w/o Zr + 1.5 w/o Nb without cladding	Normal	12
93.5 w/o U + 5 w/o Zr + 1.5 w/o Nb without cladding	20% Enriched	12

Specimens currently in preparation and about 60% completed are:

	Uranium Type	Quantity
10.0 w/o UO_2 in CaO + ZrO_2 matrix clad with Zircaloy-2	20% Enriched	15
10.0 w/o UO_2 in CaO + ZrO_2 matrix clad with stainless steel	20% Enriched	3
10.0 w/o UO_2 in CaO + ZrO_2 matrix clad with X8001 Al	20% Enriched	3

Eighteen test pins were fabricated with 0.200-in. diameter x 0.480-in. long fuel slugs sealed inside 0.020-in. thick Zircaloy-2 cans containing a small hole in the bottom of each can. The hole in each of 9 cans was 0.003 in. in diameter, and in each of the remaining 9 cans it was 0.015 in. in diameter. Sixteen pins contained 20 w/o enriched U-5 w/o Zr-1.5 w/o Nb alloy cores; the remaining two contained highly enriched unalloyed uranium.

EBR-II-type Fuel Pins for TREAT Meltdown Experiments
(A. B. Shuck)

Injection-cast uranium-5 w/o fissium alloy pins of three enrichments - 3, 4.1, and 6 w/o U^{235} - were prepared at the request of the Reactor Engineering Division for TREAT experiments. The pins were made using the same injection-casting equipment and the same procedures described elsewhere in this report in connection with the fabrication of the first loading for EBR-II. The castings were cut to length, using a lathe to obtain the maximum yield of usable material. Final inspection included diametral gaging with an air gage and eddy current examination for internal porosity. Where full length pins could be supplied, they were cut to 14.22 in. length. Where shorter lengths were cast or where flaws appeared, short pins were supplied of the maximum length possible to exclude all imperfections. A total of 195 pins have been supplied.

M. Miscellaneous Developments

1. Brazing Alloy for Zirconium (F. D. McCuaig, R. D. Misch and R. A. Noland)

The objective was to develop a brazing alloy for zirconium containing no toxic alloying elements such as beryllium, and possessing a corrosion resistance to water and sodium equivalent to that of Zircaloy-2. It was also required that the alloy be fully molten below 1000°C. An alloy containing 84 w/o zirconium, 8.0 w/o nickel, and 8.0 w/o chromium has been developed satisfying the above criteria. Its liquidus and solidus are at approximately the same temperature, 950°C. Like other zirconium-base brazing alloys, it is somewhat brittle, especially under impact loading. Thus, the material is best applied where joint clearances are small. The alloy has been found to be useful for sealing purposes, as in making seals between thermocouple protection tubes and element closures. A number of seals between stainless steel and Zircaloy, and tantalum and stainless steel, have been made with good success. These applications required limiting the time at the brazing temperature to minimize dissolution of the stainless steel by the braze.

2. Brazed End Closures for CP-5 Core (S. J. Matras and R. A. Noland)

Problems encountered by a commercial fuel fabricator in controlling the fuel core configuration at the core ends in the aluminum-clad, aluminum-uranium core, tubular fuel elements for CP-5 prompted an investigation of techniques for providing suitable end closures. A number of approaches were investigated, including butt welding, silicon bonding, inert gas tungsten-arc welding, and several variations of brazing. Of the methods examined, dip brazing in flux has succeeded in producing a number of apparently suitable closures, although refinements in the technique are still being made.

3. Calorimetric Assay of Plutonium-containing Specimens (S. Rosen and A. B. Shuck)

The fabrication of plutonium-bearing fuel elements by processes such as coextrusion or casting directly into jackets requires that an accurate, nondestructive method of assaying such specimens for plutonium content be developed. Measurement of the heat generated by radioactive decay of the plutonium offers an attractive solution of this problem. A calorimeter of the nonsteady state rating type has been constructed and tested. Results of measurements with various modifications of the original instrument have indicated that an accuracy of better than 1% is obtainable. The time required for determination is one-half to one hour. A more elaborate twin calorimeter has been constructed for comparative measurements and performance evaluation with the rating calorimeter.

A second rating-type calorimeter has been designed. Automatic instrumentation for this calorimeter, with which it is hoped to simplify and accelerate the assaying process, has been ordered.

PART II

BASIC METALLURGY

A. Preparation of High-purity Materials

1. Plutonium (M. B. Brodsky)

During the past year, two additional experimental electrolytic cells have been developed for the preparation of high-purity plutonium.

Cell III: This cell was made of Vycor and was operated to check the reproducibility of the high-purity plutonium produced in Cell II, and to determine the effect of using specially dried KCl-LiCl eutectic. Enough salt, containing less than 4 ppm water, was prepared for use in the cell and for melting down all deposits. Molybdenum cathodes were used, as in Cells I and II.

Seven plutonium buttons, weighing a total of 179 grams, were prepared in 17 runs during 12 days. The overall efficiency of the cell, defined as the weight of plutonium produced divided by the sum of all anode weight losses and the initial plutonium content of the electrolyte, was 46%. This may be compared to an efficiency of 33% for Cell II. An average recovery of 72% was obtained for the last 13 runs of Cell III, which is comparable to that obtained in the final runs of Cell II.

It was not possible to determine the effects of cell variables on product purity because of difficulties with anodes falling out of their holders during six of the runs. Additional plutonium could have been prepared without exceeding the criticality limit of 300 grams, but it became necessary to discontinue operation because of furnace cooling water failure.

Cell IV: This Vycor cell had a 2-in high Vycor plate sealed across its bottom to prevent any insoluble matter which might exfoliate from the anodes from coming in contact with the cathode. Tantalum strips, which were irradiated in CP-5 to an nvt of 4.2×10^{14} neutrons/cm^2, were used as cathodes. Although a KCl-LiCl-PuF_4 bath was used again, most of the deposits were melted in 50-50 mole percent KCl-NaCl.

The cell has been in operation for 5 weeks, and a total of 270 grams of plutonium have been recovered in 22 runs, with an overall efficiency of 58%. Plutonium recovery has averaged 89% for the last 19 runs, and therefore it should be possible to produce up to 600 grams of metal with this cell before the criticality limit is reached. Should it be desirable to run the cell beyond that point, it would be possible to reduce its plutonium content by electrodeposition without the use of a plutonium anode. In one such electrolysis run in Cell IV, a deposit which yielded a 1.93-gram button was recovered in one hour at a cell current of 2 amperes.

Analyses: The analytical data for material produced in Cells II, III, and IV are given in Table V, along with the operating conditions of the

TABLE V

Analyses of High-purity Plutonium

Sample Identification	High Purity	Anodes for Cell II	Anodes for Cells III & IV	M7	M9	M12	M15	M16	M19	M20	M21	M22	M23	M27
Preparation Method	Bomb Reduction	Bomb Reduction	Bomb Reduction	Cell II	Cell II	Cell III	Cell III	Cell III	Cell IV	Cell IV	Cell IV	Cell IV	Cell IV	Cell IV
Pu Phase Deposited	-	-	-	δ'	[illegible]	δ'	N D [d]	N D [d]	δ'	[illegible]	[illegible]	[illegible]	[illegible]	[illegible]
Cell Current (Amperes)	-	-	-	0.3-4.0	1.5	0.3	0.3	0.3	1.9	0.1	1.6	0.2	2.2	2.3
Melt-down Salt	-	-	-	KCl-LiCl	KCl-LiCl	KCl-LiCl	KCl-LiCl	KCl-LiCl	KCl-NaCl	KCl-NaCl	KCl-NaCl	KCl-LiCl	KCl-NaCl [b]	KCl-NaCl
Deposited in Run No.	-	-	-	11 and 12	15	8, 9, 10 and 11	15	17	6	7	8	9	11	15
Element [c]	Composition in parts per million by weight													
H	3.5	6-9	N D [d]	14	12	7.3	7.4	8	5	7	6	6	16	5
C	21-36	46-130	N D [d]	28	27-42	47	54	31-52	25	62	44	33	43	20
N	42	10-44	67	15	13	12	14	<5	<5	<5	17	6	7	6
O	4-14	70-130	N D [d]	7	8	14	2	2	14	4	5	4	13	8
Si	10-15	45	35-51	10	6	8	19	11	- [f]	- [f]	- [f]	- [f]	- [f]	- [f]
U	81	90	N D [d]	30	15	25	15	85	- [f]	- [f]	- [f]	- [f]	- [f]	- [f]
Am^{241} [e]	266	200	100	0	0-5	0	0	2	~4	4	3	0	5	2
Al	25	100-200	180	10	15	10	8	8	<2	<2	<5	5	<2	<2
Ca	20	<5	20-30	2	3	2	2	2	<2	2	2	<2	2	2
Cr	1	150-250	250-500	2	5	8	8	10	1	10	2	8	4	1
Cu	10	5-20	35	2	1.5	4	1	4	N D [d]	N D [d]	N D [d]	N D [d]	N D [d]	N D [d]
Fe	10	100-150	1000	10	15	120	80	120	<4	<4	<4	17	<4	4
Ga	<2	N D	500	N D [d]	2	2	<2	<2	<0.2	1	3	15	2	<0.2
K	10	1-3	≤10	10	4	10	4	10	N D [d]	N D [d]	N D [d]	N D [d]	N D [d]	N D [d]
Li	<0.004	<0.01	0.02	0.1	<0.3	0.04	0.02	0.1	0.4	0.5	3	3	0.4	0.2
Mg	5	40-90	150-200	0.6	2	0.8	<0.8	<0.8	1	<1	<1	<1	<1	1
Mn	15	20-45	20-75	0.4	2	1	2	2	0.1	0.5	0.5	2	0.5	0.05
Mo	<30	N D [d]	5-100	400	60	80	60	60	0.5	<0.5	<0.5	0.5	0.5	<0.5
Na	<4	1-5	2	0.4	0.6	0.2	0.4	0.6	<2	<2	9	3	<2	<2
Ni	10	150-200	1000	<1	<0.6	1	0.4	<1	<1	5	3	30	10	1
Pb	<5	5-15	24-100	<4	2	<4	<4	<4	1	3	2	3	2	1
Zr	25	10-30	35	<0.4	<1.5	<0.4	<0.4	<0.4	<1	<1	<1	1	<1	1

a. Metal produced using high purity" anodes.
b. Deposit washed twice in KCl-LiCl at 450°C before meltdown.
c. Other elements analyzed and found to be below spectroscopic limits are B, Ba, Be, Bi, Cd, Co, Hf, La, Sc, Sn, Sr, Ti, V and Zn.
d. Not determined.
e. Grows in with time. Data are for electrolytic plutonium, corrected to date of electrolysis.
f. Analysis pending.

runs. Also given are the analyses for the anode materials, and for high-purity plutonium prepared by bomb-reduction techniques.

Americium, calcium, copper, magnesium, manganese, lead, and zirconium are all contaminants in the anodes which are reduced in the fused salt electrolysis. Their concentrations in the final buttons do not seem to vary from cell to cell. Some of these, viz., americium, calcium, magnesium, manganese, and zirconium, are reduced to very low levels. Potassium, lithium and sodium are usually present at concentrations close to the limits of the analyses; this indicates a small amount of entrapped salt in the buttons.

Aluminum, chromium, gallium, and nickel are all reduced to low levels, and their final concentrations seem to be affected by the impurity content of the anodes or by the run conditions. Both uranium and silicon are reduced by factors of about three and it is not yet known if further purification can be achieved by recycling the metal. It is possible that a lower limit for silicon is established by the use of Vycor in the cell and in the meltdown operations.

Hydrogen and carbon seem to be reduced only slightly in the electrolysis. Further reduction of hydrogen can be obtained by liquation (see below), and the use of "pure" anodes seems to aid in carbon reduction (see run M27, Table V). It is possible that carbon is added to the metal when the anodes are cast into graphite molds. This possibility will be investigated and the need for using other mold materials might then be examined.

Oxygen and nitrogen impurities have been found to be fairly low, especially in Cell IV material. The higher oxygen values for runs M9 and M12 are probably due to incomplete surface cleaning or delays in analysis, which allows surface oxidation to take place. This was shown to be the case for an oxygen sample from M16, prepared at the same time as the one reported in Table V, and which was stored in helium over a week end. The stored sample was found to have 57 ppm, while the matching sample, which was analyzed the same day it was cut, contained only 2 ppm oxygen. An effect in sample preparation on oxygen content has also been noted. The oxygen samples from M19, M23, and M27 were cleaned by polishing with SiC paper; those from M20, M21, and M22 were wiped with ethyl alcohol after the SiC polish. The consistently lower values for the latter samples show the need for further examination of sampling techniques.

The constancy of the molybdenum contents in the metals from cells II and III implies that 60 ppm might represent its lower limit for plutonium deposited on molybdenum cathodes from a mixed chloride-fluoride bath. In the plutonium deposited on tantalum (Cell IV), the molybdenum content was below the limits of spectroscopic detection. The only tantalum

analysis available to date is for M20, for which a concentration of less than 5 ppm has been tentatively reported. This value was obtained by examination of the gamma-ray spectrum of a solution of the electrolytic sample and of standard tantalum solutions prepared from small pieces of the irradiated cathodes. The determination of the lower limit of tantalum contamination might be improved by removal of the bulk of the plutonium from the sample solution, thereby causing a reduction of the background activity. The use of cathodes with a higher specific activity will also allow a more accurate determination of the tantalum content.

Iron contamination of the plutonium deposited on molybdenum cathodes was reduced by a factor of about ten. The use of tantalum cathodes and KCl-NaCl meltdown salt have reduced the iron contamination to below spectroscopic limits. The higher iron content of M22, which was melted in KCl-LiCl, may be due to a slightly higher iron content in the salt, i.e., 10 ppm iron in LiCl and 2 ppm iron in NaCl. There is the further possibility that the iron contamination from Cells II and III may be due to an iron impurity in the molybdenum.

Effects of Varying Operating Conditions in Cell IV: There appears to be no significant differences between material deposited at temperatures corresponding to the delta or delta-prime phases (M19 and M21). Material deposited under a low current density (M20) is slightly more contaminated than that deposited where using a higher current (M19) The effect of rinsing the deposit in KCl-LiCl before melting it in KCl-NaCl (M23 compared to M19) has been to increase the hydrogen, nitrogen, and perhaps the carbon contents of the button; it has not aided in the removal of any impurities. Metal melted in KCl-NaCl, dried by melting in dry helium, is lower in aluminum, iron, nickel, and gallium content than metal melted in specially dried KCl-LiCl.

At the end of the series of runs in Cell IV described here, two runs were made with anodes prepared from the "high purity" plutonium obtained in Cells II and III. The metal obtained in the second of these runs, M27, is the purest plutonium obtained to date. The final evaluation of the purity of this metal must await additional chemical analyses and microscopic examination.

Liquation of Plutonium Impurities: Several preliminary liquation runs have been made in MgO crucibles. No magnesium contamination of the metal has been observed. Melting of plutonium in vacuum has reduced the hydrogen content to 2 to 3 ppm. Vertical variation in the concentrations of aluminum, chromium, iron, and manganese indicate the possibility of further reductions of these elements by liquation. There has been no reduction or vertical variation of the carbon content.

Summary: The use of specially dried KCl-LiCl as the electrolyte solvent has reduced the break-in period for the cell but has not affected the purity of the deposited metal. Deposition onto tantalum cathodes from moderately pure plutonium anodes yields very pure metal when melted in KCl-NaCl. Of the remaining analyzed impurities, hydrogen is reduced further by melting in vacuum, and the oxygen and nitrogen contents are strongly dependent on sample preparation. The carbon content might be further lowered by the elimination of graphite as a mold material for anode castings, or by the use of a fresh electrolytic bath during the recycle electrolysis.

2. Uranium (G. B. O'Keeffe and L. T. Lloyd)

Preparation of high-purity uranium for use in research studies has continued during 1959. The loss of melts due to either failure of the thoria crucibles or to "burn-through" of the 2-in. diameter copper molds, which were the prime difficulties of the process discussed in the annual report for 1958 (ANL-5975), has been greatly diminished, and no melts have been lost since May 1959. A total of 51 melts were made during the year and 47 ingots were obtained, with a total weight of 117 kg. Several of these contained certain concentrations of impurities in excess of the acceptable average for "high purity" material. Disbursements were made in various quantities to the following organizations during 1959:

Atomics International
Chemistry Division - ANL
Chemical Engineering Division - ANL
French School of Mines (Paris)
General Electric Company (Hanford)
United Kingdom (Harwell)
Westinghouse Electric Corporation.

This operation will be discontinued during the coming year when we move into the Fuels Technology Center. Efforts will be diverted toward the preparation of high-purity plutonium.

B. Physical Metallurgy of Uranium

1. Plastic Deformation of Single Crystals at Elevated Temperatures (L. T. Lloyd)

Experimental work on the operative deformation mechanisms of alpha-uranium single crystals upon compressive loading at 600°C has been completed during the past year. Some of the results of this investigation were given in the 1958 Annual Report (ANL-5975). During the current year six additional crystals have been studied. The compression directions for these were selected with two aims in mind: (1) to verify the value of the critical resolved shear stress at 600°C for the (001)-[100] and {110} -<110> slip systems, and (2) to investigate the operative deformation mechanisms of crystals compressed in directions not lying near the principal crystallographic planes. The latter crystals served to complete a representative coverage of random crystallographic directions on a quadrant (001) standard projection plot.

Good checks were obtained on the critical resolved shear stress values that were reported for (001)-[100] slip (0.013 kg/mm^2 and {110} -<110> slip (0.43 kg/mm^2) in the 1958 report. These served to establish firmly the predominance of the former slip system in compressive deformation at 600°C.

As might be expected, the crystals compressed in directions away from the principal crystallographic planes exhibited multiple slip deformation mechanisms. In addition to the more important deformation of (001)-[100], (010)-[100], and {110} -<110> slip, the crystals yielded evidence for slip on the {111} and {021} planes.

Slip on the {111} plane was always accompanied by other deformations, which made it impossible to determine experimentally its slip direction. From considerations of the most densely packed direction in {111} planes, the <110> and <112> directions are the most likely slip directions. At 600°C, the atoms are spaced 3.263 Å apart in the <110> directions, and only 3.006 Å in the <112> directions, but for the latter case they must shift 0.734 Å perpendicular to the direction.

2. Recrystallization Textures in Deformed Single Crystals (L. T. Lloyd)

Publication:

1. L. T. Lloyd, "Recrystallization of Deformed Alpha-Uranium Single Crystals," ANL-6001 (July 1959).

The above report describes the results of a study of the crystallographic orientation relationships between deformed alpha-uranium single crystals and grains grown in them by annealing within the alpha-phase temperature range. Crystals, which had been deformed at room

temperature in compression and whose elements of deformation had been previously determined, were annealed for various periods of time at different temperatures and observed metallographically for evidence of recrystallization. Orientation determinations of the recrystallized grains and of the remaining deformed portions of the crystals were obtained from Laue back-reflection photograms. Stereographic treatment of the data yielded an orientation relationship between deformed and recrystallized material which can be expressed as 27.5° rotations about the four crystallographically equivalent axes located 70.0° from the [100] direction, 63.5° from the [010] direction, and 34.0° from the [001] direction. Rotations for the axes located in the first and third quadrants of a (001) standard projection were in clockwise direction, and for axes located in the second and fourth quadrants, counterclockwise. In arriving at these relationships, the recrystallized grains were considered to originate from deformed twin orientations, as well as from the original crystal orientation. The twin orientations that were required to explain the observed recrystallized grain orientations in a particular crystal corresponded with the operative twin systems of these crystals. These recrystallization orientation relationships differ from similar observations in face-centered cubic, body-centered cubic, and hexagonal metals in that the axes of rotation are not normal to the most densely populated planes of the crystal structure. Comparison of observed recrystallization textures in polycrystalline alpha-uranium rod and sheet materials with those derived from the observed deformation textures and the orientation relationship described above showed good agreement.

3. Recrystallization of Room-temperature-rolled Sheet (L. T. Lloyd and M. H. Mueller)

Publication.

1. W. R. Yario and L. T. Lloyd, 'Recrystallization of Heavily Cold-rolled Uranium Sheet,' ANL-5966 (May 1959).

The above report summarizes the work that has been completed on the recrystallization studies of high-purity uranium sheet rolled to 80% reduction in thickness at room temperature As discussed in the report, because of the large alpha grain size present prior to the final fabrication and the resulting heterogeneous deformation, it was impossible to obtain quantitative measurements of preferred orientation by X-ray diffraction techniques from the above work To overcome this difficulty and to permit correlation of microstructural observations, thermal expansion behavior, and X-ray preferred orientation measurements, the studies have been continued on high-purity material prepared in a manner such that the starting grains were uniform and reasonably small in size, and the deformations on rolling were more homogeneous. The results to date on this type material are as follows.

Some of the metallographic studies have been completed. Similar to the previous work on the heterogeneous material, the initial stages of recrystallization were characterized by the creation of very fine grains which were absorbed later by discontinuous growth of larger grains. An interesting observation in the present work is that an increased annealing temperature is required to give, for equal annealing times, a comparable percent recrystallization to that found for the heterogeneous material.

The thermal expansion studies are nearly complete. In general, the results agree well with those from the previous work. Mean thermal expansion coefficients in a direction lying in the plane of the sheet and perpendicular to the rolling direction (transverse samples), after almost complete recrystallization at low temperatures, were not significantly different from those obtained on as-rolled material annealing at higher temperatures to comparable percentages of recrystallization resulted in a measurable change in this property. Mean expansion coefficients in directions parallel to the rolling direction (longitudinal), however, showed a somewhat different behavior. In the earlier results with heterogeneous material, the data obtained for the longitudinal directions were quite erratic because they did not represent adequate statistical sampling of the grain orientations parallel to the rolling direction. In the present work, the sampling was adequate and the mean expansion coefficients in the longitudinal direction showed a consistent decrease as the percent recrystallization increased, regardless of the annealing temperatures. Sufficient metallographic measurements are not yet available to correlate positively the changes for this direction with percent recrystallization at the various annealing temperatures These results suggest that the preferred orientation of samples annealed at the lower temperatures of the recrystallization range is different from that of as-rolled material; however, a second preferred orientation may be obtained upon annealing at intermediate temperatures. X-ray diffraction determinations of preferred orientation should clarify these points.

Sets of samples have been prepared for measurements of preferred orientation of five material conditions. (1) as rolled, (2) annealed 300 hours at 380°C, (3) annealed 15 hours at 400°C, (4) annealed 15 hours at 450°C, and (5) annealed 300 hours at 380°C, followed by reannealing 15 hours at 450°C. X-ray diffraction intensity measurements for the construction of pole figures have been obtained from the first three sets of samples. It is planned to obtain four pole figures for each set of samples, namely, the (010), (110), (001), and (100) Pole figures of the as-rolled material have indicated no significant change in preferred orientation from that reported previously[5] for reactor-grade material rolled 87% reduction in thickness at 300°C. The preferred orientation in the 380°C annealed specimens appeared to be practically identical with the 400°C annealed specimens, as was suspected from thermal expansion measurements, but it was clearly different from the as-rolled condition. This is in agreement with the dilatometric

[5]M. H. Mueller, H. W. Knott and P A. Beck, Deformation and Recrystallization Texture of Rolled Uranium Sheet Trans AIME 203 1214 (1955).

results discussed above. The pole figures from these first two annealed sets of specimens appeared to be quite different from those previously reported[5] for samples annealed at higher temperatures A more complete discussion of the preferred orientations will be possible when the pole figures are available for the other two sets of specimens

4. Some Aspects of the Beta-to-Alpha Phase Transformation

Publication

1. H. H. Chiswik and L. T Lloyd, "Some Aspects of the Beta to Alpha Transformation in Uranium Metallographic Structure and Orientation Relationships," ANL-5777 (November 1959)

The effects of cooling rates and temperature gradients during the beta-to-alpha phase transformation in uranium on the microstructure and on the crystallographic orientations of the resultant alpha grains are discussed. The quantity of substructure, or "subgrains," resulting from the volume change upon allotropic transformation decreased as the cooling rate through the transformation temperature was decreased. The tendency for subgraining in samples cooled through the transformation temperature at a rate of 0.5°C per hour, with no temperature gradient imposed on the sample, was greatly reduced but not completely eliminated. Cooling through the phase transformation temperature at the above rate, but with temperature gradients imposed on the sample resulted in a higher degree of subgraining which increased with the magnitude of the imposed temperature gradient.

Holding the cooling rate through the phase transformation constant at 0.5°C per hour, and increasing the magnitude of the temperature gradient along the sample up to 138°C per inch, resulted in an increase in the size of the primary alpha grains For the higher temperature gradients, the grains were elongated in the direction of the temperature gradient.

The crystallographic orientation studies indicate that an increase in the imposed temperature gradient during phase transformation at a constant cooling rate of 0.5°C per hour causes a greater concentration of (001) plane poles in the direction of the temperature gradient. This implies that entirely random textures may not be expected in uranium samples subjected to heat treatments involving the beta-to-alpha phase transformation under conditions of imposed temperature gradients

C. Uranium and Plutonium Alloys: Constitution and Properties

1. Uranium-Carbon (B. Blumenthal)

Publications:

1. B. Blumenthal, "Constitution of Low Carbon U-C Alloys," ANL-5958 (May 1959).

Work on the constitution of the uranium end of the uranium-carbon system was completed during 1959 and the above report describes the results in detail. A summary of the data follows.

Figure 14
Uranium-Carbon Phase Diagram at Low Carbon Concentrations

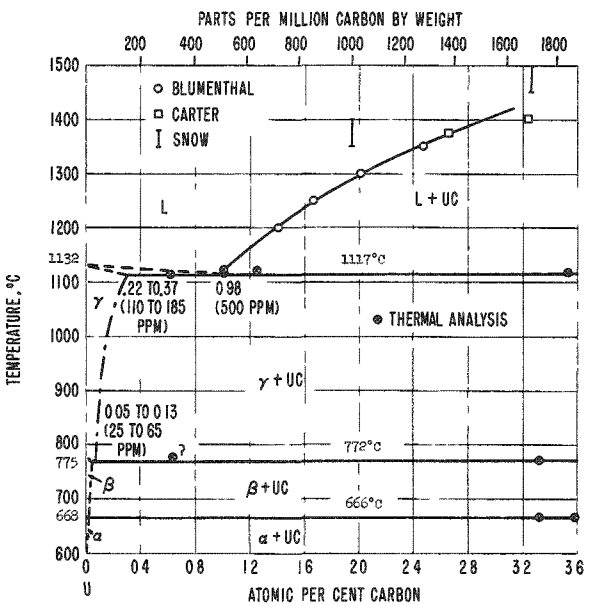

The low-carbon portion of the phase diagram, as determined by saturation experiments, thermal analyses, and metallography, is shown in Figure 14. The system has an eutectic at 0.98 a/o carbon at a temperature of 1117°C. Solubility of carbon in gamma uranium decreases from about 0.30 a/o at the eutectic temperature to about 0.09 a/o at the γ U $\rightleftharpoons$ β U + UC eutectoid temperature of 772°C. The solid state reaction occurring at 666°C is also of the eutectoid type: β U $\rightleftharpoons$ α U + UC. Solid solubility of carbon in the beta phase is estimated to be less than 10 ppm and, in the alpha phase, less than 3 ppm.

Decarburization was observed to occur in samples annealed at temperatures in the gamma-phase range. It is believed to be caused by the formation of a UN phase on the surface of the uranium sample by reaction with residual nitrogen in the inert gas annealing atmosphere, and subsequent depletion in carbon of the sample interior by diffusion to the surface to form a U(C,N) phase.

2. Uranium-Niobium-Zirconium (A. E. Dwight)

Work on the uranium-niobium-zirconium system has consisted principally of an investigation of the miscibility gap originating in the niobium-zirconium binary system and the extent of the γ + Zr field at

temperatures below 500°C. The results indicate that the γ + Zr field is somewhat larger and the gamma field somewhat smaller than was originally believed.

3. Uranium-Fissium (A. E. Dwight, S. T. Zegler and M. V. Nevitt)

Publications:

1. M. V. Nevitt and S. T. Zegler, "Transformation Temperatures and Structures in Uranium-Fissium Alloys," J. of Nuc. Materials 1(1) 6-12 (April 1959).

2. S. T. Zegler and M. V. Nevitt, "Some Properties of Uranium-Fissium Alloys," Nuc. Sci. and Engr. 6(3) 222-228 (September 1959).

Phase Diagrams with Fissium Elements: Work on the uranium-molybdenum system below 900°C has been completed. The equilibrium diagram in its final form closely resembles that shown in the 1958 annual report. The major differences between our work and that of earlier investigators is that we find the delta phase to be formed congruently from the gamma, rather than by a peritectoid transformation, and that the eutectoid reaction $\beta \longrightarrow \alpha + \gamma$ is at a lower temperature - 639 ± 5°C. The results are described in detail in a forthcoming publication.

A metallographic examination of the uranium-hafnium system was made on specimens quenched from between 500 and 900°C. The equilibrium diagram resulting from this investigation is shown in Figure 15 and is in close agreement with a diagram published by Peterson and Beernsten.[6]

It was found that neither the β nor the γ phase can be retained on quenching from below 900°C. A banded martensitic structure, similar to those found in uranium-niobium, uranium-molybdenum, uranium-titanium and other alloys, was found in 4 w/o Hf alloy quenched from the γ range. When isothermally transformed, the γ forms a non-lamellar eutectoid of β-U + α-Hf, in contrast to the lamellar structures found in the uranium-molybdenum and uranium-niobium systems.

Work is continuing on the uranium-ruthenium, uranium-rhodium, and uranium-ruthenium-molybdenum systems, with major emphases on the composition limits and lattice parameters of the γ phase fields.

---

[6]D. T. Peterson and D. J. Beernsten, The Uranium-Hafnium Equilibrium System, ASM Preprint No. 158 (1959).

Figure 15

Uranium-Hafnium Equilibrium Diagram

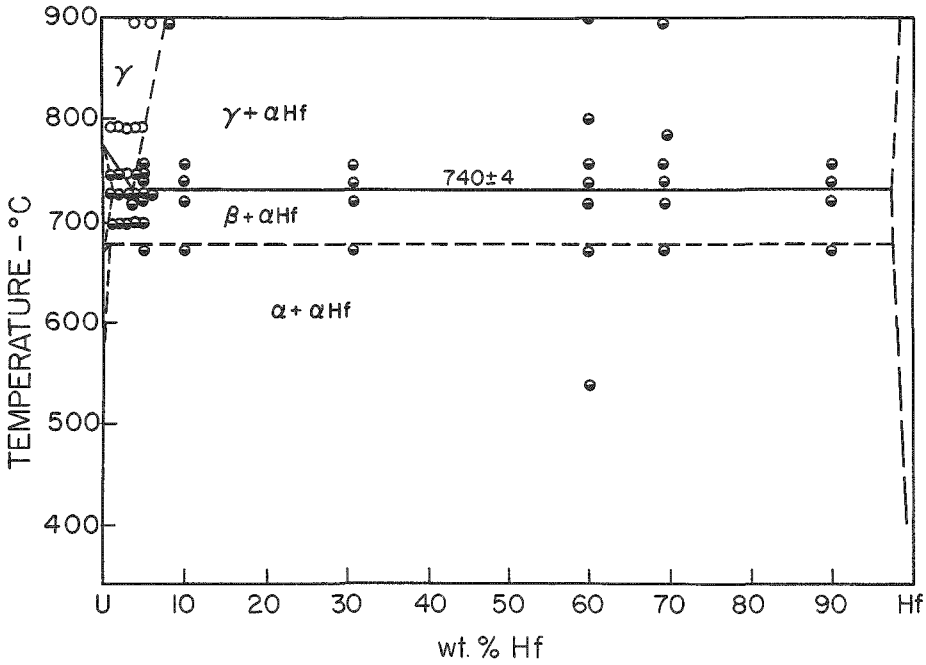

Micro 26412

Properties: Solid-state phase transformations, and hardness, density, and thermal expansion data for uranium-fissium alloys are described in detail in the two publications listed above. Phase relations were found to resemble those in the dominant uranium-molybdenum-ruthenium ternary system, while the room temperature properties of the alloys were shown to be influenced primarily by the presence of the metastable uranium gamma phase.

The design, construction, and calibration of an apparatus for measuring the thermal conductivity of these alloys in the range from 40 to 700°C have now been completed. The apparatus yields measurements with a precision of ±4% or better. Measurements of thermal conductivity as a function of temperature have been made with this apparatus for as-cast uranium and uranium-fissium alloys containing 3, 8, and 10 w/o fissium. The materials were vacuum melted by induction heating in thoria-coated graphite crucibles and bottom poured into water-cooled copper molds. The conductivities of uranium and the three uranium alloys are shown in Figure 16. All these materials show an increase in conductivity with increasing temperature. The conductivity decreases with increasing fissium concentration.

Figure 16

Thermal Conductivity Versus Temperature for Uranium and three Uranium-Fissium Alloys

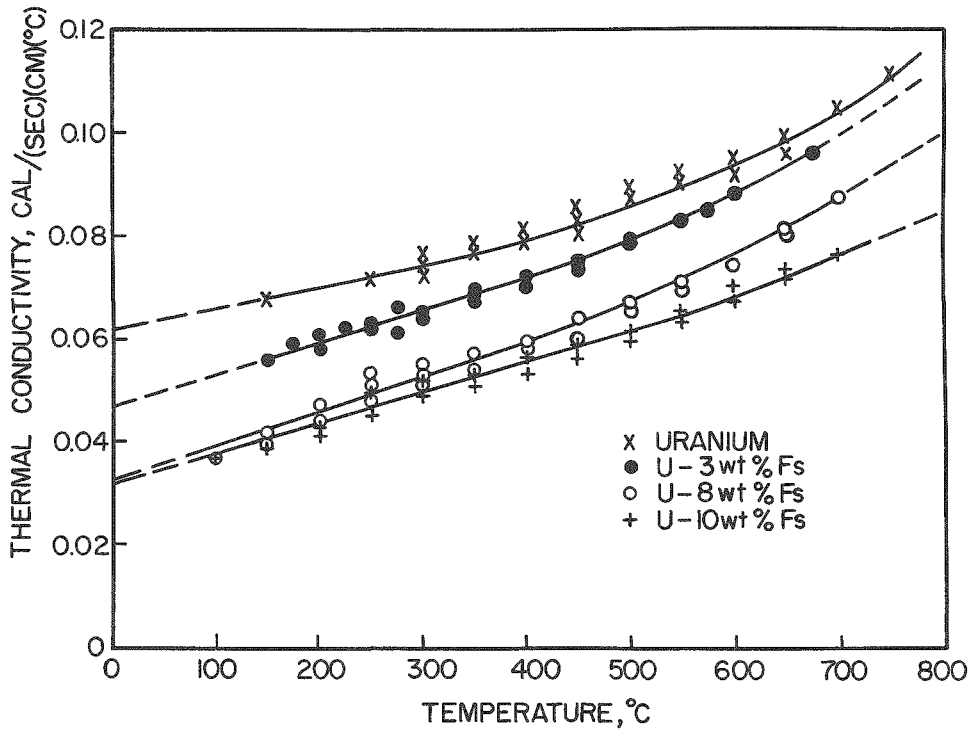

Micro 26626

4. Phase Diagrams of Plutonium with Fissium Elements (E. M. Benson and M. V. Nevitt)

Plutonium-Zirconium: Certain discrepancies in the published versions of the high zirconium end of the phase diagram are being investigated by X-ray diffraction and metallographic techniques. As the first step we are working to establish whether the delta plutonium phase forms by the eutectoidal decomposition of β zirconium at 620°C,[7] or forms peritectoidally from epsilon plutonium and alpha zirconium at 630°C.[8] The work has thus far been limited to an X-ray study of the 50, 60, and 70 a/o zirconium

[7] M. B. Waldron, J. Garstone, J. A. Lee, P. G. Mardon, J. A. C. Marples, D. M. Poole, and G. K. Williamson, "The Physical Metallurgy of Plutonium," Proceedings of the Second United Nations International Conference on the Peaceful Uses of Atomic Energy, Vol. 6, Basic Metallurgy and Fabrication of Fuels, 162-169 (1958).

[8] A. A. Bochvar, S. T. Konobeevsky, V. I. Kutaitsev, I. S. Menshikova, and N. T. Chebotarev, "Interaction of Plutonium and Other Metals in Connection with Their Arrangement in Mendeleev's Periodic Table," Proceedings of the Second United Nations International Conference on the Peaceful Uses of Atomic Energy, Vol. 6, Basic Metallurgy and Fabrication of Fuels, 184-193 (1958).

alloys quenched from 620, 639, and 660°C. It is hoped that a limited number of heat treatments in these temperature and composition ranges will be sufficient to test the validity of the constructions in the two diagrams. Results are as yet inconclusive since the epsilon plutonium (β zirconium) phase which according to both diagrams should exist in the alloys quenched from 639 and 660°C, has not been identified in any of the diffraction patterns. At this point it appears that this may be due to too low a quenching rate of the needle-shaped X-ray specimens. Further work is in progress to resolve this problem.

Plutonium-Ruthenium: Five compounds of the binary plutonium-ruthenium system, $PuRu_2$, PuRu, Pu_5Ru_3, Pu_3Ru and $Pu_{19}Ru$, have been prepared and investigated. X-ray diffraction studies of the $PuRu_2$ compound confirm the existence of the Cu_2Mg-type structure as reported.[9] The lattice parameter, $a_0 = 7.474 \pm 0.001$Å, is in good agreement with the published value. Comparison of $PuRu_2$ with Laves phases in other systems (see section on Alloying Properties) shows that the contractions of the ruthenium and the plutonium atoms are consistent with those shown by these two atomic species in other Laves phases. Diffraction studies of PuRu also confirm the CsCl structure type that has been reported.

D. Alloying Properties

1. Studies on Transition Metal Intermediate Phases
(A. E. Dwight and M. V. Nevitt)

Publication:

1. A. E. Dwight and P. A. Beck, "Close-Packed Ordered Structures in Binary AB_3 Alloys of Transition Elements," AIME Trans. 215 976-979 (December 1959).

The general objective of this program has remained unchanged since the last Annual Report, namely, the study of the roles and interrelations of atomic size, valency effects, and stacking geometry in the occurrence of intermediate phases in transition metal systems. In addition to the compound types discussed in the last Annual Report, a group of intermediate phases having the AB_5 formula and a group isostructural with α-manganese have been examined. The Hf-Co binary diagram and the ternary diagrams of Zr-Co-O and Zr-Ni-O have also received attention. Details of these studies are discussed below.

---

[9] F. W. Schonfeld, E. M. Cramer, W. N. Miner, F. H. Ellinger, and A. S. Coffinberry, "Plutonium Constitutional Diagrams," Prog. in Nuc. Energy, Serices V, Vol. 2, Metallurgy and Fuels, 579-599, Pergamon Press, London (1959).

Laves-type Phases: In the Annual Report for 1958 (ANL-5975) it was stated that Laves-type phases were found in 13 binary systems out of 28 which were investigated. As a continuation of this search, 18 additional Laves-type phases were discovered out of an additional 45 systems investigated during 1959. The 18 Laves-type phases are listed in Table VI.

TABLE VI

Laves Phases Studied during 1959

AB_2	Type	c, Å	a, Å	c/a	D_A-d_A, Å	D_B-d_B, Å
$ScFe_2$	C36	16.278	4.972	3.274	+0.2295	+0.098
$ScCo_2$	C15		6.921		+0.2852	+0.06
$ScRu_2$	C14	8.53	5.14	1.66	+0.0833	+0.0501
$ScIr_2$	C15		7.346		+0.1012	+0.1135
YNi_2	C15		7.184		+0.4913	-0.0521
YRh_2	C15		7.489		+0.3593	+0.0379
YPt_2	C15		7.607		+0.3082	+0.0821
$LaRu_2$	C15		7.701		+0.4155	-0.077
$LaOs_2$	C15		7.736		+0.4003	-0.065
$LaRh_2$	C15		7.647		+0.4389	-0.018
$LaIr_2$	C15		7.688		+0.421	-0.0075
$LaPt_2$	C15		7.755		+0.3921	+0.0297
$CePt_2$	C15		7.723		+0.306	+0.041
$GdPt_2$	C15		7.577		+0.3232	+0.0928
$ErFe_2$	C15		7.274		+0.3644	+0.009
$ErRu_2$	C14	8.790	5.235	1.679	+0.2177	-0.018
$HfAl_2$	C14	8.673	5.241	1.655	-0.0554	+0.2181
$ThRu_2$	C15		7.649		+0.2836	-0.058

The lattice contractions (for definition see ANL-5975) of the Laves-type phases that have been studied during the past two years are plotted against the radius ratios in Figures 17 and 18. When the data points are designated with respect to the identity of the B-element they can be fitted fairly well to 3 curves, each of which represents a group of B-elements. It can be seen that the contractions of both the A- and B-partner are smaller where B is ruthenium, rhenium or osmium, than when B is rhodium, iridium or platinum. When the same data points are labeled with respect to the identity of the A-element (not shown here), one can conclude that A- and B-element contractions are smaller when A is a titanium group element or an actinide element than when it is scandium, yttrium or one of the lanthanides. A combination of both of these factors accounts for the low contractions observed in such phases as $ThRe_2$.

Figure 17

Contraction of the A-Element in AB_2 Laves Phases

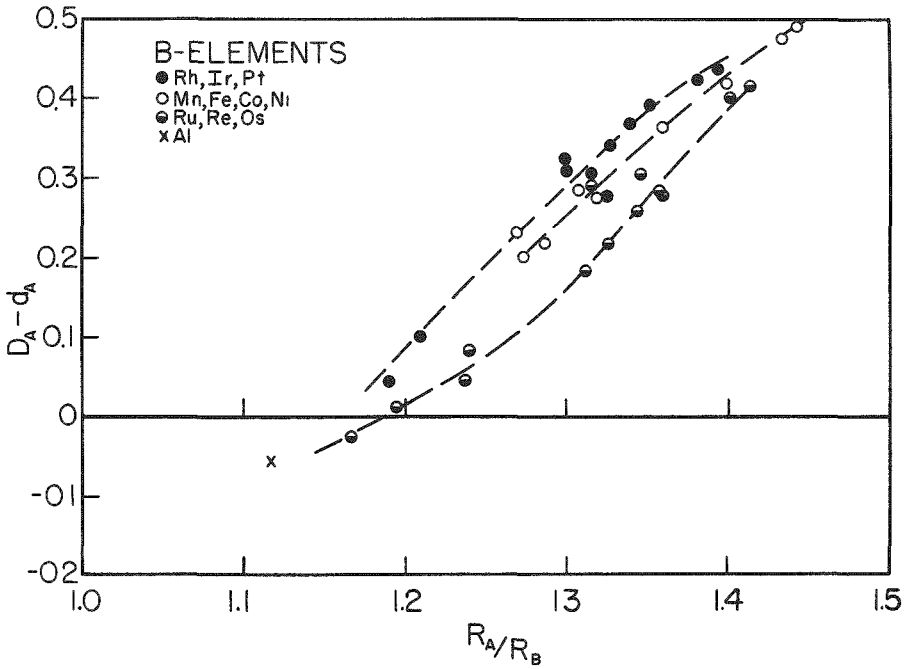

Micro 26621

Figure 18

Contraction of the B-Element in AB_2 Laves Phases

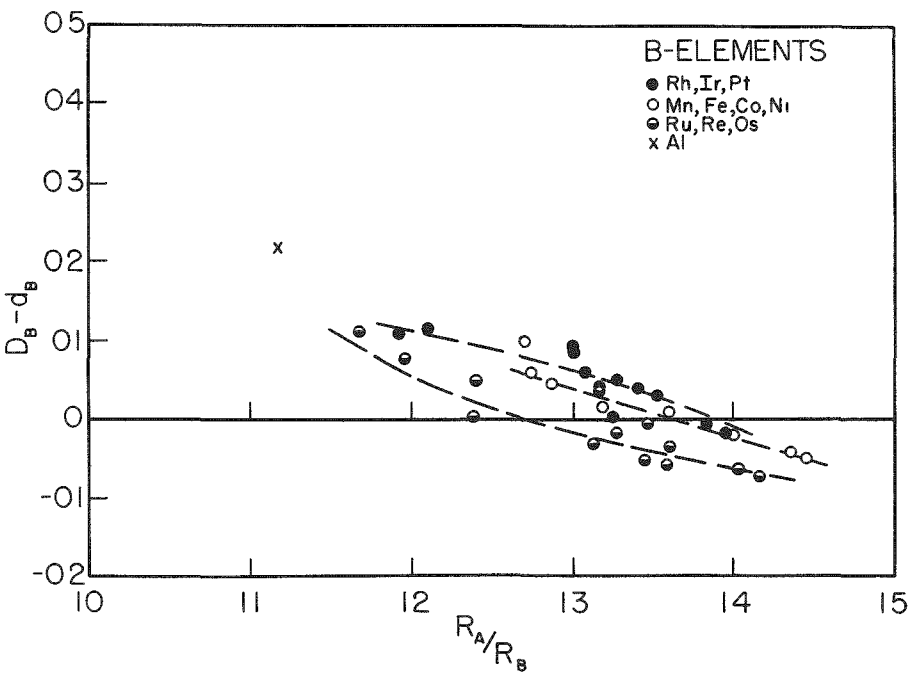

Micro 26620

The newly reported Laves-type phases raise the known total number to 161. An analysis of data pertaining to all known Laves-type phases leads to the following additional conclusions:

1. The ratio of the Goldschmidt radii of the component elements in the pure state can range from 1.05 to 1.68, and thus the Goldschmidt radius ratio is a poor criterion of whether a Laves-type phase is likely to occur in an unknown system. It is necessary that the A-element be larger than B.

2. Cubic (C15) Laves-type phases exist with radius ratios from 1.05 to 1.68, but hexagonal (C14, C36) phases exist over a somewhat narrower band of 1.06 to 1.40.

3. The position of the partner elements in the periodic table is a controlling factor in determining which of the three Laves-type phases will be formed. Rhodium and iridium form only cubic phases; rhenium forms only hexagonal phases. These are examples of a trend in which B-elements of the manganese and iron groups favor hexagonal Laves-type phases and B-elements of the nickel and cobalt groups favor cubic phases. The exceptions to this trend are most numerous among the B-elements of the first long period.

4. The B-elements rhodium and palladium are much more reluctant to form Laves-type phases than the other elements of their respective groups: cobalt, nickel, iridium, platinum. In particular, palladium will participate only with the extremely electropositive A-elements of the calcium group. A tentative explanation is that palladium is less able than platinum to undergo the necessary contraction, and therefore can form Laves-type phases only with A-elements which are sufficiently large and open in structure (small ionic core).

5. It is noted that thorium behaves more like the titanium group elements than like the scandium group.

<u>AB_3 Compounds:</u> The search for ordered phases of AB_3 composition was broadened to include elements of the scandium group and uranium as A-elements, and aluminum as a B-element. Ten additional AB_3 phases are listed in Table VII with their lattice parameters. The lattice contraction values listed in Table VII are computed by D_{AB}-d_{AB}, where D_{AB} is the average of the two Goldschmidt diameters, and d_{AB} is the minimum distance between an A and B atom in the alloy, as calculated from the lattice constants.

Figure 19 is a plot of lattice contraction vs the ratio of the Goldschmidt radii. It is noted that AB contraction is greatest when the A-element is of the scandium group, and that contraction decreases as the

TABLE VII

AB_3 Phases Studied during 1959

Composition	Structure Type	c_0, Å	a_0, Å	c/a	D_{AB}-d_{AB}, Å
$ThPd_3$	$TiNi_3$, DO_{24}	9.826	5.856	1.678	+0.245
VPd_3	$TiAl_3$, DO_{22}	7.753	3.847	2.015	+0.0143
VPt_3	$TiAl_3$, DO_{22}	7.824	3.861	2.027	+0.0164
$HfAl_3$	$ZrAl_3$, DO_{23}	17.155	3.989	4.301	+0.151
$ScPd_3$	Cu_3Au, Ll_2		3.981		+0.2007
$ScPt_3$	Cu_3Au, Ll_2		3.958		+0.229
YPt_3	Cu_3Au, Ll_2		4.075		+0.3061
$ThRh_3$	Cu_3Au, Ll_2		4.139		+0.2158
URh_3	Cu_3Au, Ll_2		3.991		+0.0525
UIr_3	Cu_3Au, Ll_2		4.023		+0.0419

Figure 19
Contraction in AB_3 Compounds

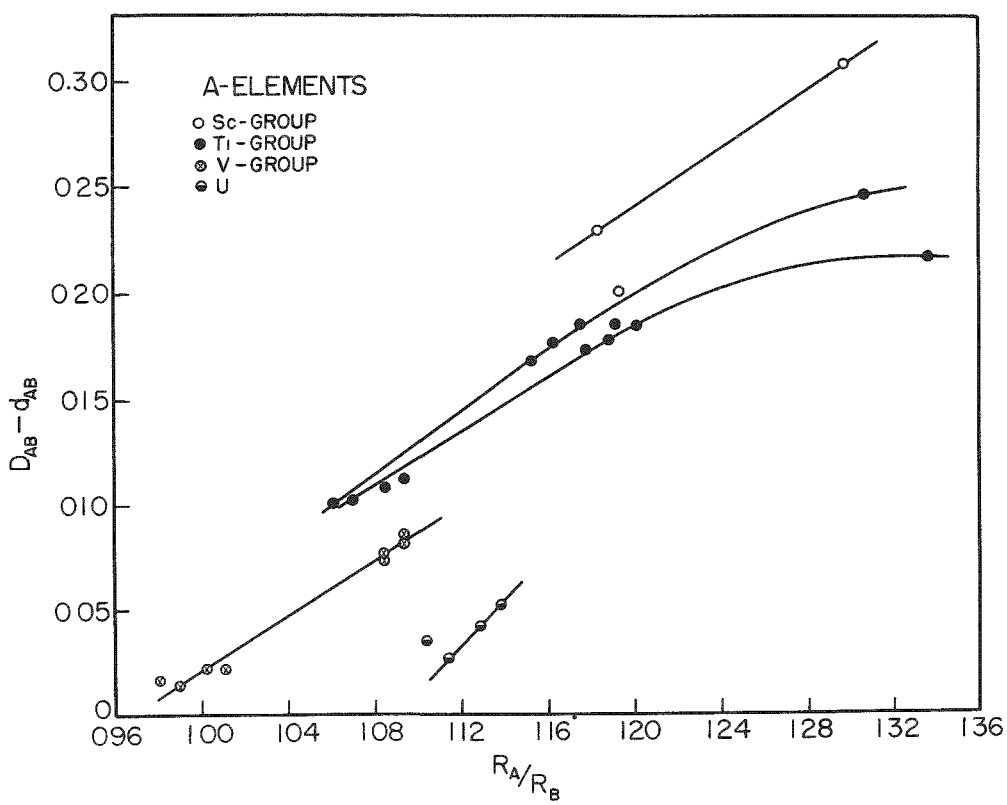

Micro 26614

A-element varies as follows: Sc group → Ti group (includes Th) → V group. The data points for alloys in which the A-element is uranium lie well below those for the vanadium group alloys, as if uranium were functioning as a member of the chromium group. It should be noted that Haworth and Hume-Rothery[10] have also included uranium in the chromium group. The data points for alloys in which A is titanium, zirconium, hafnium or thorium can be fitted to two curves, which are peculiar both to a grouping of B-elements and to a specific crystal structure; that is, the lower of the two curves represents the B-elements rhodium and iridium, and the crystal structure is of the Cu_3Au type. The upper curve represents the B-elements palladium and platinum and the crystal structure if of the $TiNi_3$ type.

If the curves on Figure 19 are extrapolated back to $R_A/R_B = 1.0$ a contraction is implied for Sc-, Ti-, and V-group alloys. This observation indicates that the stability of these AB_3 compounds does not result entirely from optimal space filling by spherical atoms, since A and B atoms having the same radius could be accommodated without a contraction.

The study of AB_3 compounds leads to the conclusion that, with respect to the structure type, thorium and uranium behave as members of the titanium group, although the accepted form of the periodic table lists thorium and uranium as actinide elements, with the zero element, actinium, included in the scandium group. The sequences of compounds having the same crystal structure are the basis for the above conclusion. These are listed in Table VIII.

TABLE VIII

Isostructural Phases of the Platinum Metals

B-Element	A-Element				
	Ti	Zr	Hf	Th	U
Rh	Cu_3Au	Cu_3Au	Cu_3Au	Cu_3Au	Cu_3Au
Ir	Cu_3Au	Cu_3Au	Cu_3Au	-	Cu_3Au
Pd	$TiNi_3$	$TiNi_3$	$TiNi_3$	$TiNi_3$	$TiNi_3$
Pt	Cu_3Au	$TiNi_3$	$TiNi_3$	*	$MgCd_3$

*The compound $ThPt_3$ has been isolated metallographically but its crystal structure has not yet been determined.

---

[10] C. W. Haworth and W. Hume-Rothery, A Note on Transition Metal Alloys, Phil. Mag. 3 (33) 1013-1019 (1958).

It was also noted in an earlier section of this report, that on Laves-type phases, that thorium behaves more like the titanium group elements than like the scandium group. The idea that thorium is a member of the titanium group is not inconsistent with the "thoride" hypothesis advanced by Zachariasen[11] and reviewed recently by Makarov.[12] According to this hypothesis, thorium is the zero element of the "thoride" series, rather than actinium being the zero element of an actinide series.

It was first shown by Laves and Wallbaum[13] that an ordered AB_3 compound, $TiNi_3$, could be explained by ABAC stacking of ordered layers. Since then other stacking schemes have been discovered, until at present 7 families of AB_3 compounds can be explained in terms of layer stacking. Three classes of ordered layers are known, and are shown in Figures 20, 21 and 22. The stacking schemes and class of layer for the seven known families are shown in Table IX. The complexities of certain

Figure 20
Ordered Layer, Class I

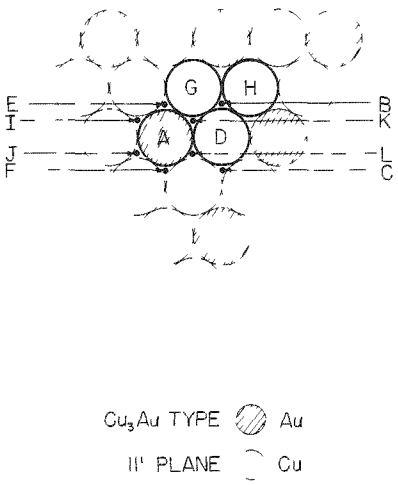

Micro 26616

Figure 21
Ordered Layer, Class II

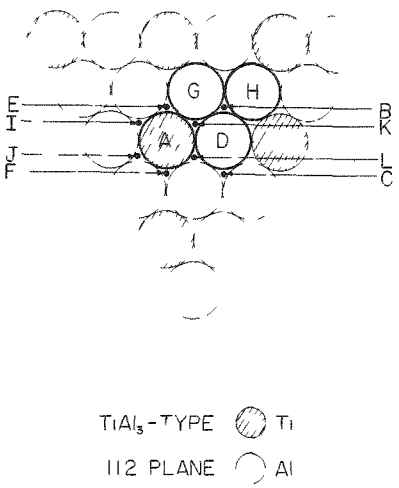

Micro 26615

Figure 22
Ordered Layer, Class III

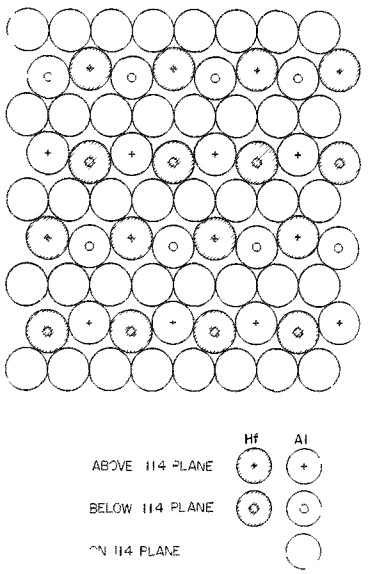

Micro 26618

---

[11] W. H. Zachariasen, "Crystal Chemistry of the 5f Elements," in The Actinide Elements by G. T. Seaborg and J. J. Katz, McGraw-Hill Book Co., New York (1954).

[12] E. S. Makarov, Crystal Chemistry of Simple Compounds of Uranium, Thorium, Plutonium, Neptunium, 45, 120, published by Consultant Bureau, Inc., New York, N.Y. (1959).

[13] F. Laves and H. J. Wallbaum, Die Kristallstruktur von Ni_3Ti und Si_2Ti, Zeit. Kristallographie, 101 78-92 (1939).

TABLE IX

Classification of AB_3 Ordered Layer Structures

Class of Layer	Stacking Sequence	Family	Symmetry
I	ABAB	$MgCd_3$	Hexagonal
I	ABCABC	Cu_3Au	f.c. cubic
I	ABCACB	$PuAl_3$	Hexagonal
I	ABAC	$TiNi_3$	Hexagonal
II	ABAB	$TiCu_3$	Orthorhombic
II	ACEDFB*	$TiAl_3$	Tetragonal
III	ACEDFB	$ZrAl_3$	Tetragonal

* The stacking sequence of the $TiAl_3$ family was reported by Saito and Beck,[14] but using a different nomenclature.

stacking schemes (e.g., ACEDFB for the $TiAl_3$ family) makes it necessary to adopt a standard nomenclature for designating the various lattice sites. Referring to Figure 21, a titanium atom in the ordered layer is designated as the A site. When a second layer is placed on the first, the titanium atom of the second layer lies in the interstice of the first layer designated as site C. The titanium atom of the third layer lies above the interstice of the first layer designated as site E, and so on until six layers have been stacked. The seventh layer has the titanium atom lying directly over the titanium atom of the first layer; thus first and seventh layers are equivalent and the stacking sequence repeats. A similar stacking of Class I layers in an ABC sequence leads to the face-centered cubic Cu_3Au structure.

As there are at least five more families of AB_3 compounds which have not yet been related to stacking of ordered layers, further work to locate other AB_3 compounds and to determine their crystal structures is planned.

AB_5 Compounds: Two families of AB_5 compounds are being investigated: the face-centered cubic UNi_5 type and the hexagonal $CaCu_5$ type. There is a close relation between these AB_5 compounds and the $MgCu_2$-type and $MgZn_2$-type Laves phases. Replacement of A atoms with B atoms on 4 lattice sites of the $MgCu_2$-type Laves phase creates the structure of the UNi_5 type. In a similar manner, replacement of A atoms with B atoms on 3 lattice sites on each of the (001) and (002) planes of the $MgZn_2$-type Laves phases creates the structure of the $CaCu_5$ type. It is to be expected that Laves AB_2 phases and AB_5 compounds would occur in many of the same systems, and this has been found to be the case. The AB_5 compounds of the $CaCu_5$ type which have been studied during the past year are tabulated in

[14] S. Saito and P. A. Beck, The Crystal Structure of $MoNi_3$, Trans. AIME 215 935 (1950).

Table X. No new examples of the UNi_5 type were found. A plot of the B atom contraction, D_B-d_B, vs R_A/R_B is shown in Figure 23.

TABLE X

Structural Details of $CaCu_5$-Type Compounds

AB_5	c, Å	a, Å	c/a	D_B-d_B, Å	R_A/R_B	AB_5	c, Å	a, Å	c/a	D_B-d_B, Å	R_A/R_B
YCo_5	3.969	4.956	0.801	0.0635	1.435	$PrCu_5$	4.109	5.122	0.802	0.0248	1.430
YNi_5	3.961	4.891	0.810	0.0576	1.446	$PrPt_5$	4.386	5.353	0.819	0.0914	1.318
YCu_5	4.113	4.994	0.824	0.0447	1.409	$NdCo_5$	3.977	5.031	0.791	0.0477	1.451
YPt_5			0.839			$NdNi_5$	3.976	4.956	0.802	0.0408	1.463
$LaCo_5$	3.976	5.108	0.778	0.0349	1.494	$NdCu_5$	4.107	5.110	0.804	0.0276	1.425
$LaNi_5$	3.982	5.016	0.794	0.028	1.506	$NdPt_5$	4.391	5.345	0.822	0.0906	1.313
$LaCu_5$	4.112	5.184	0.793	0.0129	1.467	$GdCo_5$	3.967	4.984	0.796	0.0597	1.436
$LaPt_5$	4.376	5.386	0.812	0.0898	1.352	$GdCu_5$	present				
$CeCo_5$	4.016	4.903	0.819	0.0533	1.454	$ErCo_5$	present				
$CeNi_5$	4.003	4.887	0.819	0.0413	1.466	$ErNi_5$	3.964	4.859	0.816	0.0619	1.411
$CeCu_5$	4.108	5.146	0.798	0.021	1.428	$HoCu_5$	present				
$CePt_5$	4.385	5.369	0.817	0.0892	1.316	$ThCo_5$	3.987	5.005	0.797	0.048	1.433
$PrCo_5$	3.988	5.027	0.793	0.0439	1.456	$ThIr_5$	4.288	5.315	0.807	0.0776	1.325
$PrNi_5$	3.975	4.964	0.801	0.0398	1.468						

Figure 23
Contraction of the B-Element in $CaCu_5$-Type AB_5 Compounds

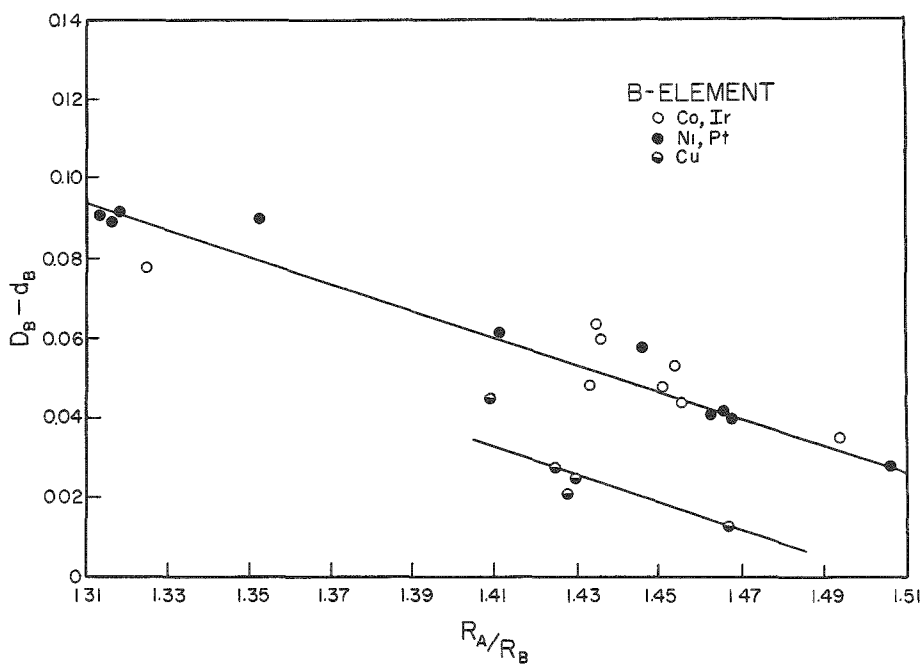

Micro 26653

Here d_B is defined as equal to $\sqrt{\frac{c^2}{4} + \frac{a^2}{12}}$. A grouping of points is evident, with compounds whose B-element is cobalt, nickel, iridium or platinum lying near the upper line, and those whose B-element is copper lying near the lower line. The apparent lesser contraction of copper cannot be compared at this time with Laves or AB_3 compounds.

Probably the most definite factor controlling the crystal structure of AB_5 compounds is the size factor. A rather sharp division exists at R_A/R_B ratios of 1.29-1.30. Below this ratio only the UNi_5 type is found; above it only the $CaCu_5$ type. The sensitivity to size factor is in contrast to the Laves phases, in which either crystal structure may be found over a wide range of radius ratios. The effect of size factor explains why zirconium, hafnium and uranium form the UNi_5-type compound with nickel, but thorium forms the $CaCu_5$ type with nickel. The location of A- and B-elements in the periodic table is quite definite, although this may derive at least in part from the size effect, as members of some groups are all large, and of others all small. Figure 24 shows a radial form of the periodic table, in which thorium is a member of the titanium group

Figure 24

Pattern of Elements Which Form $CaCu_5$-Type AB_5 Compounds

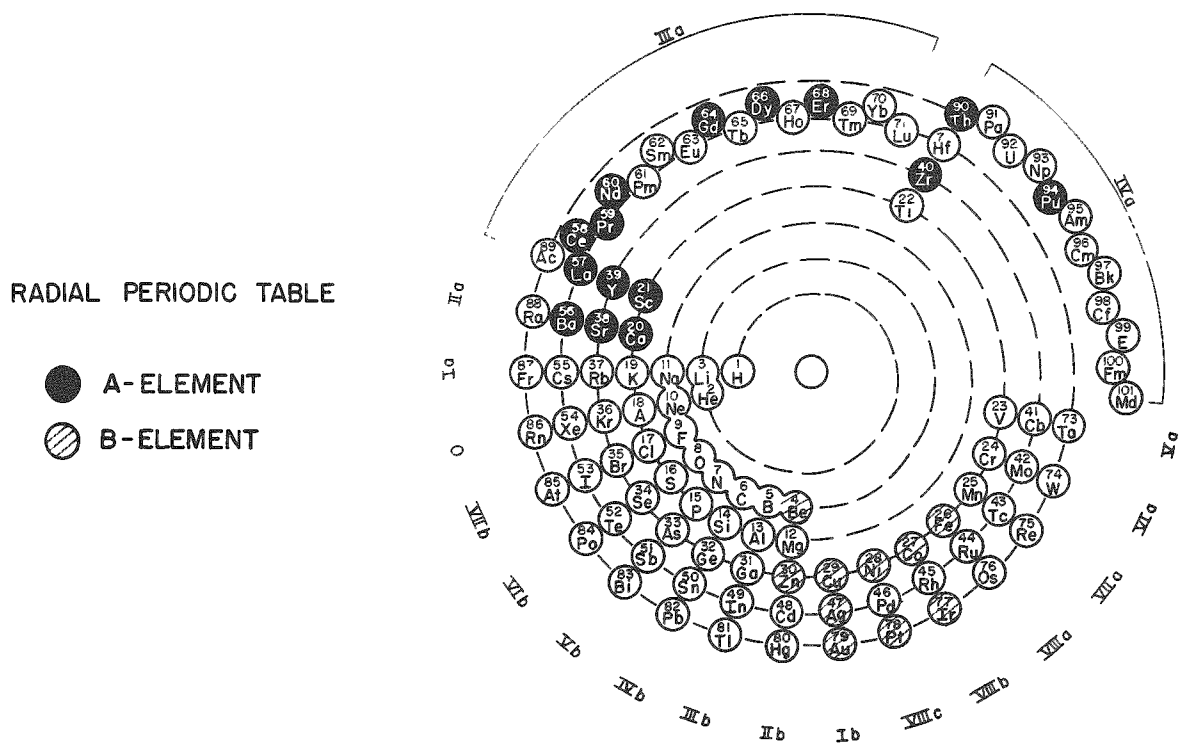

Micro 26625

and is also the zero member of a "thoride"series. On this table are superimposed the A- and B-elements known to form $CaCu_5$-type compounds, including all compounds from the literature as well as ANL work.

A feature of the hexagonal $CaCu_5$-type compounds is that the axial ratio lies close to 0.80. Yet a closer inspection reveals a relation between the axial ratio and the radius ratio, as shown in Figure 25.

Figure 25

Axial Ratio Versus Radius Ratio in $CaCu_5$-Type AB_5 Compounds

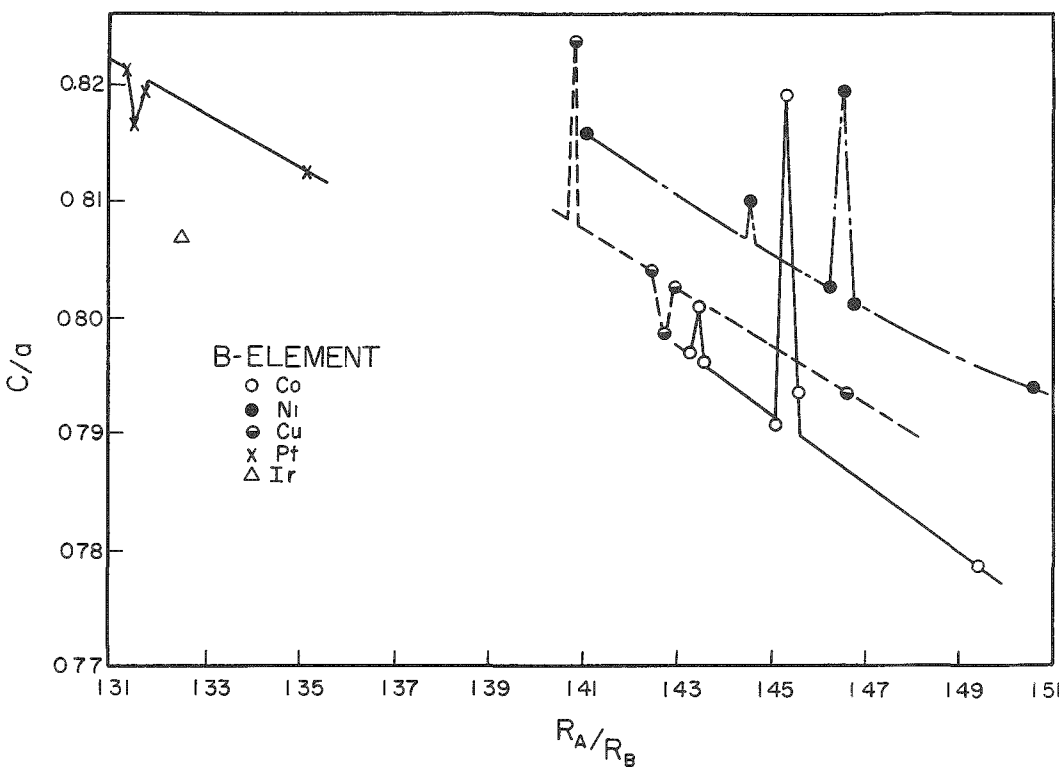

Micro 26655

For each B-element, the axial ratio decreases smoothly with increasing radius ratio, with the exceptions of cerium, which deviates from the curve, and yttrium, which always lies above the curve. The deviation in the c/a of the AB_5 alloys containing cerium appears to be due to the same cause as the deviation of cerium from the line of D_{AB}-d_{AB} contraction in the equiatomic AB alloys, referred to in an earlier section of this report. Other workers[15] have reported similar phenomena with regard to cerium, and have advanced the tentative explanation that cerium may have a +4 valence, in contrast to a +3 for other rare earths, and therefore cerium may have a smaller than expected effective radius.

[15] J. H. Wernick and S. Geller, Transition Element-Rare Earth Compounds with the $CaCu_5$ Structure, Acta Cryst. 12 662 (1959).

α-Mn-type Compounds: A study of the α-Mn-type compounds is under way to determine the factors controlling the occurrence of the compound. Table XI lists the systems investigated and the results.

TABLE XI

Occurrence of α-Mn-type Compounds

System	a_0, Å	a/o B
Ta-Os	9.659	66
Nb-Os	9.640	66
Zr-Re	9.75	83
Hf-Re	9.711	83
Th-Re		None found*
U-Re		None found*
Nb-Ru		None found**

*One composition investigated, 83 a/o Re.

**Three compositions investigated: 60, 65, 75 a/o Ru.

The α-Mn-type structure occurs only when the A-element lies in the titanium, vanadium or chromium groups (i.e., to the left of the manganese group) and the B-element is either rhenium or osmium. This implies that the combination of an electropositive A-element and an electronegative B-element can synthesize the necessary electronic arrangement to stabilize an α-Mn-type compound. In the Nb-Os and Ta-Os systems, the AB_2 composition has the α-Mn-type structure.

Ti_2Ni-type Phases: The discussion of the Ti_2Ni-type structure in the 1958 Annual Report dealt with the interpretation of the occurrence of the compound in the ternary systems Ti-Mn-O, Ti-Fe-O, Ti-Co-O and Ti-Ni-O. During the past year the qualitative correlation with valency electron concentration has been applied to the more general case of the occurrence of the same phase in the systems in which titanium, zirconium or hafnium is paired with a B-partner from the first, second or third long period, with and without oxygen as a third component. The phase is regarded as a kind of electron compound with oxygen exerting a stabilizing role through its effect on the valency electron concentration. The essential points of the hypothesis are the following: (1) Oxygen acts as an electron acceptor, reducing the electron concentration and thereby stabilizing the phase in systems where the electron:atom ratio is otherwise unfavorably high. (2) The minimum oxygen content required for stability can be correlated with the B-partner valency which, within a given long period, is assumed to decrease with increasing atomic number. (3) The upper limit of oxygen solubility

occurs when the 16 (c) positions of the O_h^7 - Fd 3m space group are filled. These positions are interstitial with respect to the 96 metal atom positions.

It has been found that the occurrence of all of the isostructural phases containing titanium, zirconium or hafnium is consistent with this hypothesis. Several interesting side effects are these: (1) Titanium and zirconium exhibit essentially the same valency in this compound, but the valency of hafnium is significantly lower (2) Rhodium and palladium and iridium and platinum have higher valencies than their respective first long period members, cobalt and nickel, in keeping with the observation made by Hume-Rothery and Coles[16] that among elements of the iron, cobalt and nickel groups there is a tendency toward higher valencies in the later periods. (3) The larger atomic radii of second and third long period elements introduce a weak size factor effect that was not evident from prior work. The radius ratios of all of the compounds fall between 1.05 and 1.27, with a peak in frequency of occurrence at 1 17. (4) When the B-partner is manganese, the metal components exhibit AB stoichiometry rather than A_2B stoichiometry, irrespective of whether the A-partner is titanium, zirconium or hafnium These observations, together with the approximate composition boundaries of the phase in the ternary systems Zr-Fe-O, Zr-Rh-O, Zr-Ir-O, and Zr-Pt-O, are shown in Figure 26. Table XII lists the new Ti_2Ni-type phases found, and their lattice parameters.

TABLE XII

New Ti_2Ni-Type Phases

System	Composition (a/o)	a_o Å
Ti-Rh-O	57.3 Ti, 28.7 Rh 14 O	11.585 ± 0.001
Ti-Ir-O	57.3 Ti 28.7 Ir 14 O	11.6198 ± 0.0005
Zr-Pd-O	57.3 Zr, 28.7 Pd, 14 O	12.458 ± 0.001
Zr-Fe-O	63.5 Zr, 31.5 Fe, 5 O	12.189 ± 0.001
Hf-Mn	50 Hf 50 Mn	11.812 ± 0.001
Hf-Fe	66.7 Hf 33.3 Fe	12.0555 ± 0.0005
Hf-Co	66.7 Hf, 33.3 Co	12.1036 ± 0.0004
Hf-Ru-Ni	67 Hf, 10 Ru 23 Ni	12.1730 ± 0.0007
Hf-Os-Ni	67 Hf 10 Os 23 Ni	12.1794 ± 0.0004

A logical extension of the study of valency effects has been concerned with the occurrence of the phase in five ternary systems having in each case hafnium and nickel as two of the components, and cobalt, rhodium, iridium, ruthenium, or osmium as the third component. Starting with the assumption that Ti_2Ni-type phase does not occur in the binary Hf-Ni system because the electron/atom ratio is too low, the following two predictions can be readily made.

[16] W. Hume-Rothery and B R. Coles, The Transition Metals and Their Alloys Advances in Physics 3 149 (1954)

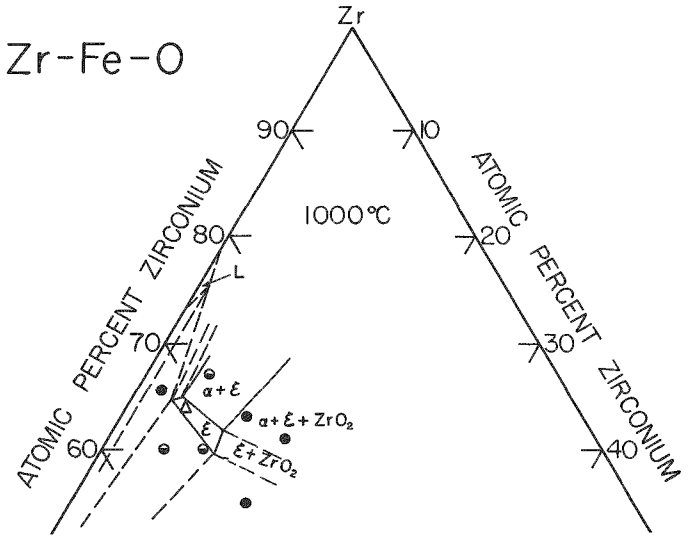

Micro 25695

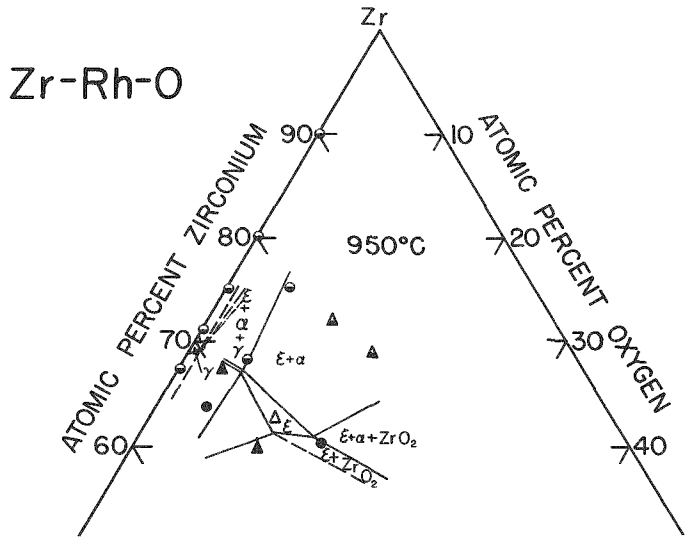

Micro 25187

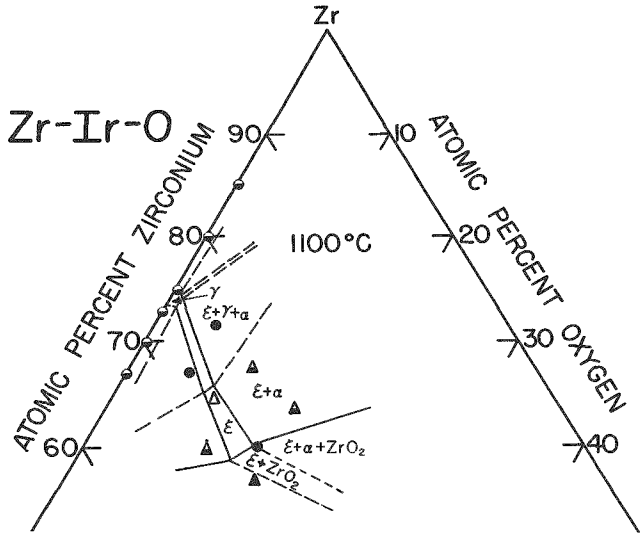

Micro 25188

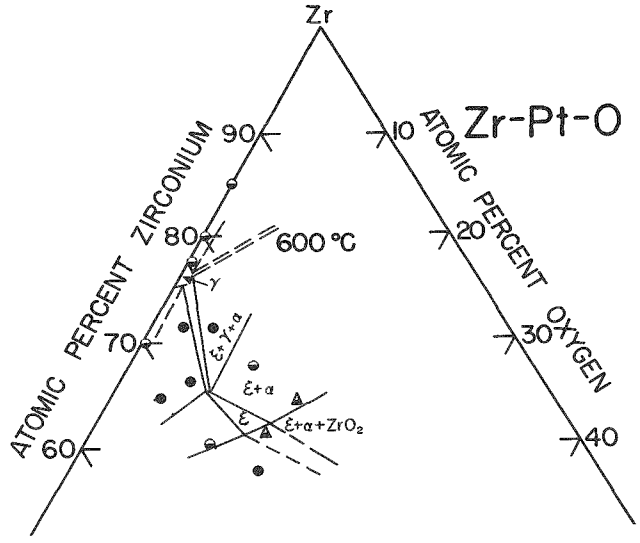

Micro 25189

Figure 26. Boundaries at 950°C of the Ti_2Ni-type Phase in the Systems Zr-Fe-O, Zr-Rh-O, Zr-Ir-O and Zr-Pt-O

1. The extent of replacement by nickel of cobalt, rhodium and iridium in the Ti_2Ni-type phases Hf_2Co, Hf_2Rh and Hf_2Ir should increase in the sequence Co → Rh → Ir, in keeping with the increasing valency of Co-group elements with increasing period number.

2. The electron:atom ratios for the compositions Hf_2Ru and Hf_2Os are probably too high for Ti_2Ni-type phases to be stable, but favorable electron:atom ratios should occur at certain ternary compositions in the systems Hf-Ni-Ru and Hf-Ni-Os.

Sufficient data have now been collected to show that both of these predictions are correct. Figure 27 shows the approximate location of the Ti_2Ni-type phase fields in these systems. Further work is under way to determine the composition boundaries with greater accuracy.

Figure 27

Approximate Boundaries at 1100°C of the Ti_2Ni-type Phases in the Ternary Systems Hf-NiCo, Hf-Ni-Rh, Hf-Ni-Ir, Hf-Ni-Ru and Hf-Ni-Os

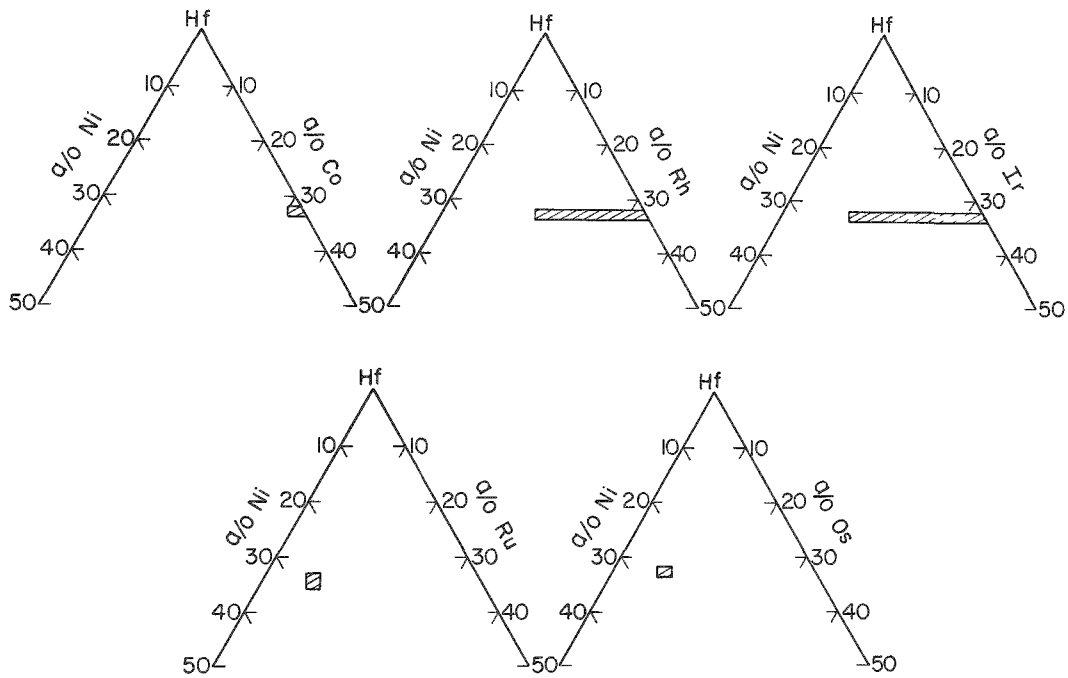

Micro 26669

These favorable results have strengthened our confidence in the electron compound concept, and we now believe that we are justified in deriving a set of empirical valency numbers for all of the component elements and assessing the critical limits of the electron:atom ratio corresponding to the stability of the phase. This will be done during the coming year, and an attempt will then be made to treat these empirical valency electron concentration limits in terms of Brillouin zone concepts. If a

Brillouin zone model can be derived for this structure, the expected interactions between the Fermi surface and the zone boundaries can be studied by magnetic susceptibility measurements.

Hf-Co Equilibrium Diagram: Work on the Hf-Co system is continuing. The tentative equilibrium diagram is shown in Figure 28.

Figure 28
The Hf-Co Equilibrium Diagram

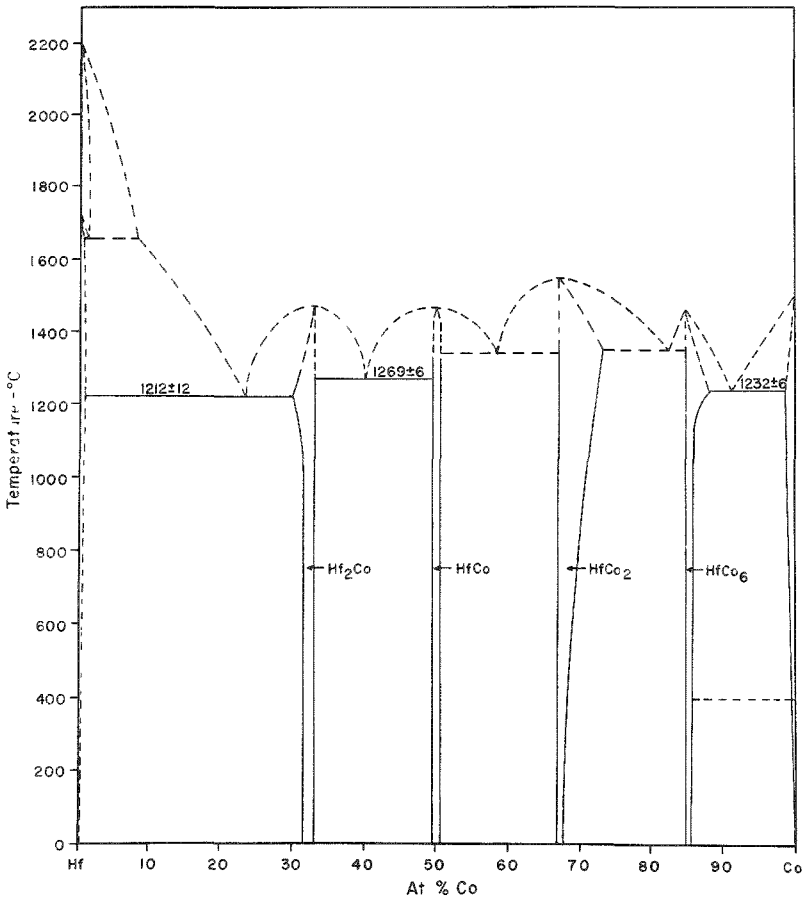

Micro 26109

The Zr-Co-O and Zr-Ni-O Ternary Systems: Initial interest in the binary systems Zr-Co and Zr-Ni, and the corresponding ternary systems with oxygen, stemmed from the belief that a Ti_2Ni-type phase might occur in one or more of them. It now appears certain that, due to an unfavorable size factor, none of these systems contains a Ti_2Ni-type phase, although both binary diagrams contain compounds having A_2B stoichiometry. Zr_2Ni has been reported to be isostructural with

$CuAl_2$[17] while the structure of Zr_2Co has not been described. We have continued to study the two ternary systems with oxygen because of our discovery in each system of an oxygen-stabilized phase which occurs in a narrow, elongated phase field very similar in appearance to the Ti_2Ni-type phase fields previously discussed. An important difference, however, is the fact that the two new phases are based upon A_3B stoichiometry for the metal components rather than the A_2B stoichiometry of the Ti_2Ni-type phases. The two phases give essentially identical diffraction patterns suggesting that they are isostructural compounds. However, attempts to index the patterns have thus far been unsuccessful. The zirconium-rich corners of the 950°C isothermal sections are shown in Figure 29.

Figure 29

The Zirconium-rich Corners in the Ternary Systems Zirconium-Cobalt-Oxygen and Zirconium-Nickel-Oxygen

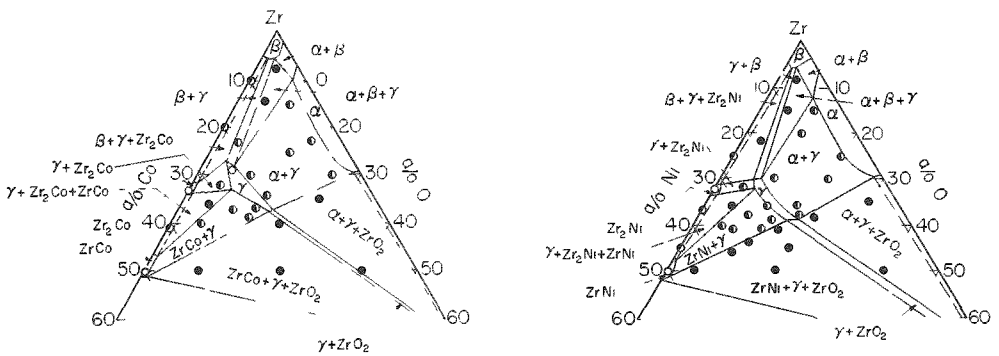

Micro 26719 Micro 26720

2. Occurrence and Magnetic Properties of C^8 and Sigma Phases (M. V. Nevitt)

Iron-Vanadium: The work on two alloys in this system during the past year was both an extension of the study of the CsCl-type phase and the initial step in the study of the magnetization of the sigma phase. As a result of the work on TiFe, an interesting correlation was observed between the magnetization and the lattice contraction for equiatomic alloys of iron with titanium, vanadium and chromium. However, the magnetization of FeV was derived from an extrapolation of data on iron-rich alloys, and it was considered necessary to check the validity of the correlation by determining the magnetization of one or more Fe-V alloys in the vicinity of the equiatomic composition. Accordingly the saturation magnetizations of the two alloys 60 Fe-40 V and 53 Fe-47 V in the metastable alpha-phase condition were determined by means of magnetic isotherms at 9, 51, 79, and 297°K. The curves of specific magnetization versus internal field for

[17] J. F. Smith, W. E. Kirkpatrick, D. M. Bailey and D. E. Williams, Crystallographic and Phase Relationships of the Nickel-Zirconium and Nickel-Hafnium Systems, ISC-1050 (June 1958).

the 53 Fe-47 V alloy are shown in Figure 30. In Figure 31 are shown the results of the present work and the older data of Fallot.[18] It is not yet certain how our new data should be interpreted. The anomalously low value for the 53 a/o Fe alloy may be due to a genuine bending over of the curve, as is thought to occur in chromium-rich Fe-Cr alloys. On the other hand, the examination of the metallographic control samples which were heat treated and quenched along with the magnetic specimens (0.2-in. diameter spheres) indicated that it is difficult to suppress the transformation to sigma in these alloys. It is therefore possible that the 53 a/o Fe alloy sphere, which was quenched at a slightly slower rate than the 60 a/o Fe alloy, has a lower apparent magnetization because it has undergone a partial transformation to the sigma phase. The latter assumption has been tentatively adopted in Figure 31 by fitting a straight line to Fallot's data and our 60 a/o Fe data point. The saturation magnetization of the 53 a/o Fe specimen will be redetermined after it has been reheated and given a more drastic quench. The critical evaluation of the magnetization versus lattice contraction relation must await the outcome of this additional work.

Figure 30

Specific Magnetization Versus Internal Field for 53 a/o Iron-47 a/o Vanadium Alloy

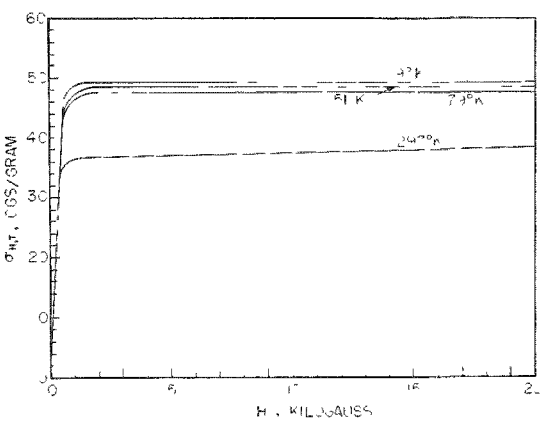

Micro 26717

Figure 31

Saturation Magnetization Versus Composition for Iron-Vanadium and Iron-Chromium Alloys

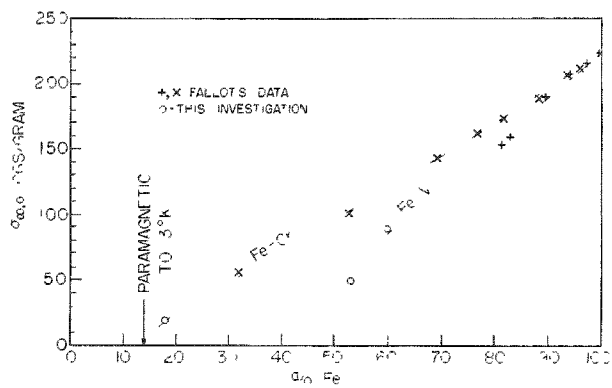

Micro 26718

The next step is to transform the two alpha-phase specimens to the stable sigma phase, and redetermine the magnetization. The equilibrating heat treatment for the 60 a/o Fe specimen is now in progress. The evaluation of the influence of crystal structure on the type and magnitude of the magnetizations of these two alloys should provide an insight into the shift in bond character that accompanies the transformation from the alpha to the sigma phase.

---

[18] M. Fallot, Ferromagnetism of the Alloys of Iron, Ann. Physique 6 305 (1936).

Iron-Chromium: This work, representing somewhat of a digression from the original goal of the program, has been a collaborative effort with Professor Paul A. Beck and his associates at the University of Illinois, who have measured the specific heat of chromium-rich Fe-Cr alloys. These workers have found an unusually large value for the term linear in T in the vicinity of 19 a/o Fe. In the interpretation of this effect as being representative of the electronic specific heat, much importance attaches to being able to show that it is not due to the magnetic transformation. Our contribution has been to study the magnetic behavior of three alloys containing 14, 18, and 19 a/o Fe. The following results have been obtained: (a) Cr-14 a/o Fe. This alloy remains paramagnetic down to the lowest temperature we have obtained in our cryostat, about 3°K. This result is consistent with that reported by Arrott[19] for a Cr-15 a/o Fe alloy. (b) Cr-18 a/o Fe. A saturation magnetization, $\sigma_{\infty,0}$, equal to 0.175 Bohr magnetons per atom was determined from a series of magnetic isotherms at 8, 26, 37, 48, 60 and 79°K. The Curie temperature of this ferromagnetic alloy is well above 26°K. (c) Cr-19 a/o Fe. Work on this alloy, as yet incomplete, indicates that it is paramagnetic as low as 51°K, but probably goes ferromagnetic at lower temperatures.

The fact that the 18 a/o Fe alloy, and probably the 19 a/o Fe alloy as well, have Curie temperatures above 25°K, offers strong support for the belief that peak in the term linear in T, seen at 1.5 to 4°K, is not due to the magnetic transformation, but may be interpreted in terms of electronic specific heat.

In Figure 31, the $\sigma_{\infty,0}$ value for the 18 a/o Fe alloy is shown, together with the older data of Fallot for Fe-Cr alloys. Our data indicate that the nonlinearity of $\sigma_{\infty,0}$ with iron content, proposed by Arrott,[20] must begin at an iron content lower than 18 a/o

3. Occurrence of the CsCl-Type Structure in Transition Element Alloys (A. E. Dwight)

Publication:

1. A. E. Dwight, "CsCl-Type Equiatomic Phases in Binary Alloys of Transition Elements," Trans. AIME 215 283-286 (April 1959).

A further study has been made of the occurrence of equiatomic structures. Newly discovered compounds are listed in Table XIII. It was noted that the lattice contraction $D_{AB}-d_{AB}$, for compounds between silver as a B-element and yttrium and the lanthanides as A-elements, shows an orderly relation to the radius ratio R_A/R_B. This relation is

[19] A. Arrott, Magnetization of Cr-rich Fe-Cr Alloys from 2°K to 300°K, Proceedings of the Boston Magnetism Conference (AIEE), 305 (1956).

[20] A. Arrott and H. Sato, Onset of Ferromagnetism with Increasing Fe Content in Fe-Cr Alloys, Bull. Am. Phys. Soc 3 42 (1958)

TABLE XIII

Lattice Contractions in Equiatomic Compounds

AB	Structure	a_0, Å	$D_{AB}-d_{AB}$, Å	R_A/R_B
GdCu	CsCl	3.505	0.045	1.41
ErCu	CsCl	3.432	0.063	1.375
ErAg	b.c.c.	3.58	0.101	1.217
LaAg	b.c.c.	3.802	0.026	1.30
CeAg	b.c.c.	3.758	0.014	1.263
NdAg	b.c.c.	3.722	0.042	1.261
PrAg	b.c.c.	3.734	0.038	1.266
HoAg	b.c.c.	3.594	0.098	1.223
DyAg	b.c.c.	3.61	0.091	1.228
SmAg	b.c.c.	3.678	0.061	1.248

reproduced in Figure 32. The deviation of cerium from the line through the other points is comparable to a similar observation on $CaCu_5$-type phases and is discussed in another section.

Figure 32

Lattice Contraction in Equiatomic Compounds Between Silver and the Lanthanides

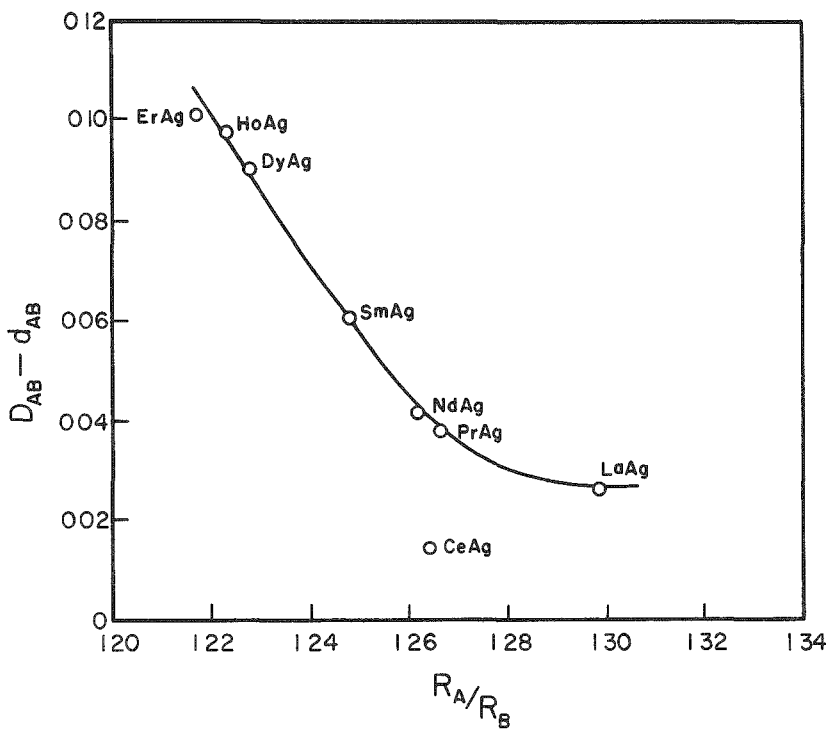

Micro 26654

The following additional equiatomic compounds were observed metallographically. The diffraction patterns have not been identified but are not of the CsCl-type: TiRh, TiIr, TiPd, TiPt, ZrPt, HfRh, HfIr, HfPt, NbPt.

4. Calorimetric Studies of Intermetallic Compounds of Transition Elements (J. B. Darby, Jr., and D. B. Jugle)

Initiated during 1959, this program was undertaken in recognition of the need for thermodynamic data in our study of bonding in intermetallic compounds and other alloys. The enthalpy or heat of formation of any compound, ΔH_f, is a measure of the difference between the total bond energy of the atoms in the compound and the sum of the bond energies of the component atoms in their pure elemental forms. At constant temperature, the relationship between the free energy, ΔF_f, the enthalpy, ΔH_f, and the entropy of formation, ΔS_f, is given by

$$\Delta F_f = \Delta H_f - T\Delta S_f \quad .$$

The entropy of formation is a measure of randomness which depends upon the configuration of the atoms in the compound and upon the difference in heat capacity between the alloy and the constituent elements. In general, the magnitude of the entropy factor is relatively small, and the magnitude and sign of ΔF_f are determined mainly by ΔH_f. Thus a knowledge of the heat of formation of a compound gives not only the bonding energy relative to that of the pure metals, but is generally a sufficient indication of the stability of the compound. Unfortunately, accurate thermodynamic data are available for only a few metallic systems,[21] and the inadequacy of the experimental methods used in the past has produced heat of formation data of limited accuracy.

Based on an evaluation of the experimental methods used in the past, a liquid-metal solution calorimeter of the twin design has been selected as the type that would yield the greatest accuracy and have the broadest application to measurement of the heat of formation of compounds of transition elements. The design of the calorimeter has been completed. It consists of two reaction chambers surrounded symmetrically by a massive thermostat which, in turn, is enclosed by a heater that is controlled with high precision. The above components are bound by several radiation shields and enclosed in a suitable vacuum-tight vessel. A twin preheat chamber, situated above the calorimeter proper, will preheat the specimens in order to aid the kinetics of solution. In addition, it will serve to heat inert specimens for calibration purposes to a known temperature prior to a calibration drop. This chamber will be adequately shielded from the laboratory environment. The calorimeter will be operated differentially by means of a thermopile whose junctions are alternately attached between each reaction chamber and the surface of the surrounding thermostat.

[21] O. Kubaschewski and J. A. Catterall, Thermochemical Data of Alloys, Pergamon Press, New York, New York (1956).

The selection of suitable metallic solvents is hindered by the modicum of data available on the kinetics of solution and solubility of transition elements and their alloys in low melting point metals that have low vapor pressures, such as tin, aluminum, and indium. An investigation is in process to obtain this information for transition elements of the first long period.

Upon construction and calibration of the calorimeter, compounds of transition elements of the first long period will be investigated first. This is an obvious choice, since most of the data for other physical properties have been acquired from alloys whose constituents are in this period. When accurate data on the heat of formation of the various compounds are available, a correlation with saturation magnetic moment data will be attempted in the hope that such correlations will contribute to an understanding of the nature of the bonds in intermetallic compounds.

E. X-ray and Neutron Diffraction Studies

1. Magnetic Structure of $(Mn,Co)_4C$ (S. S Sidhu)

The compound Mn_2Co_2C is cubic with the unit cell dimension $a_0 = 3.78$ Å. Its magnetic structure, recently reported,[22] is deduced on the basis that the carbon atom is in the central $\frac{1}{2}$ $\frac{1}{2}$ $\frac{1}{2}$ site and the metal atoms are ordered, with the manganese atoms in the 0 0 0 and $\frac{1}{2}$ $\frac{1}{2}$ 0 sites, and the cobalt atoms in the $\frac{1}{2}$ 0 $\frac{1}{2}$ sites

A ternary alloy, $Mn_{1.75}Co_{2.25}C$, with a structure similar to Mn_2Co_2C, was preapared by alloying carbon with a binary alloy $Mn_{2.19}Co_{2.81}$. An X-ray diffraction pattern of the binary alloy shows that it is face-centered cubic with $a_0 = 3.618$ Å, but its neutron pattern gives no Bragg peaks since the manganese atoms scatter thermal neutrons 180° out of phase with those of cobalt atoms. Therefore, there is no ordering of the metal atoms in this alloy.

2. Diffraction of Neutrons by Krypton in the Liquid State (G. T. Clayton and L. Heaton)

A neutron diffraction study of krypton in the liquid state has been carried out with monochromatic neutrons of wave length 1.05 Å. With apparatus developed for this experiment, diffraction patterns were obtained over a temperature and pressure range from 117°K and 0.8 atmosphere (near the triple point) to 210°K and 54 atmospheres (above the critical point).

The atomic radial distribution function, the nearest neighbor distance, and the coordination number were determined for each case by Fourier inversion of the experimentally observed neutron scattering curves. A summary of these data follows.

[22] A. H. Holtzman and G. P. Conrad II, Structural and Magnetic Properties of Mn-Co-C Alloys, J. Appd. Phys. 30 (4) 103S-104S (April 1959).

Temperature (°K)	Pressure (Atmospheres)	Density (Atoms/Å^3)	Nearest Neighbor Distance (Å)	Coordination Number
117	0.8	0.0176	4.02	8.5
133	2.6	0.0166	4.04	8.0
153	7.0	0.0154	4.08	7.0
183	24.2	0.0130	4.10	6.5
210	54.0	0.0075	4.20	4.0

3. Neutron Coherent Scattering Amplitudes (S. S. Sidhu, L. Heaton and M. H. Mueller)

Publication:

1. S. S. Sidhu, LeRoy Heaton and M. H. Mueller, "Neutron Diffraction Techniques and Their Applications to Some Problems in Physics," J. Appd. Phys. 30 1323-1340 (1959).

The coherent scattering amplitude for indium was reported in the above paper as $+0.36 \times 10^{-12}$ cm. This value was obtained from neutron diffraction patterns of indium metal and the compound InSb.

A summary of the neutron coherent scattering amplitudes for the titanium isotopes, as determined here at Argonne and at Oak Ridge, is given in Table XIV.

TABLE XIV

Neutron Scattering Data for the Titanium Isotopes

	b_{coh} ($\times 10^{-12}$cm)	σ_{coh} (barns)	$\sigma_{Total\ Scattering}$ (barns)
Ti^{46}	+0.48	2.90	2.1
Ti^{47}	+0.33	1.37	1.3
Ti^{48}	-0.58	4.23	3.7
Ti^{49}	+0.08	0.08	L 1.0
Ti^{50}	+0.55	3.80	3.5
Ti (element)	-0.34	1.45	4.0

We are planning to continue to obtain neutron scattering data for a number of different isotopes as they become available in sufficient amounts. Currently the following isotopes are being considered: Zr^{90}, Zr^{91}, Zr^{92}, and Zr^{94}; K^{39} and K^{41}; Cl^{35} and Cl^{37}; and Rb^{85} and Rb^{87}.

4. Structure of Alkali Metals in the Liquid State (N. S. Gingrich* and LeRoy Heaton)

Neutron diffraction patterns were obtained for the following alkali metal liquids: lithium (453°K), sodium (373°K), potassium (338°K), rubidium (313, 433, 513, and 633°K), and cesium (303, 573 and 848°K). Atomic distribution curves were computed for all the above cases and compared with results from X-ray diffraction studies of lithium, sodium and potassium. Just above melting temperatures the nearest neighbor distances are for lithium, 3.15 Å; sodium, 3.82 Å; potassium, 4.64 Å; rubidium, 4.97 Å; and cesium, 5.31 Å; and the number of nearest neighbors is, within one-half atom, about 9.0 to 9.5 atoms in each case. At elevated temperatures in rubidium and cesium, a weak subsidiary concentration of atoms appears between the usual first and second-neighbor concentration.

5. The Urania-Thoria System (M. H. Mueller)

It has been reported that a cubic phase is obtained upon heating U_3O_8 with ThO_2.[23] In the intermediate composition ranges, two "cubic" diffraction patterns are observed, one of which has a lattice parameter smaller than that obtained from a corresponding composition of UO_2-ThO_2 which has been fired in a hydrogen atmosphere. Since it is reasonable to suppose that in the U_3O_8-ThO_2 compositions there are U^{+6} ions present as well as excess oxygen, in terms of the UO_2-ThO_2 compositions, it was of interest to determine if the "cubic" phase with smaller lattice parameter consists of a fluorite structure with essentially all oxygen sites occupied, but a deficiency of metal ions in the other sites which might account for the decreased lattice parameter.

In order to check this possibility, two samples were prepared for neutron diffraction: one sample of 50 m/o UO_2-50 m/o ThO_2 fired in H_2 at 1650°C for 15 hours, and another sample of U_3O_8-ThO_2 prepared with equal molar concentrations of uranium and thorium and heated in air at 1450°C for 90 hours. The X-ray diffraction patterns of the two samples showed a single cubic phase for the UO_2-ThO_2 material and two "cubic" patterns in the U_3O_8-ThO_2 sample. The strongest "cubic" pattern from the latter material has a lattice parameter considerably smaller than that observed in the UO_2-ThO_2 material, and the other very weak pattern has a lattice parameter more nearly the same as the UO_2-ThO_2.

*University of Missouri, Consultant to ANL Metallurgy Division.

[23] F. Von Hund and G. Niessen, Anomale Mischkristalle in System Thoriumoxyd-Uranoxyd, Z. Elecktrochem. 56 972 (1952).

If the composition of this material is written as $(U, Th)_{1-x}O_2$, where x = 0 for the UO_2-ThO_2, and if it is assumed that x = 0.15 for the U_3O_8-ThO_2 sample, then the calculated relative intensities for the first three peaks in a neutron diffraction pattern are considerably different for the two samples, as indicated in Table XV.

TABLE XV

Comparison of Calculated and Observed Relative Intensities for UO_2-ThO_2 and U_3O_8-ThO_2

	UO_2-ThO_2		U_3O_8-ThO_2	
	Calculated	Observed	Calculated	Observed
111	34.1	36.8	28.3	32.5
200	3.2	1.4	9.5	nil
220	100.0	100.0	100.0	100.0

There is better agreement between calculated and observed intensities for the UO_2-ThO_2 than for the U_3O_8-ThO_2. It was noted that the neutron pattern for the U_3O_8-ThO_2 sample was similar to that obtained for UO_{2+x} type material, where x is approximately 0.25 to 0.33. Additional work is necessary to determine the nature of these oxide phases.

6. Neutron Diffraction Spectrometer (S. S. Sidhu, LeRoy Heaton and M. H. Mueller)

Construction of the horizontal spectrometer of a dual neutron spectrometer instrument for use at the CP-5 reactor is nearing completion. It has been designed with a number of special features, such as (1) Two monochromators are to be used in an in-line arrangement for use with two independent spectrometers, one a large horizontal instrument and the other a smaller vertical spectrometer. (2) The horizontal spectrometer arm will pivot about the center of the spectrometer table or may also be made to pivot about a point approximately 2 feet from the center of the table. This arrangement permits the use of the instrument for crystal studies involving neutron energy change. (3) The horizontal table is constructed so as to support massive accessories, such as cryostat, furnace and magnet. (4) The movement of the horizontal spectrometer arm may be continuous or in variable steps. (5) The powder diffraction patterns are to be recorded by an x-y recorder and, in addition, the intensity versus angle data are printed automatically on paper with an electric typewriter. (6) The two monochromating crystals may be used in transmission or reflection, and each crystal may be accurately positioned by external controls. (7) Considerable variation in primary beam wave length may be made by changing the take-off angle from the monochromator crystals by means of

interchangeable "pie-shaped" segments. (8) The monochromating crystals are located inside a relatively small, heavily shielded housing which consists of lead, steel, and depleted uranium walls. (9) The monochromator housing is surrounded with a large moderating shield which consists of stacked, 2-in. thick Masonite sheets which have a total minimum thickness of 2 feet from the inner housing. (10) The vertical spectrometer which is planned for single-crystal investigations will have a single-crystal goniostat which will be in many ways similar to the General Electric X-ray instrument. Although it is planned to make this single-crystal unit fully automatic, using a taped input program, it will initially be semiautomatic.

The horizontal spectrometer should be in operation very soon, since all construction has been completed except for a small amount of machining on the large spectrometer table, and the assembly at the reactor has been completed except for this subassembly. The shielding has been tested with the beam-hole open and found to be quite satisfactory.

7. High-temperature X-ray Diffraction Furnace (M. H. Mueller)

The high-temperature furnace for use on the G. E. X-ray diffractometer has been completed. The furnace was designed with a number of special features such as: (1) provision for moving the sample in and out of the focusing circle with an exterior control; (2) metal vacuum seals, such as gold and lead; (3) provision for moving θ with respect to 2θ; (4) use of an ion vacuum pump for attainment of a good vacuum and for permitting the removal of all external vacuum connections after initial rough pumping so that there will be no obstruction for the diffractometer arm movement; (5) stainless steel construction in order to present a clean, polished surface on the inside of the furnace; and (6) minimum volume for the furnace and associated vacuum equipment.

To date we have had good success in heating samples up to 700°C, still maintaining the vacuum in the 10^{-7} mm range. During initial calibration, six Pt-Rh thermocouples were imbedded in a nickel sample, $\frac{3}{4} \times 1\frac{1}{4} \times \frac{1}{6}$ in. thick, in order to determine the gradient. Results showed a variation of $\pm 1.5°$ at 600°C, which increased to approximately $\pm 5°$ at 1000°C. Pumping time with the ion pump is very satisfactory.

F. Problems in Metal Physics

1. Studies on Diffusion in Anisotropic Metals

Self-diffusion in Uranium (S. J. Rothman)

Publications:

1. S. J. Rothman and L. J. Sobocki, "Precision Chuck and Chip Catcher for Sectioning Diffusion Samples," Rev. Sci. Instr. 30 201-202 (1959).

2. R. Weil, S. J. Rothman and L. T. Lloyd, "Preparation of Diffusion Couples by Cathodic Sputtering," Rev. Sci. Instr. 30 541-543 (1959).

3. S. J. Rothman, L. T. Lloyd, R. Weil and A. L. Harkness, "Self-Diffusion in Gamma Uranium," ANL-5971 (July 1959).

The first paper describes a chuck that allows one to line up a diffusion sample in a sectioning lathe so that the original surface on which the isotope layer was deposited is perpendicular to the lathe axis. Also, an effective chip catcher for use with the chuck is described.

The second paper describes a technique for removing adsorbed gases and oxide layers from a diffusion sample and depositing a thin layer of another uranium isotope on the surface of the sample.

The third publication describes studies of self-diffusion in gamma uranium. The diffusion samples were prepared by the method described in the second of the above papers, annealed and sectioned, using the chuck and chip catcher described in the first paper. The sections were analyzed mass spectrographically. The results combined with the results of other authors[24,25] could be described by an Arrhenius equation with the following constants:

$$D = 1.12 \times 10^{-3} \exp(-26{,}500 \text{ cal}/RT) \text{ cm}^2/\text{sec} \quad .$$

---

[24] A. A. Bochvar, V. G. Kuznetsova, and V. S. Sergeev, Self-Diffusion of Uranium in Gamma Phase, Second U.N. International Conference on Peaceful Uses of Atomic Energy, Geneva (1958), Vol. 6, p. 68.

[25] Y. Adda and A. Kirianenko, Etude de l'autodiffusion de l'uranium en phase gamma, Compt. Rend. 247 744 (1958).

The results indicated that the values of the activation energy and the D_0 were anomalously low. The work of the past year has therefore been devoted to experiments designed to elucidate the significance of the low values of these parameters.

Because of the strong disagreement of the diffusion parameters with those deduced on the basis of the vacancy mechanism, the possibility was considered that another mechanism, such as the ring mechanism, might be operative in self-diffusion in gamma uranium. Pound et al.,[26] proposed the same reason for the anomalously low D_0 and activation energy values for self-diffusion in chromium,[27] and gave some statistical mechanical calculations supporting this thesis. We have tried to run a critical experiment which would test this hypothesis and define the mechanism.

An obvious experiment of this kind is the measurement of the activation energy for vacancy formation. This is usually done by quenching and subsequent resistivity measurements,[28] simultaneous dilatometry and lattice parameter measurements,[29] or dilatometry.[30] None of these are suitable for gamma uranium. The first cannot be used because the strains introduced into polycrystalline alpha uranium by the beta-alpha transformation and by rapid cooling through the alpha phase would overshadow the effects due to vacancies. Further, the resistivity depends strongly on the texture, and the texture obtained on quenching is not always reproducible. Simultaneous dilatometry and lattice parameter measurements, and straight dilatometry would not work because in these experiments utilizing these techniques it is necessary to have a reference temperature at which the vacancy concentration is effectively zero. For gamma uranium, this temperature very probably lies below the beta-gamma transformation point.

---

[26] G. M. Pound, W. R. Bitler and H. W. Paxton, Theory of D_0 for Self-Diffusion in Solid Metals, private communication, to be published.

[27] H. W. Paxton and E. G. Gondolf, Die Geschwindigkeit der Selbstdiffusion in reinem Chrom, Arch. f. Eisenhuttenwesen 30 55 (1959).

[28] J. W. Kauffman and J. S. Koehler, The Quenching-in of Lattice Vacancies in Pure Gold, Phys. Rev. 88 149 (1952).

[29] R. Feder and A. S. Nowick, The Use of Thermal Expansion Measurements to Detect Lattice Vacancies Near the Melting Point of Pure Lead and Aluminum, Phys Rev. 109 1959 (1958).

[30] S. D. Gertsriken and B. F. Slyussar, On the Determination of the Energy of Formation of Vacancies and Their Number in Pure Metals, Fiz. Met. i Metalloved. 6 1061 (1958).

Sintering experiments offer a possible solution to the problem. By measuring the rates of neck growth as functions of time and sintering temperature, both the mechanism and activation energy of sintering can be determined.[31] If sintering takes place by volume diffusion it must involve point defects. Therefore, a comparison of activation energy for sintering with that for self-diffusion will show whether the latter takes place by a defect mechanism or not. For this reason we have undertaken to measure sintering rates in gamma uranium by several techniques. The first technique tried was the sintering of spheres to plates; no bonds were obtained. Attempts to observe the sintering of spheres in a microscope hot stage also failed to yield satisfactory results. Next we tried the wire-spool technique[32] with moderate success. These experiments are currently in progress.

In connection with the work on self-diffusion of gamma uranium, we thought it interesting to see whether the very rapid diffusion persisted into the beta phase. The techniques used were, with some exceptions, those used for gamma uranium: thin layers of the tracer isotope, U^{235}, were deposited either by cathodic sputtering or by vacuum evaporation on a sample cleaned by cathodic sputtering. After annealing, the samples were sectioned on a lathe. The sections are being analyzed for U^{235} by fission counting. Four samples, annealed at 678, 800, 730, and 760°C, respectively, have been sectioned and analyzed. Preliminary values for D at 700 and 760°C are 1.1×10^{-11} cm^2/sec and 3.3×10^{-11} cm^2/sec, respectively. These values are higher by a factor of 2 than those of Adda,[33] but they still confirm the large discontinuity in the log D vs 1/T curve at the gamma-beta transformation.

Attempts to grow alpha-uranium single crystals by Fisher's method[34] from an ingot of highly depleted, high-purity uranium for diffusion studies in the alpha phase have been unsuccessful, probably due to the

---

[31] G. C. Kuczynski, Self-Diffusion in Sintering of Metallic Particles, J. Metals 1 169 (1949).

[32] B. H. Alexander and R. W. Balluffi, Experiments on the Mechanism of Sintering, J. Metals 2 1219 (1950).

[33] Y. Adda, A. Kirianenko and C. Mairy, Etude de l'autodiffusion de l'uranium en phase β, J. Nuc. Mat. 1 300 (1959).

[34] E. S. Fisher, Preparation of Alpha Uranium Single Crystals by a Grain-Coarsening Method, Trans. AIME 209 882 (1957).

relatively poor chemistry of the material Large pseudo single crystals of this material have been grown by slow cooling across the α-β transformation temperature. We are presently attempting to perfect these crystals by Lacombe's method.[35] At the same time, oriented pseudo single crystals are being prepared. Diffusion studies on these samples may yield information on volume diffusion, or may indicate anisotropy effects due to diffusion along dislocations of different orientations.

Kirkendall Effect in Anisotropic Metals (J. B. Darby, Jr.)

Much of the effort expended on this program has been devoted to the development of techniques for preparation of satisfactory diffusion couples. In several preliminary trials, couples were fabricated using discs carefully prepared from single crystals of high-purity magnesium which were subsequently coated with high-purity cadmium by a combination of sputtering and electrochemical plating techniques. Initially the bond between the two component metals was unsatisfactory, however, a modification in the technique for surface preparation of the magnesium resolved this difficulty.

Preliminary results to date indicated that in portions of some of the diffusion couples having a good bond at the interface, magnesium, rather than cadmium, was the fast diffuser. This is contrary to the generalization observed in face-centered cubic metals, namely, that the component with the higher vapor pressure is the fast diffuser.[36]

It is not certain at present whether this is a true effect in hexagonal metals, in contrast to the behavior in face-centered cubic metals, or if it might not have been caused by grain boundary diffusion in the sputtered layer of the cadmium, the grain size of which varied from one couple to the other. To check this, sandwich-type couples prepared from materials with a controlled grain structure will be studied. The results of this investigation should decide for us which element is to be used in the form of single crystals and which element as the sputtered on layer in pursuit of our aim of determining the magnitude of the Kirkendall shift as a function of crystal orientation in hexagonal metals.

2. Elastic Moduli (E. S. Fisher)

The measurements of the fundamental elastic moduli of orthorhombic alpha uranium have been extended from room temperature down to -195°C. The techniques used were essentially the same as those described

[35] J. Mercier, D. Calais and P. Lacombe, Croissance de gros cristaux parfaits d'uranium alpha par ecrouissage et recuit de monocristaux polygonises obtenus par changement de phase, Compt. Rend. 246 110 (1958).

[36] R. W. Balluffi and L. L. Seigel, J. Appl. Phys. 25 607 (1954).

in last year's annual report. The wave-velocity data were obtained from a phase comparison technique in cooperation with H. J. McSkimin at the Bell Telephone Laboratories, using small single crystals of predetermined orientations prepared at ANL. The computations for deriving the moduli from the wave-velocity data and the thermal expansion data were carried out on the ANL IBM 704 computer.

The temperature dependence of the stiffness moduli is plotted in Figures 33 through 37. The curves were obtained by first fitting the experimental points to polynomials

$$c_{ij} = a_0 + a_1 T + \ldots\ldots a_n T^n \quad ,$$

where $a_0 \ldots a_n$ are coefficients obtained by least square analysis and T is temperature. The polynomials were then evaluated at equal intervals of T to obtain plotting points. The resulting curves are quite smooth and deviations from experimental points in all cases are less than 0.2%.

Figure 33

Stiffness Moduli c_{11} and c_{22}

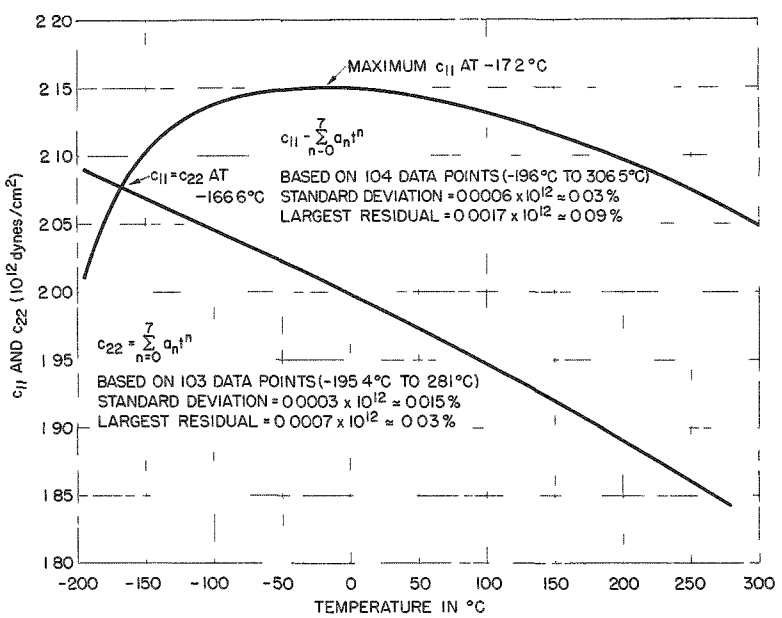

The dilational moduli, c_{11}, c_{22} and c_{33}, were obtained from the velocities of longitudinal waves propagated in the [100], [010] and [001] direction, respectively. The shear moduli, c_{44}, c_{55} and c_{66}, were obtained from the propagation velocities of two different shear modes.

Figure 34

Stiffness Modulus c_{33}

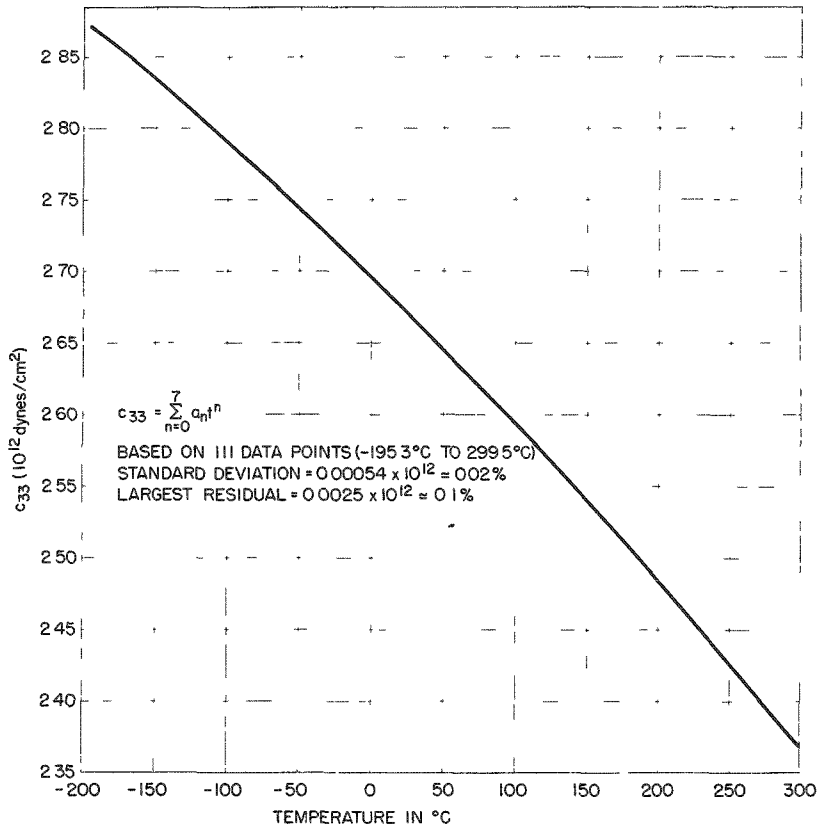

Figure 35

Stiffness Modulus c_{44}

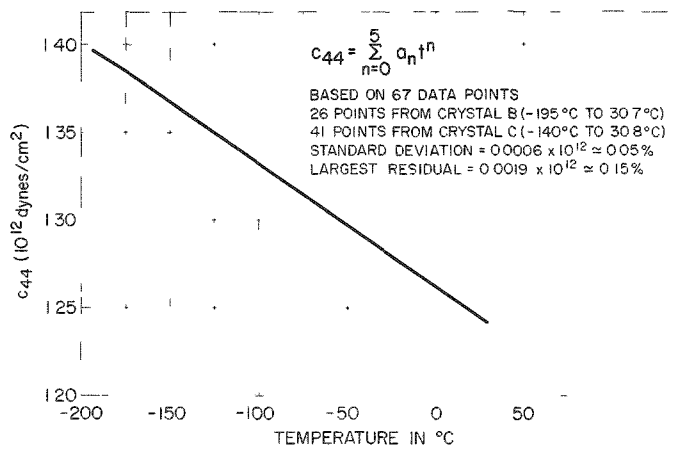

Figure 36

Stiffness Moduli c_{55} and c_{66}

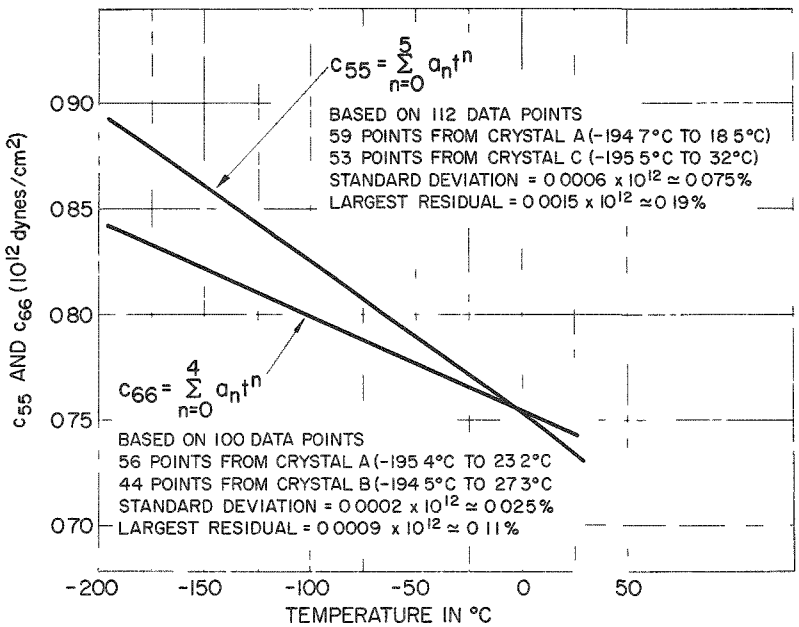

Figure 37

Temperature Dependence of Cross Coupling Moduli

Solid lines are polynomials fitted to c_{ij} from quasi-longitudinal data; open circles are c_{ij} computed from quasi-shear data.

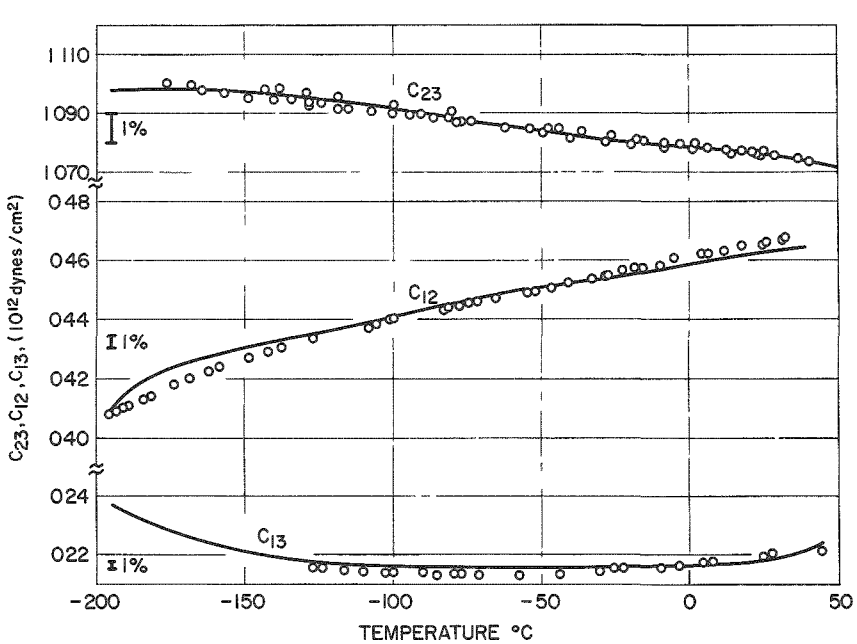

The combinations of wave propagation and particle displacement involved in each of these shear moduli were as follows:

Shear Modulus	Direction of Wave Propagation	Direction of Particle Motion
c_{44}	[001]	[010]
	[010]	[001]
c_{55}	[001]	[100]
	[100]	[001]
c_{66}	[100]	[010]
	[010]	[100]

The cross-coupling moduli, c_{12}, c_{13} and c_{23}, were obtained from velocities of quasi-longitudinal or quasi-shear modes propagated in three different directions which are 90° to one principal axis and inclined to the other two. The curves in Figure 37 represent moduli evaluated using quasi-longitudinal mode data fitted to polynomials; the open circles represent experimental points obtained from quasi-shear mode data. The largest deviation between the independently derived data is about 1%.

Table XVI summarizes the temperature coefficients, $R = \frac{1}{c_{ij}} \frac{dc_{ij}}{dT}$, at several temperatures. Figures 38, 39, 40, 41, and 42 give the variations with temperature of the principal Young's moduli, Poisson's ratios, and compressibilities.

TABLE XVI

Temperature Coefficients of Moduli Derived from Best Fit Polynomials

$$\left(R = \frac{1}{c_{ij}} \frac{dc_{ij}}{dT}\right)$$

Modulus	Temperature (°C)	R x 10^6/°C	Modulus	Temperature (°C)	R x 10^6/°C
c_{11}	-165	+812.9	c_{55}	25	-1063.5
	-17.2	0	c_{66}	25	-622.8
	25	-56.9	c_{12}	25	+326.9
	200	-188.7	c_{13}	-165	-1283.6
c_{22}	25	-250.8		-50	0
c_{33}	25	-377.8		25	+629.5
c_{44}	25	-557.9	c_{23}	25	-123.2

Figure 38

Temperature Dependence of Young's Moduli in [100] and [010] Directions

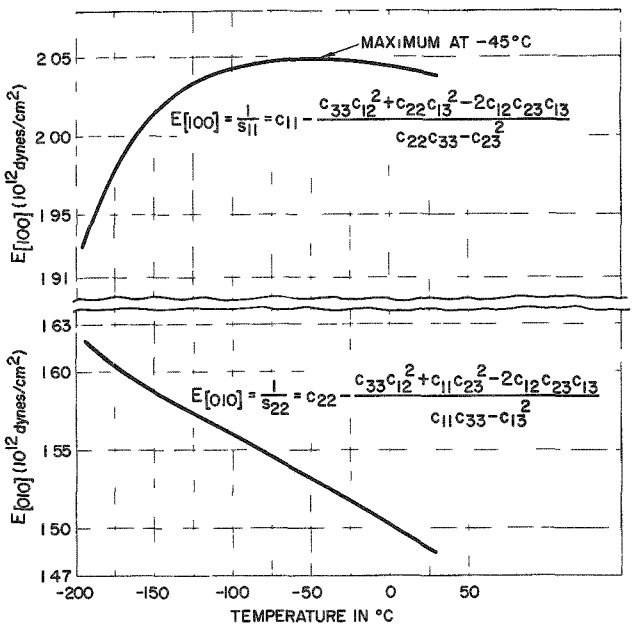

The striking deviations from the usual temperature dependence of elastic moduli are as follows:

(a) c_{11} and $E_{[100]}$ pass through maxima on cooling below 0°C and have large positive temperature coefficients at the low temperatures,

(b) the linear compressibility in the [100] direction increases quite markedly with decreasing temperature,

(c) Poisson's ratio for the [100]-[001] elastic coupling decreases inversely with temperature and becomes negative.

All of these anomalies are related to the [100] direction, or more specifically, to the second nearest neighbor interatomic bond. There is apparently a broad transition in the electron interaction contributing to this bond, the nature of which does not give rise to any reported peaks in specific heat or marked changes in crystal structure. There are, however, inconclusive data which indicate a negative thermal expansion coefficient for the [100] direction at temperatures below -200°C and an anomalous minimum in magnetic susceptibility for the bulk metal at approximately -100°C.[37,38] More careful studies of these properties at low temperatures are needed to establish definitely their existence and their possible relation to the elastic stiffness anomalies. Also, extension of the present studies to liquid helium temperatures is required to define completely the anomalies in elasticity.

---

[37] J. R. Bridge, C. M. Schwartz and D. A. Vaughan, X-ray Diffraction Determination of Coefficients of Expansion of Alpha Uranium, Trans. AIME 206 1282 (1956).

[38] L. F. Bates and S. J. Leach, The Magnetic Susceptibility of Palladium-Uranium Alloys, Proc. Phys. Soc. B69 997 (1956).

Figure 39

Temperature Dependence of Young's Modulus in [001] Direction

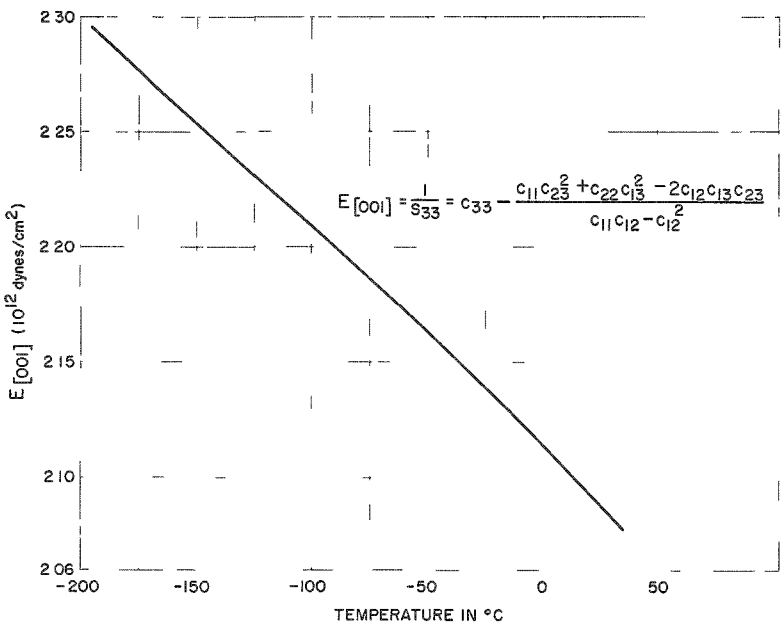

Figure 40

Temperature Dependence of Linear and Volume Compressibilities

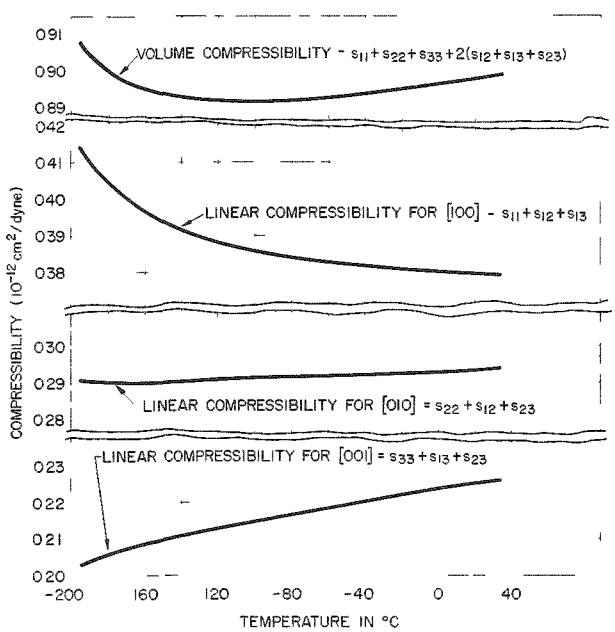

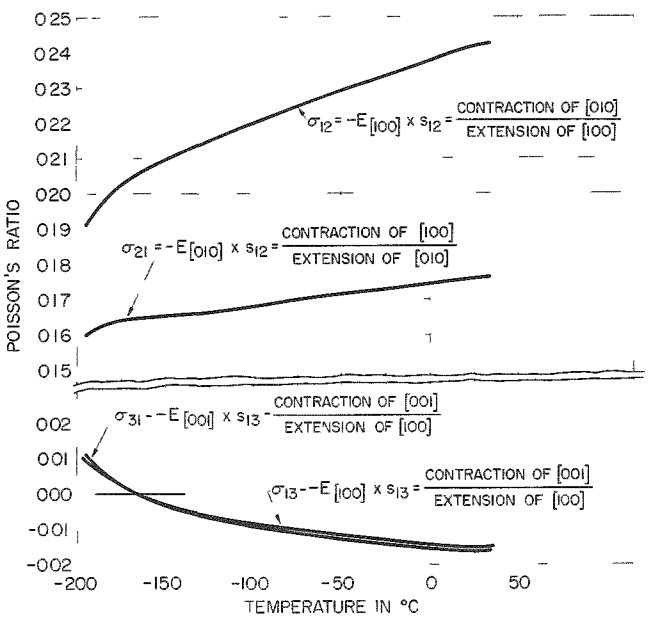

Figure 41

Temperature Dependence of Poisson's Ratios, σ_{1j}

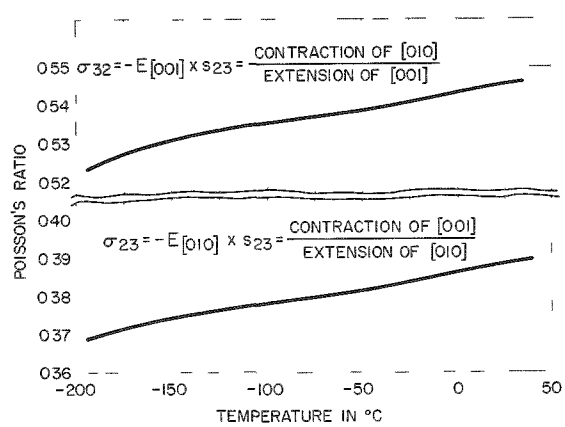

Figure 42

Temperature Dependence of Poisson's Ratio, σ_{1j}

The smooth, almost linear curve of c_{22}, versus temperature above 200°C is interesting in view of the negative temperature coefficient of thermal expansion in the [010] direction in this temperature range. It is planned to extend the work to these temperatures on equipment currently being designed and built at ANL.

3. Theoretical Studies on the Temperature Dependence of Elastic Moduli (D. Van Ostenburg)

The temperature dependence of the stiffness modulus c_{11} in orthorhombic α uranium, which goes through a maximum near -20°C and then decreases with decreasing temperatures, is in contradiction to

theories based upon an anharmonic approximation for nonmagnetic solids, which predict a temperature dependence in which the stiffness increases with decreasing temperatures.[39,40] It is conceivable that there is a magnetic transition occurring at low temperatures in uranium which causes a lowering of the modulus. To this end, we intend to re-examine the data on magnetic susceptibilities at low temperatures and, if necessary, to acquire more accurate data. Also, upon completion of experimental apparatus at Argonne, it is proposed to measure the temperature dependence of the moduli as a function of magnetic field strength and as a function of the direction of the field with respect to the crystallographic axes. The fact that the alleged magnetic dependence occurs only for c_{11} seems to indicate a strong magnetic anisotropy.

We have also begun a study of the material in the harmonic approximation based upon the model of a solid composed of atoms coupled together by springs. This approach will enable a correlation between the elastic parameters and the force constants of the atoms, which should eventually lead to a calculation of the lattice vibration spectrum and comparison with specific heat data. The procedure follows rather closely that of DeLaunay[41] and Smith.[42] Alpha uranium, which has orthorhombic symmetry, can be constructed from two interpenetrating lattices which are both side-centered orthorhombic. Figure 43 shows the atomic arrangement in which the solid circles represent atoms of lattice I and open circles those of lattice II. The neighbors of lattice I are denoted by the unprimed letters, those of lattice II by primed letters. The atomic spacings of representative atoms are

$$A - B = 2.75\ \text{Å},\ A - C = 2.85\ \text{Å}$$
$$A - D = 3.25\ \text{Å},\ A - E = 3.34\ \text{Å}$$

If we let $\bar{e}_1$, $\bar{e}_2$, $\bar{e}_3$ denote unit vectors along the x, y, z axes, the atoms of lattice I are given by

$$\vec{r}_I = \left(\frac{n_1 + n_2}{2}\right) a\ \vec{e}_1 + \left(\frac{n_2 - n_1}{2}\right) b\ \vec{e}_2 + n_3\ c\ \vec{e}_3 \quad , \qquad (1)$$

---

[39] W. Ludwig, J. Phys. Chem. Solid 4 283 (1958).

[40] E. A. Stern, Phys. Rev. 111 786 (1958).

[41] J. DeLaunay, Solids State Phys. 2 219 (1956).

[42] H. M. J. Smith, Trans. Roy. Soc. A241 105 (1949).

Figure 43

The black circles represent atoms of lattice I, the white circles atoms of lattice II. The large black and white circles show the origins of the two lattices. Unprimed letters designate nearest, next nearest neighbors, etc., of lattice I, while primed letters mark those of lattice II. The remaining half of the neighbors indicated by C, C', D, D', E, E', are obtained by reflection in the y-z plane.

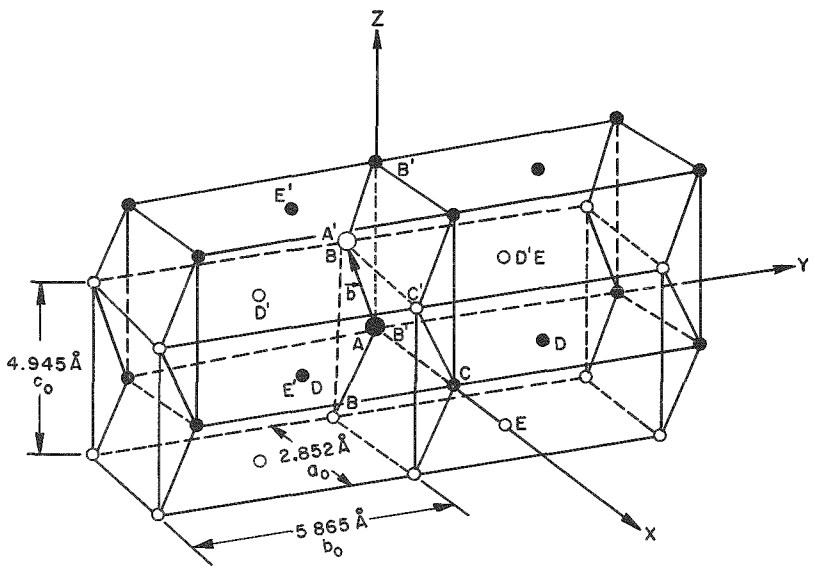

and those of lattice II by

$$\vec{r}_{II} = \left(\frac{n_1 + n_2}{2}\right) a\,\vec{e}_1 + \left[\frac{n_2 - n_1}{2} - 2y\right] b\,\vec{e}_2 + \left(n_3 + \frac{1}{2}\right) c\,\vec{e}_3. \qquad (2)$$

where the basis vector is

$$\vec{b}_1 = -2y\,b\,\vec{e}_2 + \frac{1}{2}c\,\vec{e}_3 \quad .$$

In these equations the n_i (i = 1, 2, 3) are integers, a, b and c are the unit cell dimensions, and y = 0.105.

In the model currently assumed, nearest neighbors interact with non-central forces while 2nd, 3rd and 4th nearest neighbors interact with central forces. We let α_1' represent the angular force constant associated with the nearest neighbors, and α_1, α_2, α_3, and α_4 the central force constants associated with the first through fourth nearest neighbors, respectively. The use of these force constants with the interpenetrating lattice depicted in Figure 43 enables us to write down the equations of motion. They are solved by assuming the waves of the form

A exp i $(\omega t + 2\ \vec{k} \cdot \vec{r}_I)$ and B exp i $(\omega t + 2\ \vec{k} \cdot \vec{r}_{II})$ pass through lattice I and II, respectively. The result for both lattices is that the eigenfrequencies are given as the solution of the following 6 x 6 determinant:

$$\begin{vmatrix} a_{11}-x & a_{12} & 0 & a_{14} & a_{15} & a_{16} \\ a_{12} & a_{22}-x & 0 & a_{15} & a_{25} & a_{26} \\ 0 & 0 & a_{33}-x & a_{16} & a_{26} & a_{36} \\ a_{14}^* & a_{15}^* & a_{16}^* & a_{11}-x & a_{12} & 0 \\ a_{15}^* & a_{25}^* & a_{26}^* & a_{12} & a_{22}-x & 0 \\ a_{16}^* & a_{26}^* & a_{36}^* & 0 & 0 & a_{33}-x \end{vmatrix} = 0 \quad , \quad (3)$$

where a_{ij}^* is the complex conjugate of a_{ij} and $x = \omega^2 M$. The elements have the values

$$a_{11} = 2\alpha_1' + 4\alpha_2 S_a^2 + 4\alpha_3(0.438)^2\,(1 - C_a C_b) + 4\alpha_4(0.425)^2$$

$$a_{22} = 2\alpha_1' - 2(\alpha_1' - \alpha_1)(0.447)^2 + 4\alpha_3(0.899)^2(1 - C_a C_b) + 4\alpha_4(0.509)^2$$

$$a_{33} = 2\alpha_1' - 2(\alpha_1' - \alpha_1)(0.895)^2 + 4\alpha_4(0.739)^2$$

$$a_{12} = 4\alpha_3(0.438)(0.899)\ S_a S_b$$

$$a_{14} = -\left[2\alpha_1' C_c + 4\alpha_4(0.425)^2 e^{-i\pi b k_2}\ C_a C_c\right] e^{4\pi i b y k_2}$$

$$a_{15} = 4i\alpha_4(0.425)(0.509) e^{-i\pi b k_2}\ S_a C_c e^{4\pi i b y k_2}$$

$$a_{16} = 4\alpha_4(0.425)(0.739) e^{-i\pi b k_2}\ S_a S_c e^{4\pi i b y k_2}$$

$$a_{25} = -\left[2\alpha_1' C_c - 2(\alpha_1' - \alpha_1)(0.447)^2\ C_c + 4\alpha_4(0.509)^2 e^{-i\pi b k_2}\ C_a C_c\right] e^{4\pi i b y k_2}$$

$$a_{26} = \left[2i(\alpha_1' - \alpha_1)(0.447)(0.895) S_c + 4i\alpha_4(0.509)(0.739) e^{-i\pi b k_2}\right] e^{4\pi i b y k_2}$$

$$a_{36} = -\left[2\alpha_1' C_c - 2(\alpha_1' - \alpha_1)(0.895)^2 C_c + 4\alpha_4(0.739)^2 C_a C_c e^{-i\pi b k_2}\right] e^{4\pi i b y k_2} \quad ,$$

where $S_a = \sin\pi a k_1$; $S_b = \sin\pi b k_2$; $S_c = \sin\pi c k_3$;

$C_a = \cos\pi a k_1$; $C_b = \cos\pi b k_2$; $C_c = \cos\pi c k_3$.

In the limit of infinite wave length ($\vec{k} = 0$) we obtain from (3) three roots $\nu^2 = 0$ (acoustic waves) and three roots of optical frequency

$$\nu = \frac{1}{\pi}\sqrt{\frac{\alpha_1' + 2\alpha_4(0.425)^2}{M}}$$

$$\nu = \frac{1}{\pi}\sqrt{\frac{\alpha_1' - (\alpha_1' - \alpha_1)(0.447)^2 + 2\alpha_4(0.509)^2}{M}} \qquad (4)$$

$$\nu = \frac{1}{\pi}\sqrt{\frac{\alpha_1' - (\alpha_1' - \alpha_1)(0.895)^2 + 2\alpha_4(0.739)^2}{M}}$$

where M is the mass of the uranium atom. These frequencies are those at which the two single Bravais lattices vibrate with respect to each other when each itself is rigid.

To obtain the elastic moduli in terms of the force constant we take the double limit $\vec{k} \to 0$, $\nu \to 0$ in equation (3). The first of these selects the long wave lengths while the second selects the low frequencies and hence the acoustical frequencies. Comparison is then made with a 3 x 3 secular determinant for ω^2 which contains the elastic moduli c_{ij} and the propagation vector $\vec{k}$. The values computed thus far are

$$c_{11} = \frac{2a}{bc}\left[2\alpha_2 + (0.438)^2\alpha_3 + (0.425)^2\alpha_4\right]$$

$$c_{22} = \frac{2b}{ac}\left\{(0.899)\alpha_3 + (0.509)^2\alpha_4\left[\frac{\alpha_1' - (0.447)^2(\alpha_1' - \alpha_1)}{\alpha_1' - (0.447)^2(\alpha_1' - \alpha_1) + 2\alpha_4(0.509)^2}\right]\right\}$$

$$c_{33} = \frac{c}{ab}\left[\alpha_1' - (0.899)^2(\alpha_1' - \alpha_1) + 2\,(.739)^2\alpha_4\right] \quad .$$

4. Interactions of Interstitial Solute Atoms with Dislocations (D. G. Westlake)

A program has been initiated to study the effects of solute hydrogen on the deformation modes of zirconium. Rapperport and Hartley[43] have found only one slip system in pure zirconium, the $(10\bar{1}0)$ $[\bar{1}2\bar{1}0]$. It seems quite likely that this slip is produced, not by a unit dislocation, but by two partial dislocations:

$$1/3\,[\bar{1}2\bar{1}0] \rightarrow 1/6\,[\bar{1}2\bar{1}3] + 1/6\,[\bar{1}2\bar{1}3] \quad .$$

Sidhu, Heaton, and Zauberis[44] have shown that hydrogen occupies the tetrahedral interstices of hafnium, titanium and zirconium. Hydrogen in these positions would not seem to offer great hindrance to the motion of the partial

[43] E. J. Rapperport and C. S. Hartley, Deformation Modes of Zirconium at 77, 300, 575, and 1075°K, NMI-1221 (1959).

[44] S. S. Sidhu, LeRoy Heaton and D. D. Zauberis, Neutron Diffraction Studies of Hafnium-Hydrogen and Titanium-Hydrogen Systems, ANL-5501 (1956).

dislocations; hence solute hydrogen atoms would not be expected to change the mode of deformation by slip. However, sufficient quantities of hydrogen concentrated between the partial dislocations might make measurable changes in the critical resolved shear stress of the slip system.

Twinning has been observed on $\{10\bar{1}2\}$, $\{11\bar{2}1\}$, $\{11\bar{2}2\}$ planes, and infrequently on $\{11\bar{2}3\}$ planes.[43] The first three types of planes are the habit planes of zirconium hydride.[45] This may indicate that the hydride is nucleated at concentrations of hydrogen in faulted material between partial dislocations lying in the twin planes. Attention will therefore be directed toward evaluating the atom movements and the combinations of partial dislocations [according to Cottrell and Bilby's mechanism of twinning][46] which would produce the observed twinning. No information is available on the effect of hydrogen on any of the twinning modes.

There is also the possibility that at low temperatures, in the presence of hydrogen, twinning on the aforementioned systems would be suppressed to the point that other twin systems could operate. Should slip dislocations be unable to cross these new twin boundaries, embrittlement would result. Biggs and Pratt[47] have observed that twinning always preceded cleavage failure in iron, and Birnbaum's[48] work supports their theory that slip dislocations were unable to cross the particular twin boundaries observed. In zirconium, this does not seem the most likely mechanism of hydrogen embrittlement, since it occurs only when precipitated hydride is visible metallographically.[49] It is more likely that dislocation pile-ups against the hydride initiate the brittle failure.

To date, an apparatus has been designed for charging metal specimens with hydrogen and for hydrogen analysis. Single crystals of zirconium will be used in these studies. The first objective is to measure the critical shear stresses for the slip and twin systems between 77 and 300°K as a function of hydrogen content.

[45] S. W. Kunz and A. E. Bibb, Habit Plane for Hydride Precipitate in Zirconium and Uranium-Zirconium, KAPL-2000-5, pp. 113-114 (1959).

[46] A. H. Cottrell and B. A. Bilby, A Mechanism for the Growth of Deformation Twins in Crystals, Phil. Mag. 42 573 (1951).

[47] W. D. Biggs and P. L. Pratt, The Deformation and Fracture of Alpha-Iron at Low Temperatures, Acta Met. 6 694 (1958).

[48] H. K. Birnbaum, On the Conditions Governing the Brittle Fracture of Iron Single Crystals, Acta Met. 7 516 (1959).

[49] R. W. Dayton, A. D. Schwope, G. T. Muehlenkamp, H. A. Saller, R. F. Dickerson, C. M. Schwartz, and M. W. Mallett, Hydrogen Embrittlement of Zirconium, BMI-767 (1952).

G. Corrosion Research

1. Polarization in Distilled Water (F. E. DeBoer and J. E. Draley)

Apparatus: Determination of the effect of applied current on the solution potential of a metal corroding in distilled water is a difficult instrumentation problem. In prior years these measurements have been made without serious error, except for the high cathodic current part of the curve. It is now believed that this weakness in the apparatus has been rectified, and that it will now be possible to determine reliable curves on a routine basis.

Corrosion in Boiling Water: In order to provide data for correlation with polarization behavior, the corrosion of six metals has been studied: aluminum, nickel, tin, magnesium, tantalum, and chromium. It is interesting to observe the difference in corrosion behavior, shown in Figure 44, between two kinds of "high purity" aluminum of the following compositions (in parts per million):

	Fe	Cu	Si	Mg
Kaiser	10	30	31	12
Swiss	7	4	12	1

This trend in corrosion behavior (above a certain test temperature) as a function of purity is typical for aluminum. The most important impurities have not definitely been determined.

Figure 44

High Purity Aluminum in 100°C Water

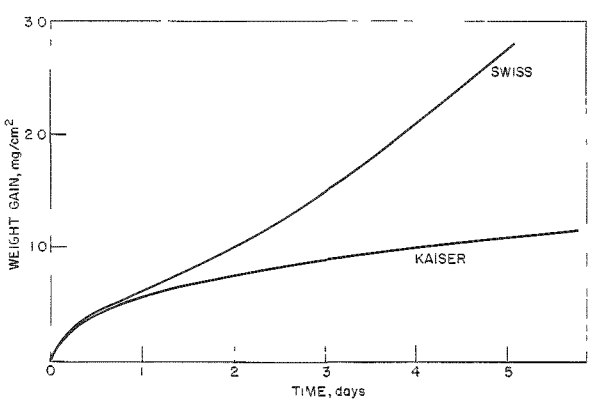

Analysis of Impurities in Aluminum: Analyses such as those above require refined procedures. There was no suitable procedure available for magnesium. A method of concentrating it in the metal by fractional distillation to facilitate analysis has been worked out. The method has been published in an article in Nature 184 54 (1959).

2. Corrosion Mechanism of Zirconium (R. D. Misch and J. E. Draley)

There has been little progress in the effort to find an acceptable technique for measuring the electrical resistance of the growing oxide film on zirconium and its alloys. The problem is still to obtain reproducible values for known contact areas.

Other measurements are being used to examine the corrosion mechanism of zirconium from two general aspects. The first approach is to identify the reasons why zirconium has higher corrosion rates in water and steam than in dry oxygen. This indicates that hydrogen is able to accelerate scaling by some unidentified means. The second approach is based on the phenomenon of valency control of defects in ionic solids. The use of aliovalent additives (those which differ in valency from the cations of the host lattice) has served to explain many impurity effects on electrical conductivity and other properties of ionic solids.

The application of these theories to zirconium corrosion has required a re-evaluation of some of these concepts for the case of scale growth. Based on these considerations, a number of new alloys have been prepared to vary the oxide-defect structure while avoiding the complication of introducing effective cathodes. These alloys contain combinations of lower and higher valent additives designed to stabilize the ZrO_2 structure by eliminating both anion vacancies and conductivity electrons.

Hydrogen Mechanisms: Hydrogen could have several effects in the metal or oxide, depending on diffusion and recombination. An extreme case was found in zirconium crystal bar corroded in 540°C, 600 psi steam for 162 hours. The residual metal was brittle and contained approximately 2 w/o H_2. Consequently, its composition was close to that of ZrH_2. Many other alloys tested in steam also embrittled from the pickup of hydrogen, but only if corrosion was severe. Thus far, severe corrosion in steam without embrittlement has not been observed. A wider variety of corroded specimens will be analyzed to determine whether hydrogen pickup always accompanies a high corrosion rate.

The oxide film on zirconium has the properties of an insulator at room temperature, and this layer would not be expected to act as an efficient cathode at higher temperatures. As a result, the presence of additional cathodes could increase or decrease the corrosion rate. The latter effect would support the theory of film damage from cathodic hydrogen.

These possibilities were tested in three ways. First, inert cathodes were incorporated into zirconium by sintering mixtures of foreign oxides and zirconium hydride. Three oxides of particular interest were TiO_2, Nb_2O_5 and Ta_2O_5 for the reason that fused buttons of these oxides remained good electronic conductors after exposure to water at 350°C. The appearance of these oxides did not change during water exposure. Mixtures of zirconium hydride and oxide powders were pressed into $\frac{1}{2}$-in. diameter pellets at 75 tons per square inch and sintered in vacuum at 1200°C for 2 hours. Slow heating was necessary to permit the hydrogen to be pumped off. The zirconium controls prepared in this way had inferior corrosion resistance as compared to zirconium arc melted from Grade I

crystal bar. White oxide appeared on all the specimens within several days in water at 350°C. Four compositions retained black films for longer periods. These contained platinum, molybdenum, Nb_2O_5 and Ta_2O_5. Thus an improvement was obtainable, but it fell far short of a good alloy such as Zircaloy-2. It was concluded that supplementary cathodes were beneficial when the matrix zirconium had a relatively high corrosion rate.

This conclusion was reinforced by experiments based on comparisons between water and $CuSO_4$ solutions. By using $CuSO_4$, the metal cation should be reduced instead of hydrogen. In the absence of discrete microcathodes the copper would be reduced on the oxide surface. If platinum is present in the metal, it should form preferential cathodes. Comparisons were made using pure zirconium, zirconium containing 0.5 w/o Ti (to increase the corrosion rate), and zirconium plus 0.5 w/o Ti, 0.1 w/o Pt. Enough copper sulfate was used to insure saturation at room temperature (5 g $CuSO_4 \cdot 5H_2O$/80 ml solution). The average weight loss of zirconium was determined after removing the brittle oxide by bending the metal disc. The results for 16-hour exposures at 350°C were as follows:

Alloy Composition	Medium	Average Weight Loss, mg/dm^2
0.5 w/o Ti	H_2O	2610
0.5 w/o Ti + 0.1 w/o Pt	H_2O	2025
0.5 w/o Ti	$CuSO_4$ Solution	1330
0.5 w/o Ti + 0.1 w/o Pt	$CuSO_4$ Solution	970

These results were a clear indication that hydrogen was influencing the corrosion reaction. On the other hand, pure zirconium, whose film was too thin to be removed by flaking, showed no difference in weight gain (approximately 5 mg/dm^2) with the addition of $CuSO_4$.

On the basis of this evidence, it is proposed that cathodic hydrogen requires the presence of defects in the ZrO_2 film (such as produced by the presence of titanium) before its deleterious action becomes pronounced. It is possible that hydrogen in the form of protons associates with defects in the ZrO_2.

Mechanisms Based on Control of Defects: Substitutional valency control as a means of controlling ZrO_2 formation on zirconium has so far not received detailed consideration. The reason for this is that the application of the Hauffe rules[50] has not explained the corrosion results obtained with binary alloys of zirconium. For example, to explain

[50] K. Hauffe, Reaktionen in und an Festen Stoffen, Springer-Verlag, Berlin (1955).

why iron and nickel are beneficial it is necessary to assume that the ions of these metals are present on interstitial sites in ZrO_2. Additives such as niobium, molybdenum and tungsten, which might eliminate anion vacancies by virtue of forming cations with valencies greater than +4, either have no effect or cause an increase of corrosion rate.

One part of the present program is to examine the valency control mechanism more closely, with due regard for complicating factors. Among these are ion size, ionization potential, and types of ionic reactions to be expected. It is shown below that the usual Hauffe rule for diminishing vacancies in ZrO_2 (anion vacancies) may not apply for an additive such as tungsten. This complication has not been pointed out previously.

The effect of an additive is usually considered in terms of the result when the respective oxides are combined. Thus, a minor constituent (e.g., NiO or WO_3) will dissolve in ZrO_2 and change the defect structure in accordance with the valence of the added cation. In the case of corrosion-resistant alloys, the additive is present in the alloy and is incorporated into the growing scale. It is unlikely that the additive will form its own oxide if it is present in solid solution or as an intermetallic compound. Therefore, the formation of the oxide layer may not be analogous to the case when the pure oxides combine. Another complicating factor is that the equilibria in the oxide will depend on the presence of oxygen. In the ZrO_2 case an equilibrium condition will not exist at the metal-oxide interface where oxygen is lacking.

Another possibility which must be considered is that oppositely charged impurity centers, such as nickel ions and tungsten ions on zirconium ion sites, may associate to form stable complexes. This gives rise to the possibility that certain combinations of additives may control the defect structure of ZrO_2 more effectively than any single additive.

This hypothesis has been used as the basis for preparing a number of alloys with combinations of elements which should not form cathodes. The elements selected for study consisted of scandium and yttrium (normal valences +3) in combination with other elements which were potentially capable of forming +5 and +6 ions. The binary alloys of scandium and yttrium with zirconium have poor corrosion resistance, but this was not considered sufficient reason to avoid these elements which have favorable ionic sizes for replacing Zr^{+4} in the ZrO_2 lattice. The assumption was made that the effect of additives in combination cannot be judged a priori from the effect of single additives.

By analogy with NiW, a 3-5 valence combination should produce an electrically neutral lattice. On the chance that all the potentially higher valent additives (As, Bi, Cr, Mo, Mn, Nb, Pb, Sb, Ta, W) might not form higher valent ions, the ratios of +3 to +5 or +6 elements were chosen as 1:1, 1:2 and 1:3. A series of alloys were made up containing 0.5 w/o of additives, balance zirconium. Alloys were made by arc melting, annealing, and

furnace cooling or quenching. They were then screened by exposure to water at 350°C and later to steam at 540°C, 600 psi. Thus far, two combinations have shown sufficient promise to warrant more detailed study. These were 0.1 w/o Sc, 0.4 w/o Mo, and 0.5 w/o Y, 1.0 w/o Nb. These compositions are highly specific; for example, analogous yttrium alloys containing tantalum or molybdenum have low corrosion resistance by comparison.

Further work on these alloys will involve comparison with alloys containing nickel and copper, for which a hydrogen mechanism may be operative.

3. The Corrosion of 1100 Aluminum in Water (S. Mori and J. E. Draley)

Effects of Metal Impurities: Our standard supply of 1100 aluminum sheet contains 0.47 w/o Fe, 0.12 w/o Cu and 0.13 w/o Si. To examine their relative influences on some aspects of the corrosion of 1100 aluminum, binary alloys were made of 99.99% Al with the appropriate amounts of each of these impurities. After 30-minute corrosion in air-saturated water at 50°C, the iron alloy had acquired a brown discoloration, apparently identical to that of 1100 aluminum. The copper alloy developed a lighter, different-hued discoloration; the silicon alloy and high-purity metal showed no significant discoloration.

After an additional exposure of 22 hours in oxygen-saturated water at 70°C, the same specimens were examined for weight gain (amount of corrosion) and the nature of the microscopic pitting. The observations were as follows:

Composition	Weight Gain (mg)	Surface Pit Description
1100 Al	5.97	Numerous small shallow pits
Kaiser H.P. Al	11.85	Some large and deep pits
Kaiser H.P. Al-0.47 w/o Fe	5.71	Numerous small shallow pits
Kaiser H.P. Al-0.12 w/o Cu	7.50	Few large deep pits
Kaiser H.P. Al-0.13 w/o Si	8.60	Few large deep pits

The results again indicate that the iron alloy corrodes very much as does 1100 Al, and that the others do not.

Kinetics: At 70°C, the amount of corrosion varied as the logarithm of time for about 7 hours. Subsequently, the rate increased and finally apparently decreased continuously with time. The final stage began at less than one day's corrosion, although it is by no means certain that the same kinetic equation is in force from that time on.

During the year, two tests were run in oxygen-saturated distilled water, using the high-sensitivity "thickness gauge" to judge the amount of corrosion for each specimen as a function of time. Material was extruded, machined and polished, then etched. In the first test, using unannealed specimens, for 60 days, reproducible, smooth curves were obtained. These could be fitted by four rate equations, none of which is commonly encountered in corrosion studies. In two of these equations, the rate of the reaction is proportional to $(a - L)^2$, where a is a constant, in the form of an asymptotic limit to the amount of corrosion, L.

The specimens for the second test (90 days) were annealed before use. In this case the curve was different, and could be fitted by an equation in which the rate was proportional to $(a - L)^3$.

At the present time the reaction kinetics seem to depend on the state of heat treatment of the specimens. Deriving corrosion mechanisms on the basis of kinetics will probably require some choice between rate equations which so far fit the data equally well.

Corrosion in D_2O: The results of corrosion tests of 1100 Al in boiling H_2O and D_2O may be summarized as follows: except for the initial period, when more corrosion occurred in the boiling H_2O than in boiling D_2O, the corrosion curves for the two systems were the same (Figure 45).

Figure 45

Corrosion of 1100 Aluminum in Boiling D_2O and H_2O

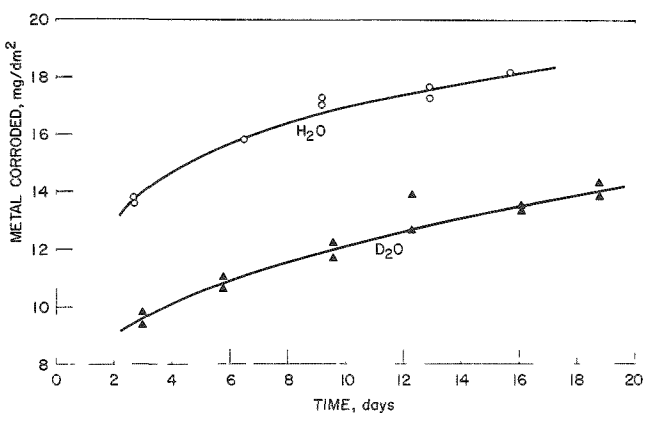

Corrosion Product Analysis: X-ray and electron diffraction analysis of the corrosion product formed in water at 50 and 70°C showed that the first clearly crystalline product had the boehmite (AlOOH) structure. After longer exposures, and perhaps corresponding to the time when the rate increased (~7 hours at 70°C), bayerite [$Al(OH)_3$] was found. More careful studies should make it possible to establish the relationship between kinetics and structure of the product.

Chemical analyses should also be helpful. The water content of the corrosion product seems generally to be between that expected for boehmite and that expected for bayerite (8 days or longer exposure). We have not yet analyzed products from quite short exposure.

4. Corrosion-film Studies by Electron Microscopy and Diffraction (R. K. Hart)

Siemens Electron Microscope: The instrument was put into working condition last September. Since then it has worked satisfactorily except for one vacuum leak in the specimen air lock chamber. This was rectified by replacing a molded gasket. The efficiency of the instrument has been somewhat impaired by mechanical vibrations which originate in the fan loft across the balcony from the microscope room. It is proposed to live with this annoyance until we move into the new laboratories (Building 212). Electron optical studies to date have been confined to aluminum and zirconium and their alloys. No work on either uranium or uranium alloys has been undertaken to date, since a problem has arisen here in the difficulty of rolling these materials to a suitable thinness for subsequent electrothinning to obtain foils for direct transmission

Taper Sectioning of Aluminum Samples after Corrosion in Water: The outer surface of corroded samples was first coated with 3000 to 5000 Å of vacuum-evaporated gold, which served the dual purpose of a marker and helped retain the oxide in position during mechanical sectioning. Samples so far investigated were as follows:

a. "Super-purity" aluminum, 3 days in water at 70°C.

b. "Super-purity" aluminum, 24 hours in water at 100°C.

c. X8001 alloy, 6.7 days in water at 350°C.

d. A255 alloy, 6.7 days in water at 350°C.

The gold-coated specimens were mounted in Bakelite before sectioning at 5°54' (10:1 taper) with an end mill. Sectioned samples were mechanically polished and etched for 5 seconds in 1/2% HF.

All these experiments were of a preliminary nature, but were of interest, however, as they did shed some light on the nature of the metal/oxide interface and to a certain degree the structure of the oxide. In the case of A255 and X8001 alloys, attack on the metal surfaces was very uneven and led to considerable intergranular attack, as is shown in Figure 46. It should also be noticed in Figure 46 that "islands" of metal remain in the oxide. These metal "islands" are oxidized to varying degrees of completion as corrosion proceeds. No suitable electron micrographs have been obtained to date on taper-sectioned samples of these alloys.

With super-purity aluminum, metal "islands" were not nearly as evident, though they were not completely absent. One interesting electron micrograph, Figure 47, which shows the block structure of the corrosion product, was obtained. This type of structure is in agreement with electron diffraction patterns from corroded aluminum and experiments with drilled discs on which film growth was observed by direct transmission.

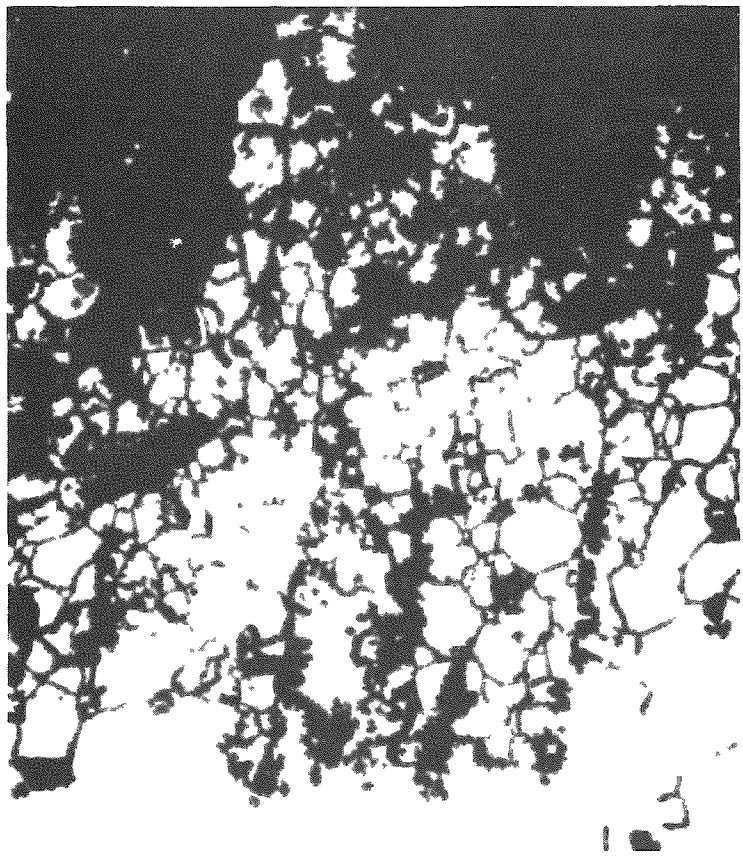

110,013 500-X

Figure 46

A255 Alloy Corroded in Water at 350°C for 6.7 Days.

Taper sectioned at 10:1. Mechanically polished and etched 10 seconds in 0.5% HF.

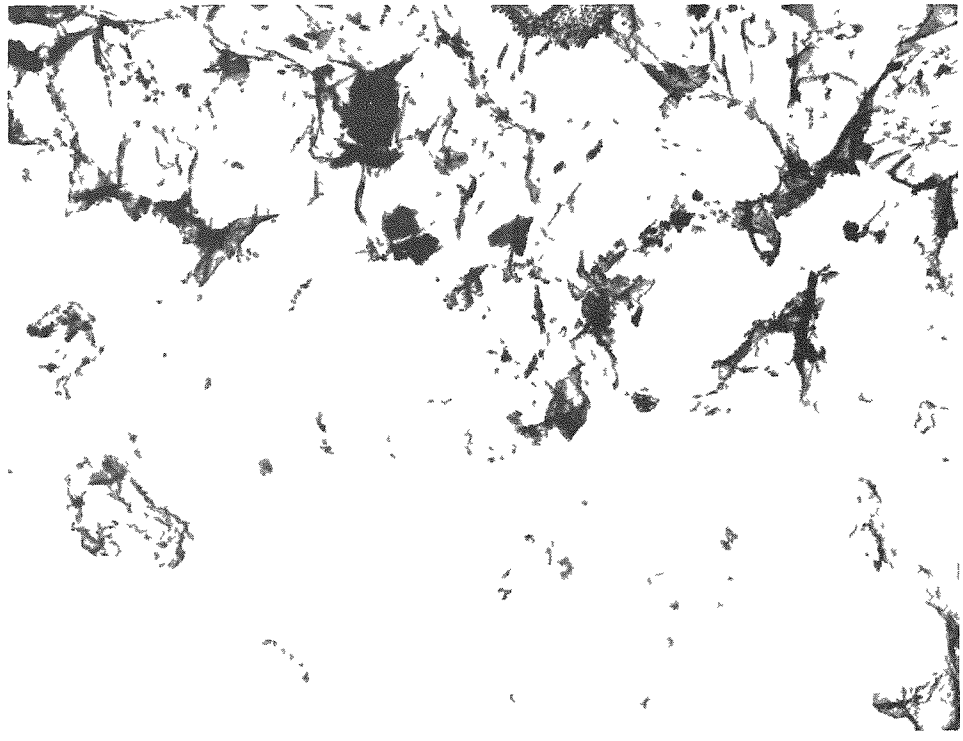

BIO-D978 3000-X

Figure 47

Super-pure Aluminum Corroded in Water at 70°C for 3 days.

Taper sectioned at 10:1. Mechanically polished and etched 10 seconds in 0.5% HF. Two-stage-shadowed carbon replica.

It is proposed to extend these investigations with taper-sectioned samples as soon as a cathodic etching apparatus is put into operation. References in the literature indicate that this method of surface preparation should be ideally suited for electron optical studies of metal/oxide surfaces. The point in favor of this method over chemical etching is that cathodic attack is nonpreferential.

Optical and Electron Optical Investigation of Particulate Material in Al-1 w/o Ni Alloys: The following materials were used in these experiments: (a) "Super-purity" aluminum, (b) X8001 alloy, (c) A255 alloy, and (d) A300 alloy. Super-purity aluminum was incorporated into this series for use as a control and also for completeness. The A300 alloy was also used as a control, and it was made from 99.999% aluminum to which was added 1 w/o "Spec Pure" nickel. It was used in the as-cast condition, whereas materials a, b and c above were in the form of $\frac{1}{8}$-in. thick rolled sheets.

Both mechanical polishing and electropolishing techniques were used to prepare the surfaces. In the case of electropolished surfaces, the initial preparation was to #6 diamond, using hypres oil as lubricant. Electropolishing was in a 1:9 perchloric/acetic bath operating at 15°C, and polishing was continued for twice the period of time required to remove the scratches left by #6 diamond paste. The polished surfaces were first viewed in the as-polished condition and then etched. The following etchants were used:

(a) 0.5% HF, 5 seconds and 10 seconds;
(b) 10% NaOH at 70% for 5 seconds;
(c) 20% H_2SO_4 at 70% for 30 seconds.

These etchants were selected from the literature as being suitable for etching of constituents in aluminum-nickel alloys. The etching characteristics of 0.5% HF are similar to the modified Keller's etch (0.5% HF, 1.5% HCl, 2.5% HNO_3), which is also commonly used for etching aluminum-nickel alloys.

Replicas for electron microscopic examination were prepared by the following three methods:

(a) two-stage-shadowed carbon replicas;
(b) stripped anodic oxide films;
(c) direct-stripped self-shadowed carbon replicas.

Results of these three methods were compared. As a result of this comparison all future replication will be standardized by method (a) which gave consistently good replicas of great clarity and had a resolution limit of less than 100 Å.

Both optical and electron micrographs showed that the electropolishing conditions used in these experiments brought out the surface structure of the second phase, namely, $NiAl_3$. It was also noted from electron micrographs that many areas were etched, the etch pits being either square or triangular in shape. This observation indicates that etching as well as electrolytic polishing take place, although some etching could have occurred between the time that the specimens were removed from the bath (with the current on) until washed in water. However, it seems highly unlikely that the amount of etching shown in the micrographs could have occurred in such a short interval of time.

With electropolished specimens, subsequent etching in 0.5% HF for either 5 or 10 seconds did not add appreciably to the relief of precipitates. Etch pits were again observed in this case. These could have remained from the original polishing. Mechanically polished specimens require etching to bring out the second phase - 10 seconds in 0.5% HF appears to be suitable.

With sodium hydroxide, etchant attack of the whole surface is rapid and a general roughening is quickly noticed. In the A255 alloy the second phase is clearly outlined, but detailed structure of the precipitates is generally lacking. The X8001 alloy is also severely attacked by sodium hydroxide and again no geometrical etch pits were observed. Precipitates were brought out in relief and a certain amount of detail could be seen within individual grains.

When etched in sulfuric acid, the particulate matter was almost completely obscured in electron micrographs by etch pits. These pits again were either triangular or square in shape. A certain amount of structure can be seen within precipitates, but is not nearly as evident as on either straight electropolished specimens or those that have been subsequently etched in 0.5% HF.

In both A255 and X8001 alloys there was in addition to the main precipitates, which were some 5 to 10 microns and larger in size, considerably smaller precipitates dispersed throughout the matrix. These particles in general were between 0.25 and 0.5 micron.

It was also noted that in the matrix there was a zone, surrounding the larger precipitates, which was devoid of smaller precipitates. This zone was of the order of 5 microns wide.

Another method that has been investigated for the study of particulate material in aluminum-nickel alloys is the direct electron microscopic examination of electrothinned foils. This method to date has led to only limited success. It has proved extremely difficult to thin these alloy foils down to some 800-1000 Å. This is probably due to preferential attack of the large second-phase precipitates which are eventually dissolved away

to leave holes in the foil. The thinning process is thus nonuniform. The most successful attempts to date are shown in Figures 48 and 49. Figure 48 is from super-pure aluminum and shows the general grain structure. Dislocations can be seen traversing a number of grains while other grains appear virtually free of imperfections. The broad dark bands which traverse individual grains are extinction contours caused by crystal planes along the bands being oriented at the right Bragg angle to give diffraction. The darkness of some grains is also due to diffraction effects. Parallel lines running adjacent to grain boundaries are due to low-angle grain boundaries.

Figure 49 shows a 0.3-micron diameter precipitate in the A255 alloy. It will be noticed that there is a distorted area in the matrix, almost entirely surrounding the precipitate. The strained area does not appear to extend very far into the metal film so the mismatch between precipitate and metal must be small. Dislocations appear to run to the boundary and pile up there rather than remain in the metal grains.

It is proposed to extend this investigation with thinned foils and, if suitable specimens can be obtained, to corrode them and have a direct observation of the process of oxide film growth in the immediate neighborhood of precipitates.

Direct Observation of Corrosion Films on Aluminum and Zirconium Alloys: Specimens for direct observation of corrosion film experiments were prepared by punching out $\frac{1}{8}$-in. diameter discs from either 0.002 or 0.005-in. thick metal foils. A centrally placed hole, 0.010-in. in diameter, was drilled and deburred. Finally, the specimens were electropolished in a 1:9 perchloric-acetic acid bath before corrosion. Corrosion conditions so far investigated were:

(a) A 255 alloy in water at 248°C for 4 minutes;

(b) A255 alloy in water at 350°C for 5 and 10 minutes;

(c) pure zirconium in water at 290°C for 2 and 20.5 hours;

(d) Zr-2 w/o Ti alloy in water at 290°C for 2 and 20.5 hours;

(e) Zr-8.4 w/o Ti alloy in water at 290°C for 2 and 20.5 hours.

Film growth in the A255 alloy corroded at 248°C for 4 minutes advanced outwards from the metal surface at a fairly uniform rate. Spaced out round the circumference of the hole were occasional outcrops where appreciable growth had taken place. Several such outcrops are shown in Figure 51. These outcrops consisted in general of clusters of thin oxide platelets, many of which showed internal structure. Diffraction patterns of these platelets corresponded to boehmite. Two-stage-shadowed carbon replicas taken close to the surface of the hole (see Figure 50) indicated that

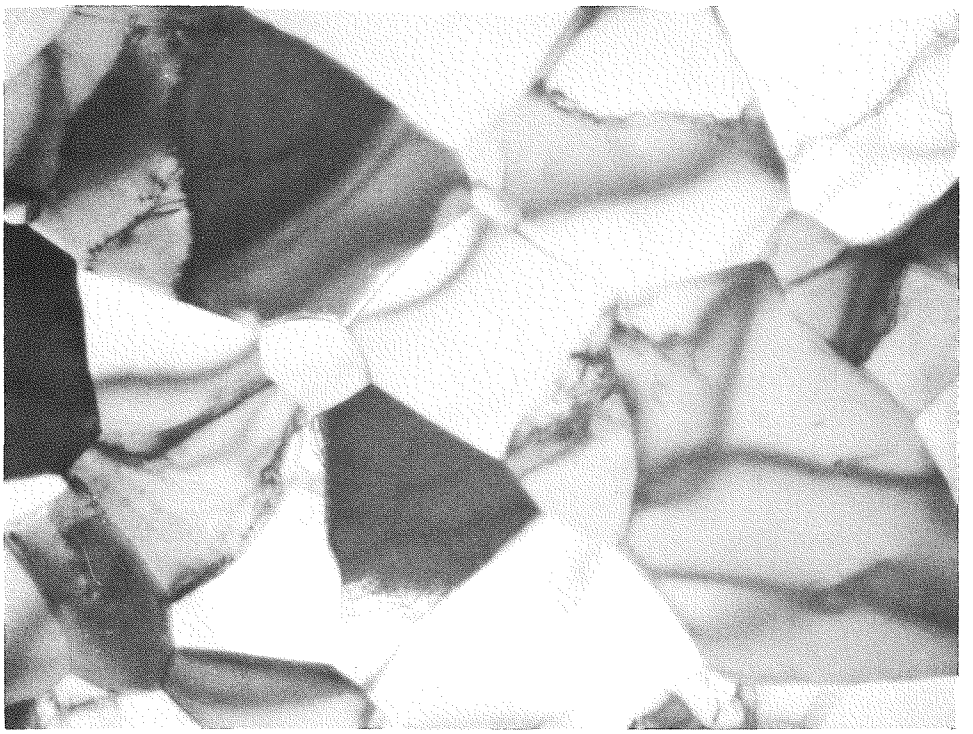

100,117 16,000-X

Figure 48

Super-pure Aluminum

Electrothinned in 1:9 perchloric acid-acetic acid from 0.002" sheet. Direct transmission.

Figure 49

A255 Alloy

Electrothinned in 1:9 perchloric acid-acetic acid from 0.005" sheet. Area showing precipitate. Direct transmission.

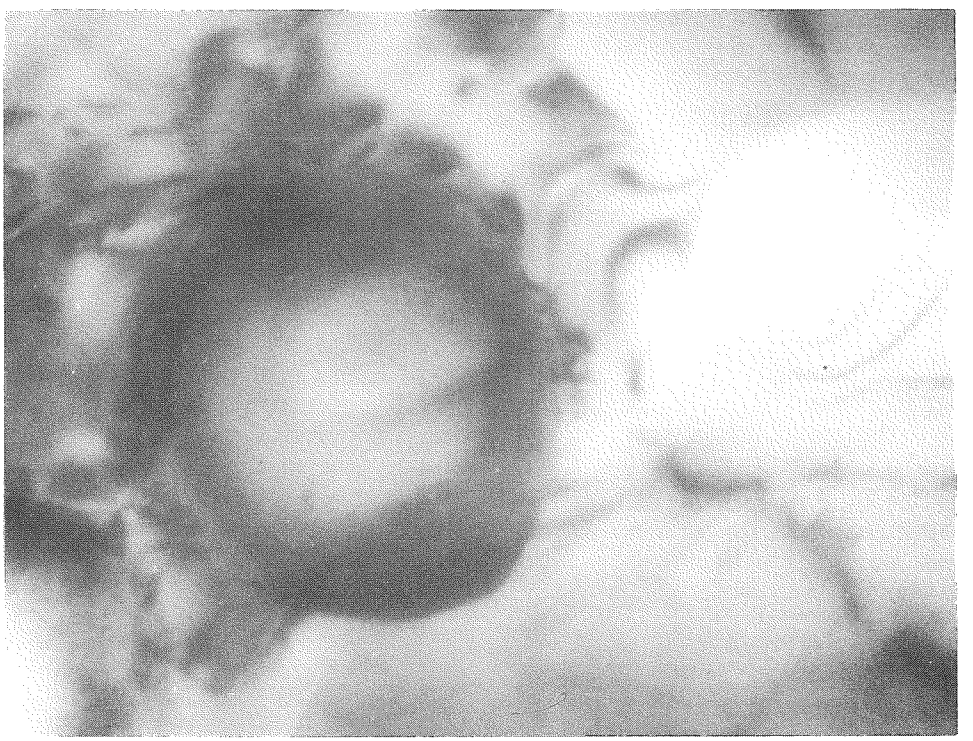

100,058 160,000-X

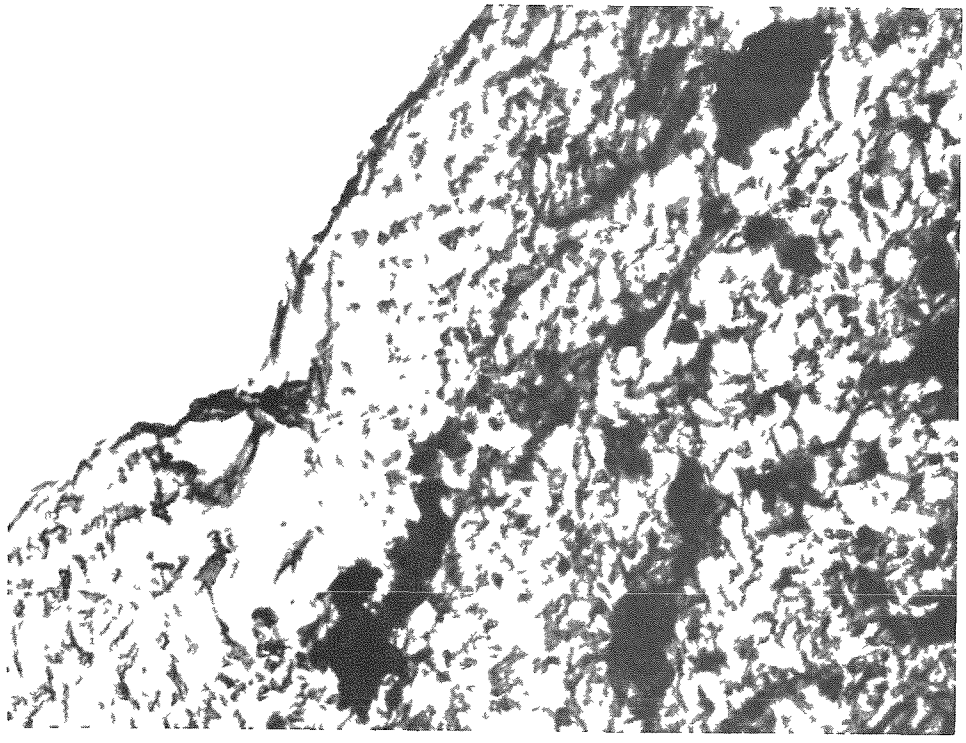

100,135 16,000-X

Figure 50

Drilled Disc of A255 Alloy Corroded in Water at 248°C for 4 Minutes.

Two-stage-shadowed carbon replica from near edge of hole.

Figure 51

Electron Shadowgraph from A255 Alloy Surface after Corrosion in Water at 248°C for 4 Minutes.

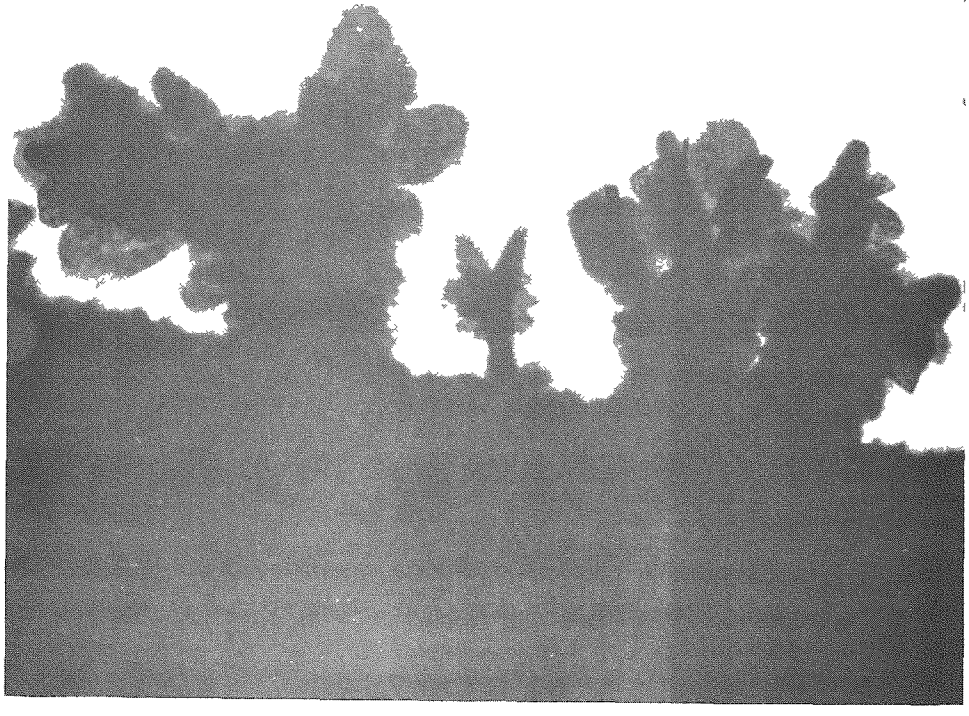

100,076 16,000-X

films consisted of overlapping platelets. Areas of more extended growth could also be seen (dark areas), but it is not possible to tie these up with the underlying metal structure. These areas, however, are probably similarly placed to the underlying structure as the growth clusters seen growing out from the surface of the hole.

The oxide growth pattern on the A255 alloy corroded at 350°C for 5 and 10 minutes appeared to be similar for both these times, but somewhat more advanced at the longer time. Selected area electron diffraction patterns showed a difference between the shorter and longer exposures. At 5 minutes only boehmite was detected, while at 10 minutes both boehmite and diaspore were present, although boehmite gave the stronger pattern of the two.

Over considerable areas the outward growth proceeded on a relatively even front and in these areas a predominance of triangular-shaped platelets were observed. The outward angle of these platelets varied between 63 and 80°. These relatively smooth areas were separated by chunky outcrops, similar to those seen in Figure 52. At and around these outcrops there was a preponderance of triangular-shaped platelets. Occasional spikes, which varied in length from 0.4 to 0.6 micron, were observed. Closer examination of these spikes indicated that they were probably platelets which were being viewed end on. In one case a spike was shown to consist of layers. Other platelets appeared monoclinic in shape and exhibited considerable structure, as shown in Figure 53. The loops and dark circles are extinction contours which appear to be caused by the sloping walls of cavities lying between layers in the platelet. Further evidence in this regard are the electron interference fringes (moiré patterns) which can be seen in the areas of diffraction contrast. The measured spacings of these fringes varied between 50 Å and 80 Å, which would correspond to a wedge angle from 0.047 to 0.029°. This is assuming that double diffraction occurs between planes of the same spacing but inclined toward each other. This type of electron interference will only occur in regions of the electron image showing diffraction contrast. This can be clearly seen in Figure 53. Also, in order for double diffraction to occur (i.e., moiré fringes), the crystals must be very thin so that the extension of the reciprocal lattice points are cut by the sphere of reflection.

The three zirconium and zirconium-titanium alloys that were corroded for 2 hours contained areas of considerable lateral extent which were relatively smooth. Outcrops of excessive growth occurred around the circumference, as shown in Figure 54. Pure zirconium outcrops, on the whole, were small and consisted mainly of clusters of oxide platelets. In the two alloys the outcrops became increasingly larger with increasing titanium concentration and became chunky, rather than consisting of clusters of platelets. Long, thin oxide "whiskers" (see Figure 57) were particularly noticeable on the two alloys, whereas on pure zirconium only the occasional short spike was observed. Figure 55 shows the occurrence of a platelet with spikes and chunky oxide. The chunky oxide is seen here breaking away

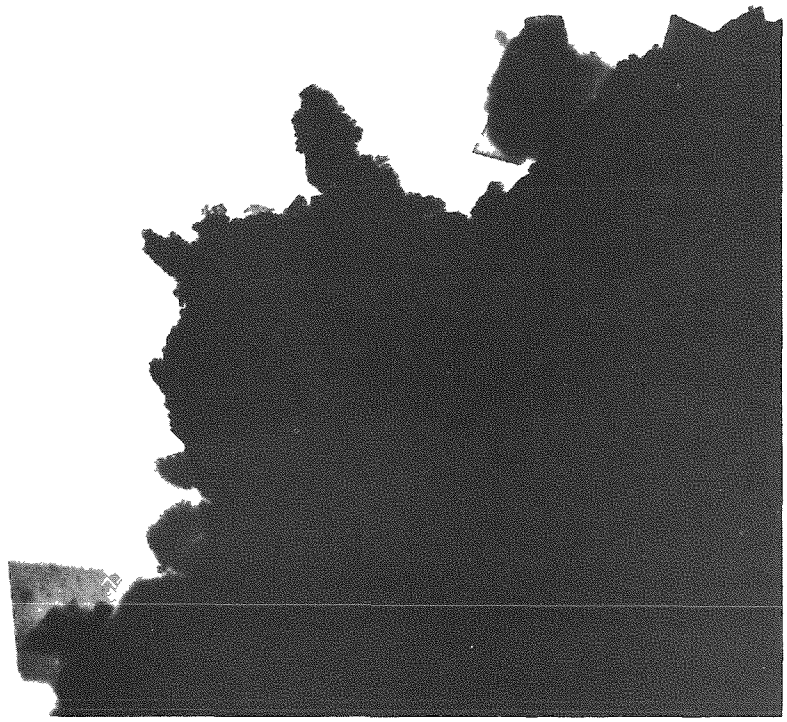

100,177 16,000-X

Figure 52

Electron Shadowgraph from A255 Alloy Surface after Corrosion in Water at 350°C for 10 Minutes.

Figure 53

Electron Shadowgraph from A255 Alloy Surface after Corrosion in Water at 350°C for 10 Minutes.

Large oxide platelet.

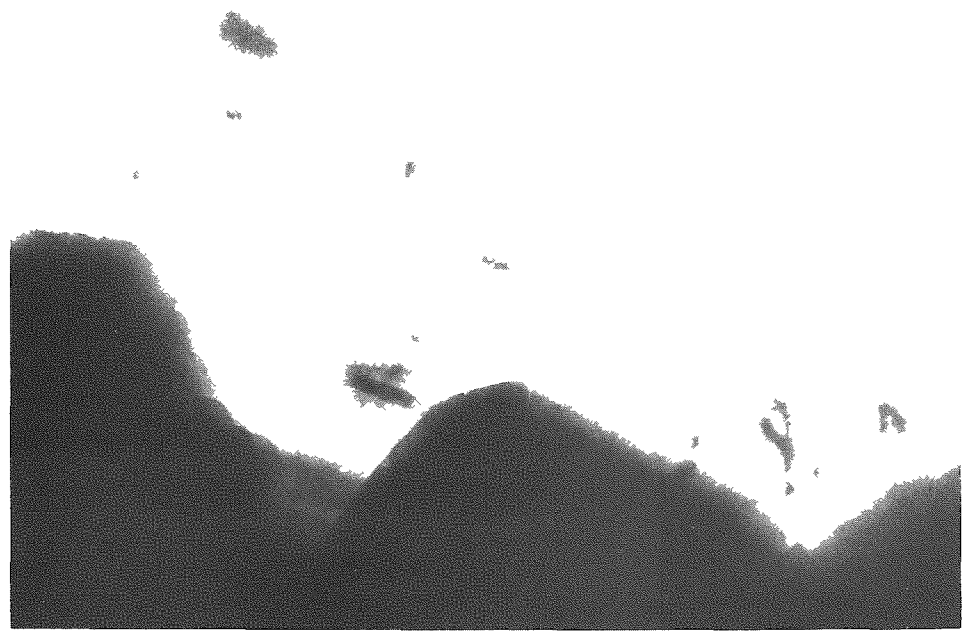

100,190 120,000-X

100,213 16,000-X

Figure 54

Electron Shadowgraph from Pure Zirconium Surface after Corrosion in Water at 290°C for 2 Hours.

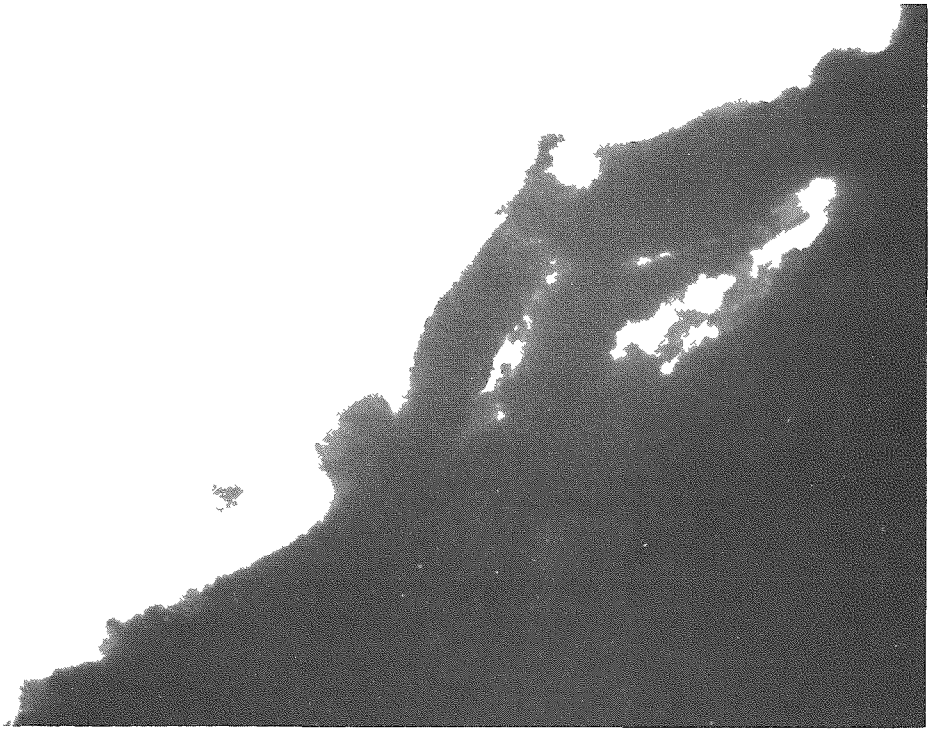

100,221 16,000-X

Figure 55

Various Forms of Oxide Growth on Zirconium-2 w/o Titanium Alloy after Corrosion in Water at 290°C for 2 Hours.

from the surface, presumably to remove the stress at that point. Figure 56 is another example of "spike" growth, only this time on the outward surface of a platelet similar to that shown in Figure 55. The "spikes" appear to nucleate from particulate matter some 60 to 120 Å in diameter.

Pure zirconium samples, corroded for 20.5 hours, had large areas of relatively smooth and uniform oxide growth which were broken by chunky outcrops. Neither thin platelets nor "whiskers" were observed under these conditions. The Zr-2 w/o Ti alloy was nearly all corroded away, while the Zr-8.4 w/o Ti alloy was completely converted to oxide and disintegrated.

Figure 56

Secondary Growth of Oxide Spikes from the Outer Edge of a Large Zirconium Oxide Platelet.

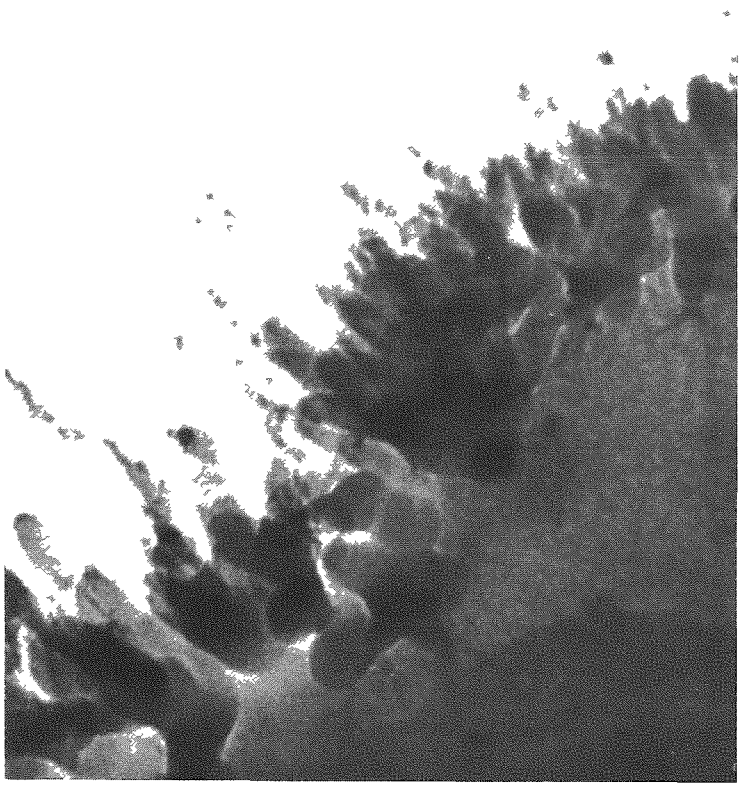

100,243 160,000-X

Figure 57

Oxide Whisker on the Surface of Zr-8.4 w/o Ti Alloy after Corrosion in Water at 290°C for 2 Hours.

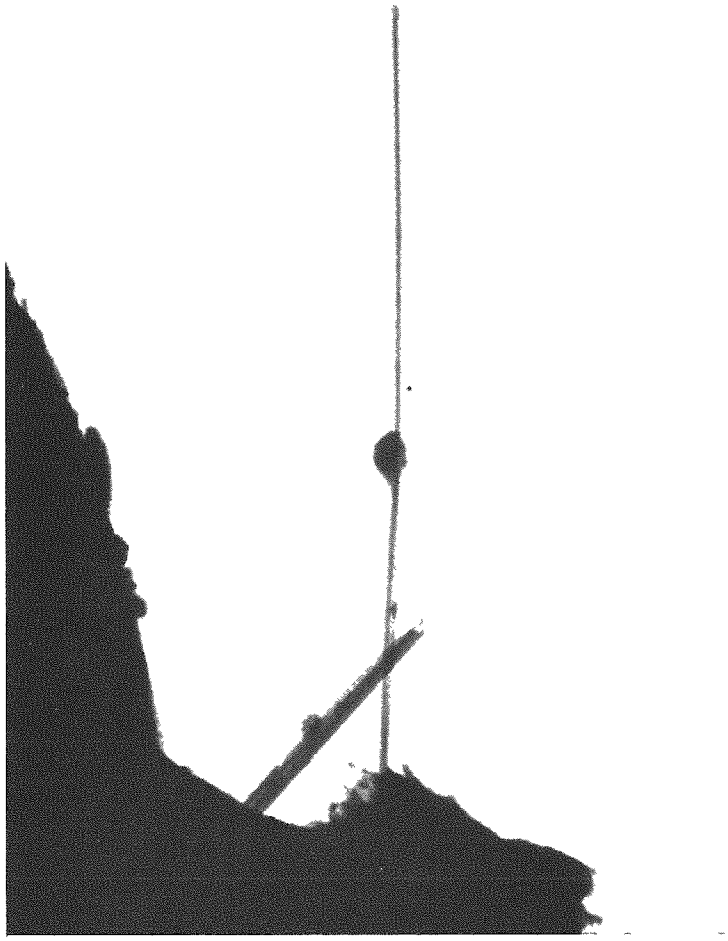

100,231 16,000-X

H. Irradiation Effects

1. Power Distribution in Uranium Specimens under Irradiation (F. R. Taraba and S. H. Paine)

Experimental work on this program has been completed during the past year and the results have been published in the following reports: "The Radial Distribution of Thermal Neutron Flux in Cylindrical Fuel Specimens during Neutron Irradiation," ANL-5872; and "The Longitudinal Distribution of Thermal Neutron Flux in Cylindrical Fuel Specimens during Irradiation," ANL-5945.

The above reports describe in detail neutron distributions in cylindrical fuel bodies during exposure in a thermal flux. The effects of the variable cylinder radius, a, and the macroscopic absorption cross section, Σ_{abs}, in the range $0 < \omega < 2.2$, where $\omega = a\Sigma_{abs}$, were studied. The experimentally determined radial distributions can be expressed by an empirical formula of the type

$$n(r,\omega) = \sum_{k=0}^{3} a_k(\omega) r^{2k}$$

for $r \leq a$, and $0 < \omega < 2.2$. The functions $a_k(\omega)$ are given by

$$a_k(\omega) = a^{-2k} \gamma^k \Big/ \sum_{j=0}^{3} \gamma^j \quad ,$$

where

$$\gamma = \omega/(-0.22894\,\omega^2 + 0.63812\omega + 1.2567) \quad .$$

The neutron flux is set equal to unity at the surface of the cylinder, i.e., $n(a,\omega) = 1$ for all ω.

The distribution of average cross-sectional flux along the length of a cylindrical fuel body may be expressed by an empirical equation of the type

$$\phi(z,T) = A(T) \exp[-B(T)z] + C(T), \ (0 \leq z \leq \lambda) \quad ,$$

where A(T), B(T) and C(T) are polynomials of the second degree, $T = 0.91\, a(\Sigma_{abs} + \Sigma_s)$ and $\lambda = 0.5935\, a^2 + 6.429\, a$. The symbol $\underline{a}$ denotes the radius of the specimen, and $\underline{z}$ is the axial distance from the end surface. Distribution is found to be a function of the material parameters

only, except when an absorbing body is near enough to perturb the flux at the cylinder end. In the latter case, a more complex equation was found to express the distribution, evaluation of which depends on knowledge of the Wilkins effect parameter.

2. Effect of Irradiation on Phase Transformations
(S. H. Paine and K. M. Myles)

Extended shutdown of the CP-5 reactor curtailed this investigation during the year to approximately 100 days of reactor operation. A total of seven uranium-molybdenum wire specimens have been used thus far to study the transformation behavior of the 5 and 8 w/o Mo alloys. The experimental method consists of holding the wire specimen at a chosen temperature within the reactor fuel lattice while making continuous measurements of resistance by means of a specially constructed ohmmeter.

The instrumental sensitivity required to detect slight changes in electrical resistance has been attained. However, it is evident from results to date that effects from a number of variables are being seen and that careful work is still needed before these may be separated. For instance, the magnitude of the resistance is quite sensitive to minor fluctuations of temperature, such as are produced by normal momentary changes in neutron flux. This does not mask long-term changes entirely, but seriously hinders observation of short-term phenomena, such as initial disorder effects in the specimen materials.

It is an encouragement to note that the long-term changes in resistivity are of a significant magnitude and show a consistent correlation with temperature and composition variables. For example, continuous exposures, one week long, have produced the increases shown in Table XVII.

TABLE XVII

Changes in Electrical Resistance Resulting from Irradiation of Uranium-Molybdenum Alloys in CP-5 for One Week

Composition (w/o Mo)	Average Temperature (°C)	Increase in Resistance (%)
5	475	10.9
5	525	11.3
8	475	7.0
8	635	9.1

Changes in resistance of the 8 w/o Mo alloy did not saturate during 2 weeks of exposure at the lower temperature, but in a similar period the 5 w/o Mo alloy at 525°C suffered a distinct drop in its rate of increase. These qualitative indications justify the present experimental arrangement and support the hope that with it dynamic changes may be studied in alloys of as low as 3 w/o Mo content.

3. Fission Gas Research (B. A. Loomis and S. H. Paine)

An immediate objective of the program of general fission gas research, begun last year, has been establishment of a correlation between swelling of fuel bodies and a number of the responsible factors, such as temperature, time, composition, rate of burnup, total burnup, and gas diffusion rate. The complex of sensitive variables is doubtless greater than this, but it was hoped that standardized materials, geometry, testing technique, and comparison with the swelling effects in unalloyed uranium could be used in separating major effects from minor.

As an initial step it was decided to irradiate specimens under appreciable restraint and at temperatures low enough to minimize gaseous diffusion. Postirradiation treatment will consist of an annealing program at elevated temperatures. Specimens presently being exposed in the MTR and which will be available for study in 1960 include unalloyed high-purity uranium and binary alloys of the same containing 10 a/o each of titanium, zirconium, niobium, and molybdenum. There are also specimens containing 2.5, 5.0, and 15 a/o molybdenum. Total atom burnups up to 1.0% are scheduled.

Apparatus for this investigation has been constructed and tested during the year as follows:

1. vacuum annealing furnace for use with irradiated specimens up to 1000°C temperature;
2. apparatus for measuring density of specimens to four significant figures;
3. monitoring equipment for determining quantity of krypton and xenon evolved during annealing;
4. apparatus for dissolving irradiated specimens and collecting gas evolved;
5. apparatus for purifying fission gas and measuring total quantity evolved from dissolved specimens.

Some experience in the performance of this equipment has been gained in connection with pulse-annealing operations on 2 aluminum-clad, aluminum-plutonium specimens which had been irradiated in MTR to

essentially 100% burnup of fuel. A slight decrease in volume of these specimens was observed as a result of annealing at temperatures up to 550°C, followed by only a small increase between 550 and 600°C. The gas evolved by chemical dissolution was purified and measured in the apparatus listed above, and was found to consist entirely of hydrogen and minor contaminants. The absence of both xenon and krypton explains the lack of appreciable swelling in the aluminum-plutonium specimens when heated to temperatures approaching their melting point.

The fact that fission gas may be accommodated in aluminum-plutonium without adverse changes in volume, and held there until total burnout of both fuel and gas is complete, gives some hope that other compound systems may be found which have in their lattices sites which can trap gas atoms and prevent their agglomeration for bubble formation. It is proposed during 1960 to investigate this possibility.

4. Effect of Neutron Irradiation on the Thermoelectric emf and Electrical Resistivity of Metals and Alloys (F. R. Taraba)

The program initiated last year to study the relative effects of cold work and radiation damage upon the thermoelectric emf and electrical resistivity of metals and alloys continued throughout 1959. During this period the effects of cold work upon the thermoelectric emf and electrical resistivity of several pure metals and alloys were investigated. The kinetics of the recovery of these properties were also investigated by a pulse-annealing technique aimed at constructing a property-versus-time curve essentially under isothermal conditions, the assumption being that the successive heatings and coolings produce changes in the property which are insignificant when compared with changes at the elevated temperature.

From a series of such curves and a method of analysis developed by Vand,[51] it is possible to determine an activation energy spectrum of lattice defects, i.e., a curve showing the relative number of defects associated with a particular activation energy of healing. Studying the kinetics of recovery provides a method for investigating the nature of the damage and also gives information on the behavior of the various types of lattice disorder. Since different properties may not be equally affected in the healing of different types of lattice defects, additional information may be gained by studying two properties simultaneously. The following graphs are typical of the results obtained so far in the investigation.

---

51 V. Vand, A Theory of the Irreversible Electrical Resistance Changes of Metallic Films Evaporated in Vacuum, Proc. Phys. Soc. (London) A55 222 (1943).

Figure 58 shows the variation of the electrical resistivity (measured at 20°C) of a nickel wire which has been successively cold worked by swaging. The gradual increase in resistivity with increasing amount of cold work is typical of pure metals. However, this is not always the case with alloys. Figure 59 is an example of an alloy, nichrome, which shows the electrical resistivity decreasing with increasing amount of cold work. Figure 60 illustrates the dependence of the thermoelectric emf of nichrome relative to annealed iron upon the amount of cold work. The temperature differential between the hot and cold junctions of the iron-nichrome thermocouple was maintained at 20°C. Similar behavior has been observed in the case of pure metals. Metals showing the opposite behavior have also been observed. Figure 61 shows the effect of cold work upon the thermoelectric emf of fully annealed and cold-worked nichrome relative to annealed iron. The effect of the cold work is exhibited as a decrease in the thermoelectric power of nichrome, i.e., in the slope of the emf versus temperature curve. Figures 62 and 63 show isothermal annealing curves for cold-worked nichrome. These curves were obtained by the pulse annealing technique. Figure 62 shows the recovery of the thermoelectric power at 150°C. Figure 63 shows the recovery of the electrical resistivity at 150°C. It should be pointed out that this behavior of the resistivity during annealing is not characteristic of all alloys. In the case of pure metals the normal behavior is just the reverse, i.e., the resistivity decreases during the annealing process.

Figure 58

The Electrical Resistivity of an Electrolytic Nickel Wire Versus Reduction in Cross-sectional Area

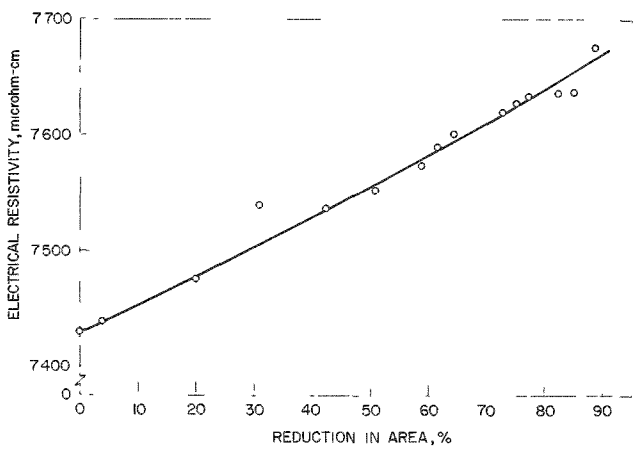

Figure 59

Electrical Resistivity of a Nichrome Wire Versus Reduction in Cross-sectional Area

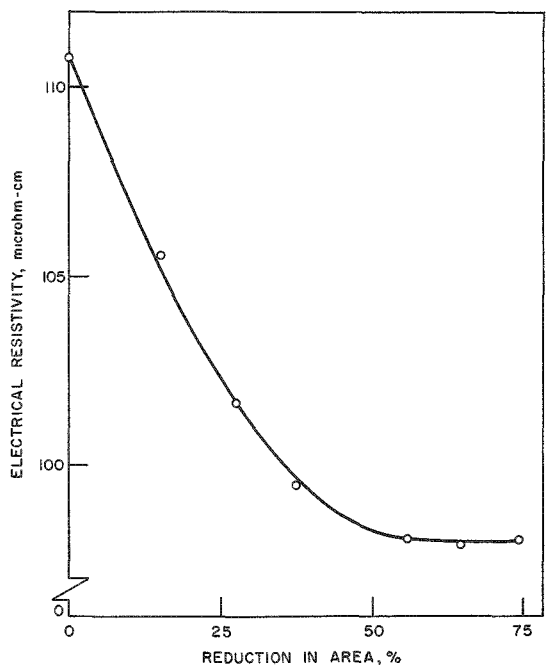

Figure 60

Thermoelectric emf of Nichrome Relative to Iron Versus Reduction in Area (ΔT = 20°C)

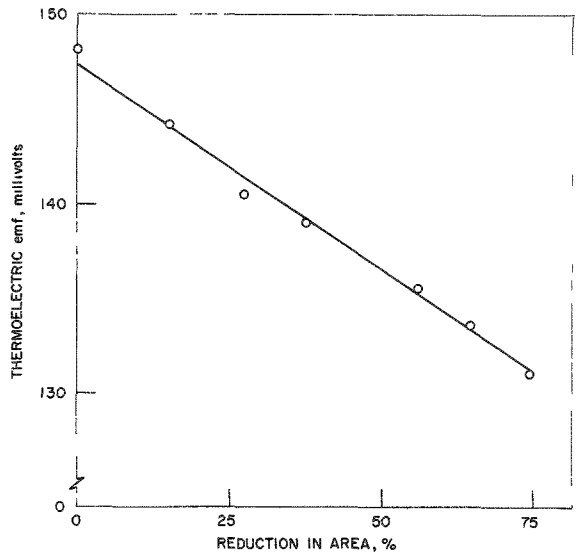

Figure 61

Thermoelectric emf of Cold-worked and Annealed Nichrome Relative to Iron

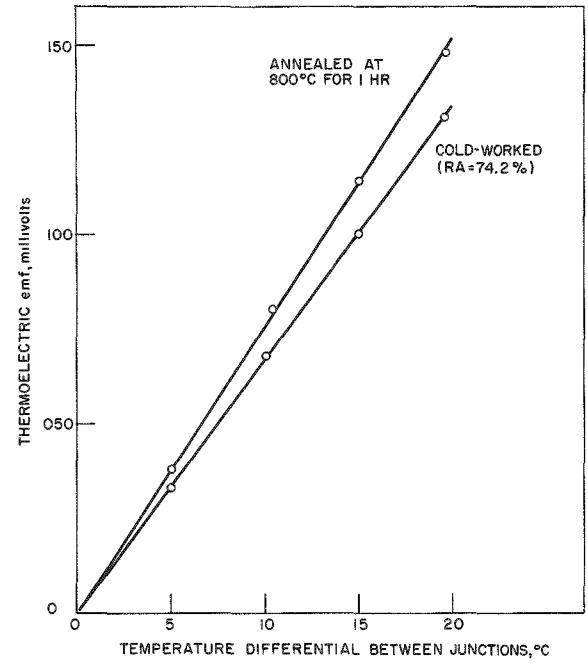

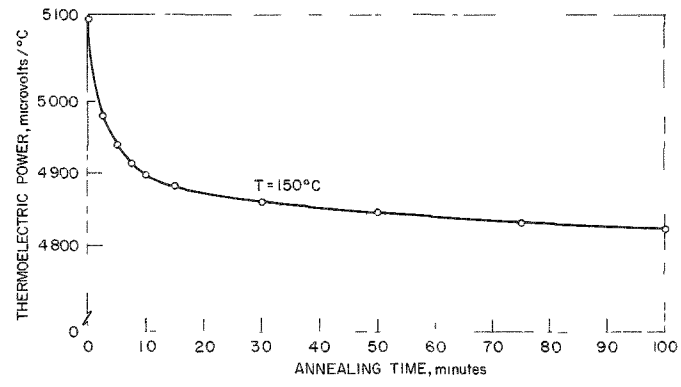

Figure 62

Thermoelectric Power of Cold-worked Nichrome Relative to Constantan during Isothermal Annealing (RA = 76.2%)

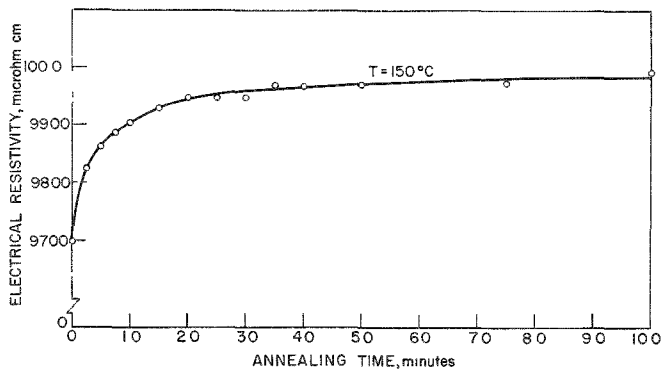

Figure 63

The Electrical Resistivity of Cold-worked Nichrome during Isothermal Annealing (RA = 76.2%)

Figure 64 shows a series of isothermal annealing curves for a cold-worked nickel wire. The curves show the recovery of the electrical resistance at several temperatures ranging between 350 and 700°C. The same wire specimen was used in obtaining each of the 6 curves. Each curve of the series was obtained by pulse annealing the specimen at a particular temperature, starting with the lowest temperature, until no further measurable change occurred in the resistance. Figure 65 is the result of an application of the Vand analysis to the isothermal annealing curves shown in Figure 64. Each bell-shaped curve was derived from a particular annealing curve. The ordinates, $N(\epsilon)$, and abscissae, ϵ, represent the relative number of lattice defects and the activation energy of healing, respectively.

Figure 64

The Electrical Resistance of Cold-worked Nickel During Isothermal Annealing (RA = 74.6%)

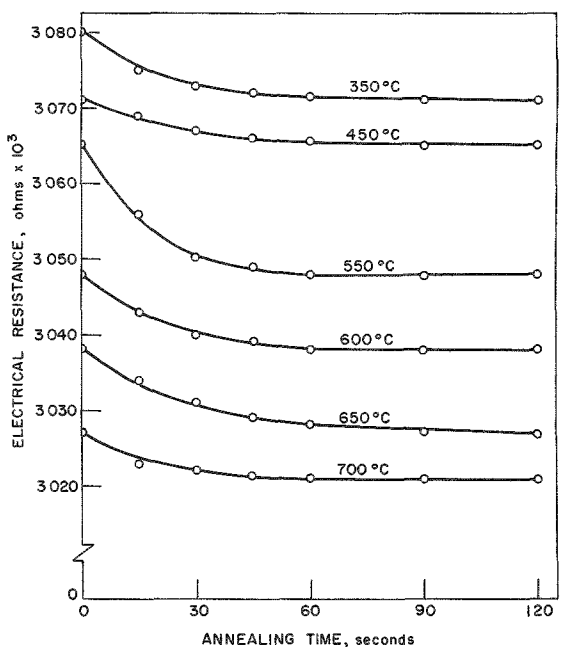

Figure 65

Components of the Activation Energy Spectrum of Lattice Defects in Cold-worked Nickel at Room Temperature (RA = 74.6%)

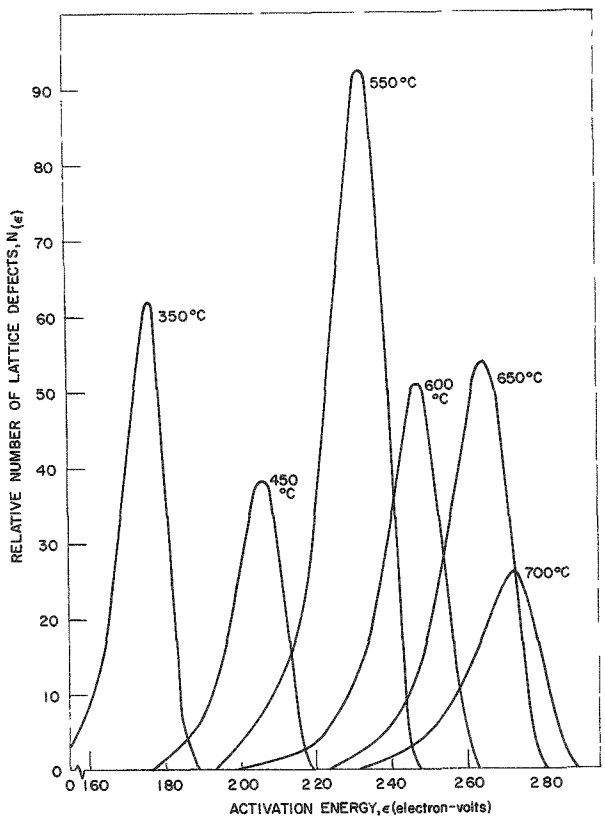

According to the Vand analysis,

$$N[\epsilon(t)] = -\frac{t}{kT}\left[\frac{dR}{dt}\right]_t \quad , \tag{1}$$

and

$$\epsilon(t) = kT \ln vt \quad . \tag{2}$$

The various symbols appearing in equations (1) and (2) are defined as follows: $\left[\frac{dR}{dt}\right]_t$ is the time rate of change of the electrical resistance at time t, i.e., the slope of the annealing curve at the time t, T is the annealing temperature (°K), v is the lattice frequency factor (sec^{-1}), k is the Boltzmann constant (ev/°K) and t is the annealing time (sec). The quantity $\left[\frac{dR}{dt}\right]_t$ was computed from the analytical expression representing the change in the electrical resistance with time, R(t). The analytical expressions for R(t) [one for each annealing curve] were derived from a least squares analysis of the annealing data and are of the form

$$R(t) = a_1 e^{-\lambda_1 t} + a_2 e^{-\lambda_2 t} \quad . \tag{3}$$

Figure 66 is the composite of the curves shown in Figure 65. It is a curve showing the relative number of defects characterized by a particular activation energy of healing. Figures 64, 65, and 66 pertain to high-purity nickel which was cold worked at room temperature by swaging.

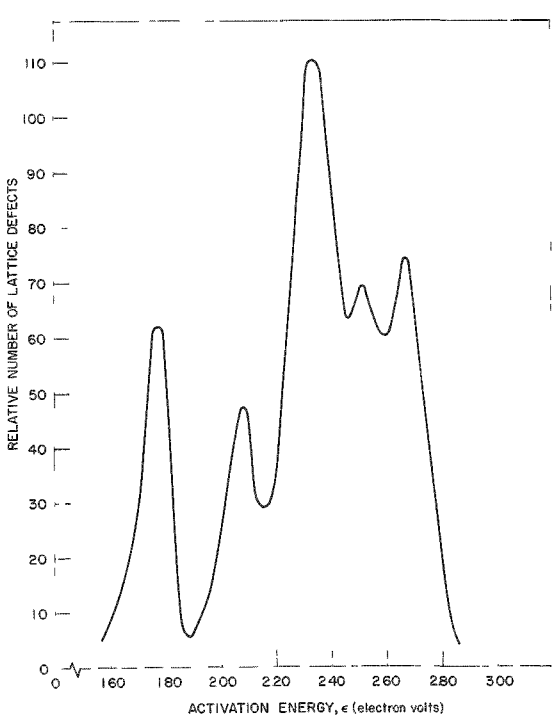

Figure 66

Activation Energy Spectrum of Lattice Defects in a Nickel Wire Cold Worked at Room Temperature (RA = 74.6%)

I. Ceramic Materials Research

1. Sintering Mechanisms of Al_2O_3 Single Crystals
(G. C. Kuczynski* and J. M. Allan)

Publications:

1. G. C. Kuczynski, L. L. Abernethy and J. M. Allan, "Sintering Mechanisms of Aluminum Oxide," in Kinetics of High Temperature Processes, John Wiley and Sons, Inc. (1959) pp. 163-172.

2. G. C. Kuczynski, L. L. Abernethy and J. M. Allan, "The Chemical Aspects of the Sintering of Aluminum Oxide," Plansee Proceedings, 1958, High-Melting Metals, 1-12, Metallwerk Plansee Ag., Reutte/Tyrol (1959).

The results discussed in the above papers indicated that the predominant process responsible for welding particles of aluminum oxide together is that of volume diffusion. However, great differences in rates were observed when the single-crystal spheres were sintered in reducing and oxidizing atmospheres. Moreover, heating in a reducing atmosphere of dry hydrogen resulted in the loss of the material due to evaporation, causing the transformation of the spheres into polyhedra.

The diffusion coefficient derived from the original sintering data in oxidizing atmospheres of O_2, He, and wet H_2, namely, $D = 2.5 \times 10^4 \exp(-131{,}000/RT)$ cm^2/sec, was not in agreement with the value obtained by Coble,[52] namely, $D = 10^7 \exp(-165{,}000/RT)$ cm^2/sec. The sintering rates were therefore remeasured in wet H_2 and O_2. The new results yielded a coefficient very close to that of Coble's, namely, $D \doteq 1.4 \times 10^7 \exp(-160{,}000/RT)$.

Sintering studies of aluminum oxide single-crystal spheres in vacuum ($< 10^{-6}$ mm Hg) indicated that the controlling process is the volume diffusion, with a coefficient of diffusion $D \cong 10^{10} \exp(-213{,}000/RT)$ cm^2/sec. When compared with the diffusivity obtained from sintering rates measured in dry H_2, $D \cong 10^{15} \exp(-215{,}000/RT)$ cm^2/sec, it is evident that the activation energies are practically identical in both cases, but the values of the frequency factor differ by a factor of 10^5. This would indicate that the concentration of defects (aluminum vacancies or interstitials, oxygen vacancies or interstitials) is greatly dependent on oxygen pressure. In the case of heating in H_2, oxygen vacancies or aluminum interstitials are produced by the reaction $Al_2O_3 + H_2 \rightleftharpoons Al_2O + 2H_2O$. In vacuum, similar defects

*The University of Notre Dame, Consultant to ANL Metallurgy Division.

[52] R. L. Coble, J. Amer. Cer. Soc., 38 187 (1955).

can be produced by Al_2O_3 decomposition: $Al_2O_3 \rightleftharpoons Al_2O + O_2$, provided that the oxygen pressure in the surrounding atmosphere is lower than that corresponding to the above reaction. If the process in question is controlled by oxygen ion diffusion, it can be shown that $D \cdot p_{O_2}^{-1/3}$, where p_{O_2} is the oxygen pressure. If the process rate is controlled by the diffusion of interstitial aluminum, then $D\ p_{O_2}^{-3/4}$. Thus, the problem of which ion diffusion actually controls the rate of sintering in Al_2O_3 can be experimentally resolved by measuring the sintering rates of spheres at various very low oxygen pressures. At present no such data are available.

2. Evaporation of Al_2O_3 Single-crystal Spheres in Dry Hydrogen (G. C. Kuczynski and D. W. Readey*)

It has been observed in the course of sintering aluminum oxide spherical particles in pure hydrogen that a copious evaporation occurs which results in a reduction of sphere size and in a change in shape from spherical to polyhedral. Closer observations of this phenomenon revealed that the development of the facets is most pronounced and fastest near the neck between two sintered spheres, and that at other locations the facets are in the form of extremely fine sets of steps (see Figure 67).

Measurement of the evaporation rate of single spheres or plates yielded the following relationships:

(1) $r_0^2 - r^2 = F_1(T)\ t$ for spheres,

where r_0 is the original radius, r the radius after time t, and $F_1(T)$ some function of temperature only;

(2) $d_0 - d = F_2(T)\ t$ for plates,

where d_0 is the original thickness of the plate and d, that after time t, and $F_2(T)$ a function of temperature only. Both equations are consistent with the hypothesis that a volatile suboxide, Al_2O or/and AlO, forms on the surface by reduction of Al_2O_3 with H_2. The activation energies for the process in both spheres and plates were found to be almost the same, ranging between 100 and 120 kcal/mol. This activation energy is very close to that for nucleation of facets[53] and polygonization[54] of Al_2O_3 crystals.

The fine facets (Figures 67, 68 and 69) are essentially composed of steps formed by basal planes of (0001) type and of prismatic planes of either $(10\bar{1}0)$ or $(11\bar{2}0)$ type (Figure 67), or both (Figure 68). Apparently

*Student Aide, Summer, 1959.

[53] G. C. Kuczynski, L. L. Abernethy and J. M. Allan, "Sintering Mechanisms of Aluminum Oxide," in Kinetics of High Temperature Processes, John Wiley & Sons, Inc. (1959), pp. 163-172.

[54] J. E. May, "Polygonization of Sapphire " in Kinetics of High Temperature Processes, John Wiley & Sons, Inc. (1959) pp. 30-37.

the surface tensions of the $(10\bar{1}0)$ and $(11\bar{2}0)$ type planes are nearly equal. These three planes seem to have the lowest surface tension.

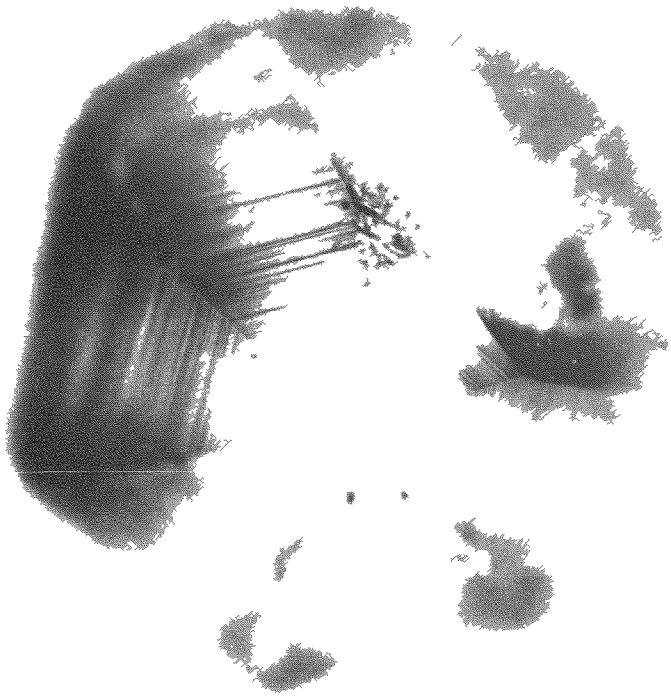

Figure 67

0.0625-in. Diameter Al_2O_3 Sphere Heated in Dry H_2 at 1850°C for 110 minutes.

Micro 26197 125-X

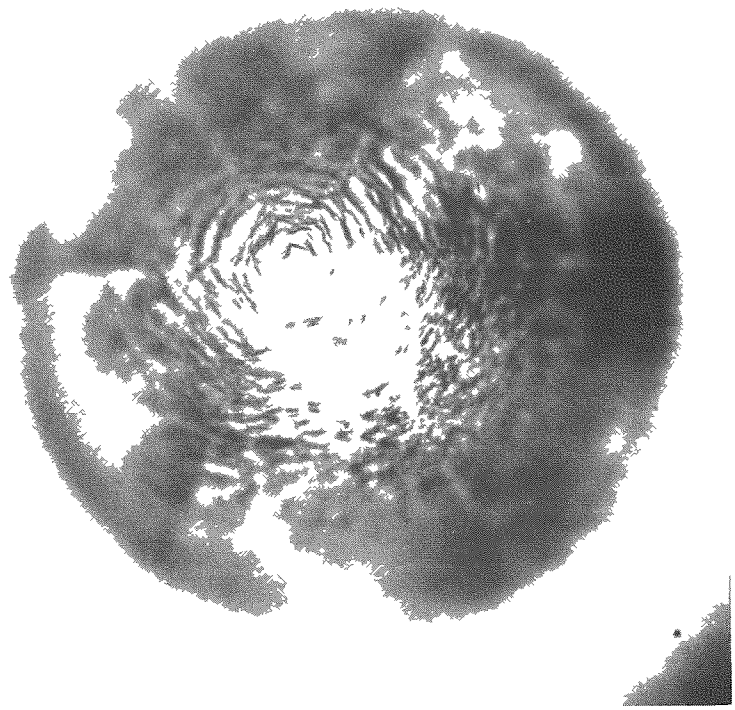

Figure 68

0.030-in. Diameter Al_2O_3 Sphere Heated in Dry H_2 at 1600°C for 120 Minutes.

Micro 26652 125-X

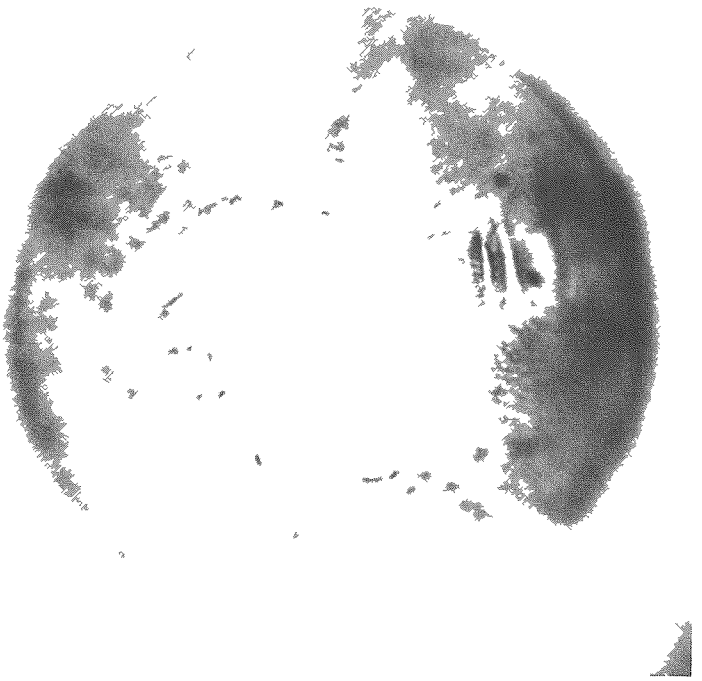

Figure 69

0.030-in. Diameter Al_2O_3 Sphere Heated in Dry H_2 at 1700°C for 140 Minutes.

Micro 26651 125-X

3. Sintering Mechanisms in Nonstoichiometric Oxides (P. F. Stablein, Jr.)

An air grinder has been designed and built to produce spheres suitable for neck-growth sintering studies. The apparatus consists of a cylindrical cavity lined with a strip of abrasive paper. The powdered sample is introduced into the cylindrical cavity through a tuyere located tangentially with the inner wall. A jet of compressed air introduced through the tuyere sets the particles in turbulent motion against the abrasive paper. The apparatus has been used successfully to produce spheres of UO_2, ThO_2, and MgO. The time required depends on the quality of the paper, the radius of the cylindrical cavity, and the hardness of the powder. The sizes of spheres produced range from 10 to about 80 mils in diameter. Spheres have been made from pellets produced from powders as well as from fused material; however, the surfaces have been quite rough. Although the ground spheres have good sphericity, thus far no satisfactory method has been found for polishing the surfaces.

Attempts to sinter UO_2 spheres in vacuum or in pure hydrogen at temperatures ranging from 1700 to 2500°C have to date been unsuccessful. The spheres were placed in a grooved tungsten heater in a manner such that good contact was maintained between them, yet no observable "necks" could be produced. The major difficulty has been the excessive

evaporation which occurs. Attempts to reduce the evaporation by using tungsten radiation shields around and within the slot in the tungsten heater have not been successful.

Considering the low sintering rates that have been observed in densification studies on stoichiometric UO_2,[55] and the diffusion coefficient of U in "pure" UO_2 the lack of growth of necks under the conditions of our experiments is perhaps not too surprising (our material is close to stoichiometric UO_2). At 2500°K the coefficient is about 10^{-10} cm^2/sec, and for an observable neck to form, considering the roughness of the surface, it would need to have a radius of at least 10^{-3} cm. To grow such a neck would require up to ten hours of heating at these temperatures, and the copious evaporation prevents such an experiment. At present, new experimental techniques are being tried to reduce further the evaporation rate.

4. Mechanism of Solid-Gas Reactions (M. L. Volpe)

The objectives of the investigation of the kinetics of reduction of uranium oxides between U_3O_8 and UO_2 by hydrogen have been to determine how the reaction rate is affected by reaction variables such as hydrogen pressure, reaction temperature, and O/U ratios and to attempt to deduce from these the mechanism of the reaction The method selected for measuring the reduction rate was that of following the decrease of hydrogen pressure with time. This method rather than the flow method at constant pressure used by former investigators[56] was chosen, because it permitted obtaining rate data at essentially constant O/U ratios. This eliminated the occurrence of bulk crystal structure changes during reduction which would occur if the O/U ratio were to change thus simplifying the interpretation of the data In the work reported below, reduction rates were measured at initial pressures of about 600 microns Samples weighing more than 1 gram were used, with about 50 micromoles of hydrogen, so that the O/U ratio decreased during a given run by no more than 0.35%. The rates were measured at various O/U ratios between 2.67 and 2 00.

Two kinds of oxide samples were used. Powder samples of U_3O_8 were obtained by air oxidation of highly purified uranium metal Some experiments were also performed on fused material of relatively large particle size. High-purity gases were used in all the tests.

Results: Typical data of a number of reduction runs at 600°C with powders are shown in Figure 70 as plots of pressure versus time The plots represent consecutive runs under almost identical conditions

---

[55] J. Williams, E Barnes, R Scott, and A Hall, J Nuc. Materials, 1 (1) 28 (1959).

[56] J. Belle and L J. Jones, Resume of Uranium Oxide Data, WAPD-904 (1956).

Figure 70

Consecutive Reduction Runs of U_3O_8 at 600°C.

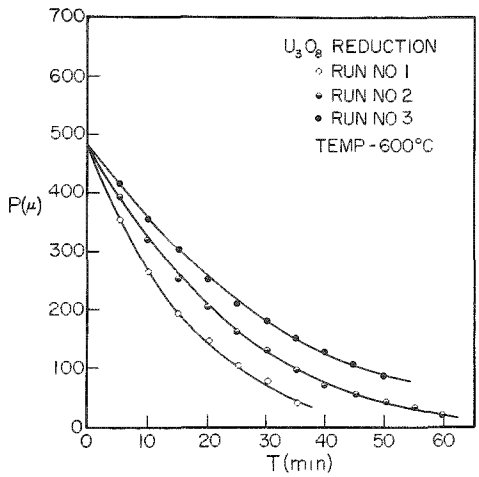

of temperature, pressure, and composition, and show a progressive decrease in rate, particularly in the initial stages. The magnitude of the decrease diminished with increasing number of runs, with the rate sometimes approaching a limiting value after about 5 to 6 runs. However, even this limit did not seem to be reproducible. The discrepancy between successive runs in a given sample was greater when its oxygen content was attained by oxidation rather than by reduction from a higher state.

The following were considered as possible causes for the nonreproducibility: (a) successive removal of oxygen atoms from an oxygen-rich surface layer; (b) absorption of hydrogen and oxygen by the platinum alloy thermocouples; and (c) the formation of a surface barrier for hydrogen by gradual adsorption of water vapor on the solid oxide. To test these possibilities, an experiment was run in which the sample was exposed to about 5 mm of water vapor pressure prior to the reduction run; no effect was noted. As for a possible reaction of the hydrogen with the platinum, a test at 600°C indicated some reaction to the extent corresponding to only 5% of the pressure decrease; hence it cannot account fully for the lack of reproducibility. The postulated presence of an oxygen-rich layer and its successive removal is yet to be evaluated.

Discussion: An attempt was made to fit the data to the following general equation, in order to provide a relationship between the rate and the reaction variables which could be used in evaluating the mechanism:

$$-dP/dt = R'(Ox)^n(A)^k(P)^m, \qquad (1)$$

where (Ox) represents the concentration of reducible oxygen in the oxide, A is the surface area, and R' is a constant. Since the oxygen concentration remained constant during a run, and assuming a constant surface area, equation (1) can be integrated to give:

$$(P/P_0)^{(1-m)} = 1 + R\,(m-1)(Ox)^n\,P_0^{(m-1)}t \quad \text{for } m \neq 1 \qquad (2)$$

and

$$\ln(P_0/P) = R(Ox)^n t \quad \text{for } m = 1 \quad . \qquad (3)$$

Here P_0 is the pressure at time t = 0 and $R = R'(A)^k$. Plots of the data as $\ln(P_0/P)$ or $(P/P_0)^{(1-m)}$ vs. time t according to the above equations

yielded straight lines for values of m between 0.75 and unity. However, the constancy of m and n has not yet been tested. The value of n will be determined from the slopes of lines obtained for different O:U ratios.

In another approach to the problem, a diffusion mechanism was postulated in which it was assumed that the diffusion of hydrogen into the solid was the rate-determining process after a very rapid attainment of surface equilibrium. Such a mechanism yields the following two equations:

$$P^{1/2} = P_0^{1/2} - At^{1/2} \quad \text{for hydrogen atom diffusion} \qquad (a)$$

and

$$P = P_0 - At^{1/2} \quad \text{for hydrogen molecule diffusion;} \qquad (b)$$

Here A is a constant. Plots of P vs. $t^{1/2}$ deviated appreciably from linearity, whereas plots of $P^{1/2}$ vs. $t^{1/2}$ yielded good straight lines except for the initial time intervals (see Figure 71). The initial curvature might be attributed to the attainment of surface equilibrium. The fact that the slopes of the linear portions were nearly the same might indicate that whatever process produced the curvature was also responsible for the nonreproducibility.

Figure 71

Reduction Data of U_3O_8 in Hydrogen at 600°C

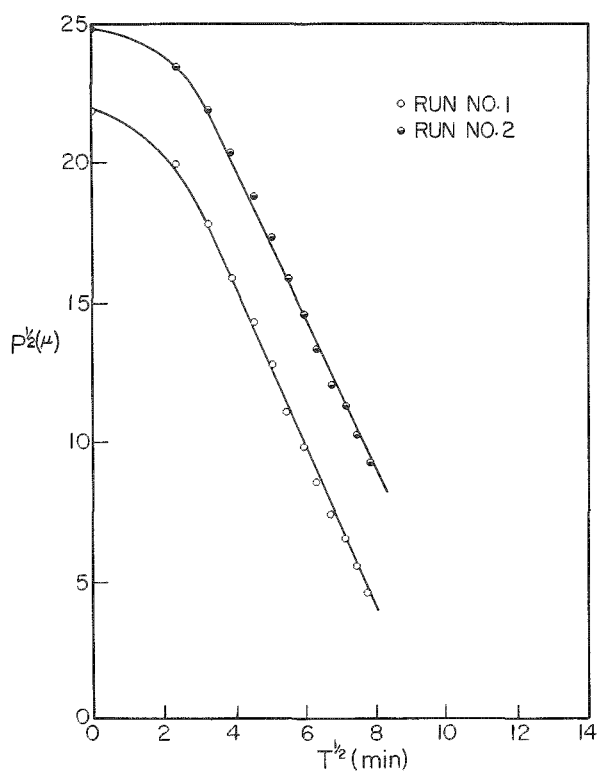

5. Metallographic Techniques for Ceramic Materials (S. J. Rothman)

An apparatus has been built for etching ceramics by ion bombardment. The sputtering chamber consists of a 4-in. ID bell jar which seals against an O-ring in an aluminum base plate The base plate, which is grounded, serves as the anode. The negative electrode is a hollow, water-cooled, tapered aluminum post, which fits into a tapered hole in the base plate and is insulated from the base plate by a glass standard-taper bushing. The gas-inlet tube, vacuum system, and vacuum gauge are also attached to the base plate.

Single and polycrystalline samples of UO_2 have been etched in this equipment with good results. Single crystals developed shallow, round etch pits similar to those found by Bierlein et al.,[57] but not at all like the ones developed by chemical etching. The reason for this difference is at present not understood. Similar round etch pits have been developed on stainless steel and aluminum samples. Etching of polycrystalline UO_2 samples showed up the grain boundaries quite nicely.

The equipment also has been used successfully to etch samples made up of two metals with different etching characteristics and to etch metals that are difficult to etch chemically.

---

[57] T. K. Bierlein, H. W. Newkirk, Jr., and B. Mastel, Etching of Refractories and Cermets by Ion Bombardment, J Am. Cer. Soc. 41 196 (1958).

APPENDIX A

METALLURGICAL FACILITIES CONSTRUCTION PROJECTS

The development of new metallurgy facilities for the Metallurgy Division continued to occupy a considerable portion of the time of a number of staff members of the Division during 1959, even more so than in the previous year. The status of these construction projects and several important equipment design developments are discussed below. A description of pertinent building areas and their functions along with a discussion of the design criteria are contained in the 1958 Annual Report.

Fuels Technology Center (Building 212)

Wings A-E: Estimates as of the end of the year indicate the completion date of construction and occupancy of Wings A-E, the administrative and physical metallurgy laboratory areas, will be in the early spring of 1960. Occupancy engineering work on Wings C and E has been nearly completed and work is currently in progress on Wing D. Meanwhile, procurement of furniture and new laboratory equipment is being timed so that delivery will correspond with the occupancy period.

A small concrete block building (D-40), equivalent to one full-size Wing D plutonium laboratory, was constructed to serve as a mock-up area. It has been used to evaluate certain design features of D-212, such as building ventilation, glovebox ventilation, and the method of bringing utilities and services to equipment for use with plutonium. It is also being used to evaluate designs of equipment for use with plutonium properly enclosed in gloveboxes and to develop efficient plutonium-handling techniques. Based on our experience to date in this mock-up facility, our free-standing glovebox approach to the problem of handling plutonium has worked out extremely well; in fact so well, that we have recently been able to begin experimental development work on plutonium ceramics materials in the mock-up area, even though it was not initially intended to introduce plutonium into this area. Owing to the free-standing glovebox concept, we anticipate no difficulty in relocating the equipment, even though contaminated, to D-212 when construction of the new building is completed. The mock-up area also permitted us to gain valuable working experience in methods we intend to use in D-212 to control materials, security, health physics, accountability, and criticality.

A major development during the past year concerns the gas atmosphere system that we plan to provide for the gloveboxes in which plutonium will be handled. Extensive tests were made on a full-size, recirculating, nitrogen-purification system using catalytic combination of hydrogen with oxygen to form water and adsorption drying to remove the water. The

basic system appeared promising, especially as regards cost, when compared with the low-temperature adsorption purification system that we have been using to purify helium in our Plutonium Laboratory in D-200. However, some of the volatile materials which are used in metallurgical operations were found to poison the catalyst and to appreciably shorten its useful life. Traps were developed to protect the catalyst, and regeneration cycles and other operating details were determined. Nevertheless, a re-evaluation of the system indicated that it was more expensive and more complicated than originally envisioned. Also, operation and maintenance would require considerable attention from specially trained technical personnel. We have therefore proceeded to develop a much simpler glovebox atmosphere system which satisfies our plutonium-handling requirements even better than the above-described system and at a considerable savings in cost. It consists of a very low once-through flow of nitrogen. This approach had been considered early in the design of D-212, but it was discarded because analysis indicated that flow rates of 2 to 5 cfm per glovebox, then considered a minimum, would result in exorbitant costs. However, we have since found that our gloveboxes are extremely tight (<0.005% in leakage/hr), thus permitting us to use extremely low flow rates, of the order of only 0.1 to 0.2 cfm per glovebox. We have tested this system in our mock-up area and have enhanced its feasibility by developing an extremely simple pressure-control system and a simple high-insurance exhaust filtering system. Thus, with this system, 20 to 30 cfm of nitrogen will suffice to provide the gas atmosphere for 100 gloveboxes. The system requires a minimum of maintenance and can be handled easily by building maintenance personnel.

We also plan to move the helium atmosphere recirculating system and purifier from our present plutonium laboratory to D-212. It has worked very well for 5½ years and will satisfy our inert gas needs in experiments where nitrogen is not a chemically suitable atmosphere.

The extruded aluminum frame gloveboxes that we developed to satisfy our plutonium equipment-enclosure requirements have been ordered from the General American Transportation Corporation and will be finished before we occupy the new building.

Wing F: Construction of Wing F, the alpha-gamma cave and hot laboratory facilities, was started early in 1959. At the end of the year, construction was estimated at 47% completion. The building construction contractor is erecting the cave shell simultaneously with construction of adjacent office and laboratory areas. Occupancy of this area is planned for mid 1960.

Since it is essential that the cave be leak-tight, helium leak-testing of the entire cave is specified. Approximately 3500 linear feet of weld joints and 1200 shell penetrations will be inspected for helium leak-testing.

Testing of component items was started late in 1959. Numerous leaks were found in the first items. Enforcement of a requirement that the contractor first perform soap-bubble leak tests on welded items subsequently reduced the incidence of leaks found in the helium test.

Construction of the cave proceeded without interruption through the latter half of 1959. Some difficulties are being experienced in obtaining necessary flatness of walls and floors. The quality of the field welding has steadily improved.

Design of manipulators, internal doors and drives, seals, and similar nonconstruction items is under way in the Remote Control Division. Provision has been made in the construction of the cave to use either mechanical or electronic manipulators, depending upon the state of development at the time procurement of manipulators is to start.

Wings G and H: The definitive (Title II) design of Wings G and H, the engineering metallurgy development facilities, was completed in April 1959. Contracts were awarded and construction started in June 1959. At the end of the year overall construction was estimated as 25% complete. The completion of both wings is presently scheduled for July 1960.

Wing G, which will house the Jacketing and Coating, Engineering Ceramics, and Engineering Corrosion Groups, and an X-ray Radiography facility, was designed basically as a two-floor structure with a high bay area adequate for tall equipment, vertical operating space, and high heat load. The ground floor has 23,890 square feet of functional area, including 8,140 square feet of high bay area. The second floor has 8,640 square feet of functional area out of a net area of 19,920 square feet. The nonfunctional area of 11,280 square feet is used to house heating and ventilating equipment and the electrical switchgear for the wing. The basement in Wing G is 5,130 square feet in area and houses the recirculating chilled-water system which services the entire building, the retention tanks, and the air-conditioning units for the wing.

Wing H was designed essentially as high bay area with only enough second floor space to house the heating and ventilating equipment, electrical distribution switchgear, and some services. The Foundry and Fabrication Group and the Machine Shop will be housed in this wing. The functional area of the ground floor of Wing H amounts to 29,800 square feet, of which 23,560 square feet is high bay. The net area of the ground floor is 33,270 square feet. The net area of the second floor is 9,710 square feet, most of which (8,900 square feet) will be nonfunctional. The basement area of Wing H includes space for the foundry service floor, generator room, retention tanks, and air compressors.

The major portion of both Wings G and H will not be air-conditioned; only offices and selected laboratories are The general area will be ventilated by filtered air supply units and roof exhaust fans. Dust and fumes generated within these wings will be exhausted through appropriate exhaust units. Fume from plating and pickling operations will be exhausted through scrubber units. Contaminated particulate matter generated in the ceramic and metal-working areas will be exhausted through bag units of the reverse jet type. Air from the toxic materials laboratory and equipment, in which material such as beryllia will be handled, will be exhausted through high-efficiency (AEC) filters.

Known contaminated and chemical liquid waste will be removed via "Dempster Dumpsters," and suspect waste through retention tanks. The recirculating chilled-water system mentioned previously will be used wherever possible. It will greatly reduce the water demand upon the already overloaded water supply system.

Plutonium Fuel Fabrication Facility (Building 350)

During the past year, the installation of process equipment, hoods, and services in the Plutonium Fuel Fabrication Facility was completed. The equipment, inert atmosphere system, ventilation equipment, and services were "shaken down," modified where necessary, and placed in operation. Figures A1 and A2 are views taken from the east and west ends of the fabricating area. It consists of 19 heavy equipment glovebox lines; 11 of these are connected on either side of a central conveyor enclosure forming a complex which may be ventilated totally or in part by a recirculating inert atmosphere The conveyor, consisting of an electrically controlled, chain-driven railway dolly, allows transfer of materials, tools, and equipment between operating lines without exposure to the air. The process lines enclose melting and casting, centrifugal casting, weighing and inspection, electrochemical, machining, pressing, swaging, drawing, shearing, rolling and heat treating equipment for work directly upon plutonium fuel cores.

Eight additional glovebox lines enclose welding, liquid metals filling, decontamination, rolling, machining and shearing equipment for operations of cladding and bonding jacket materials to the fuel cores. These lines are not interconnected, and contrasting to the conveyorized system, they must be kept at low contamination levels.

Figure A3 is a flow diagram of the recirculation and purification system for the adsorptive purification for helium gas. The helium-purifying system depends upon the capacity for synthetic zeolites to adsorb water and for activated carbon to adsorb oxygen to remove the contaminants which leak into the hood system. Purification is done at 11

Figure A1

View from Southeast Corner of the Fabrication Area, Facility 350

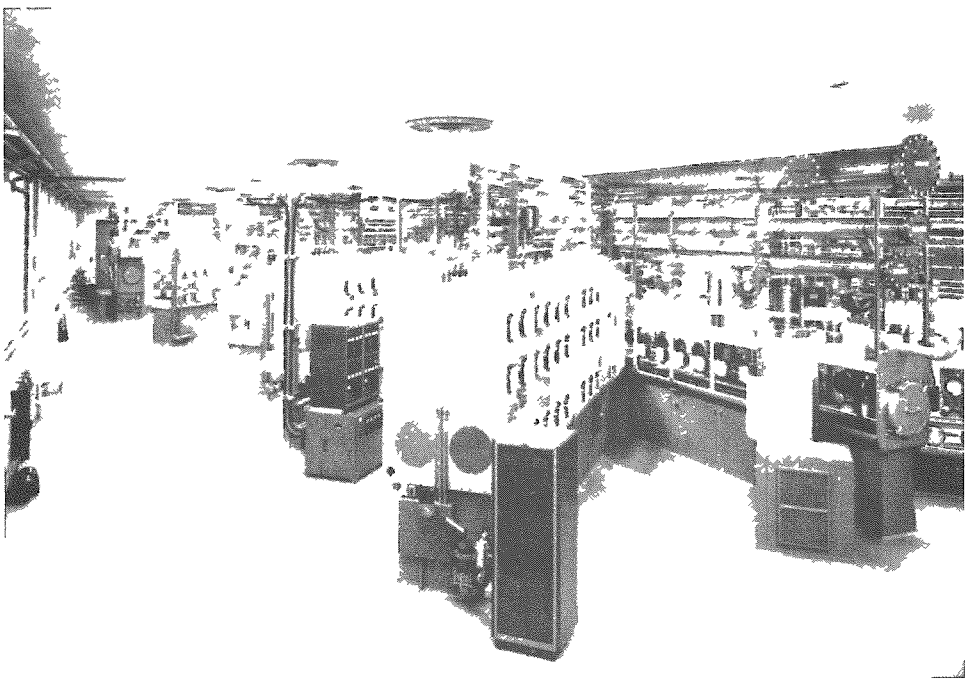

Figure A2

View from West End of Fabrication Area Along the North Side

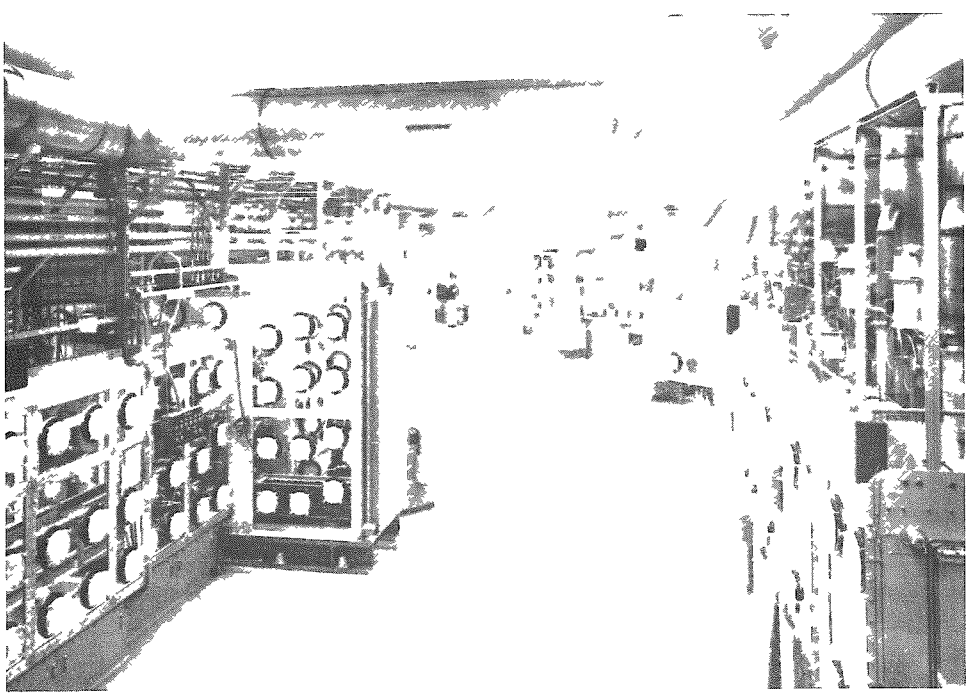

atmospheres to reduce the size of equipment required and to allow adsorption at temperatures obtainable by mechanical refrigeration. A very large part of the work of inspecting the installation consisted of mass spectrometer leak detection and leakage calibration of the gloveboxes, ventilation ductwork, piping and helium recirculating and purifying systems.

Figure A3

Facility 350, Helium Atmosphere System Flow Diagram

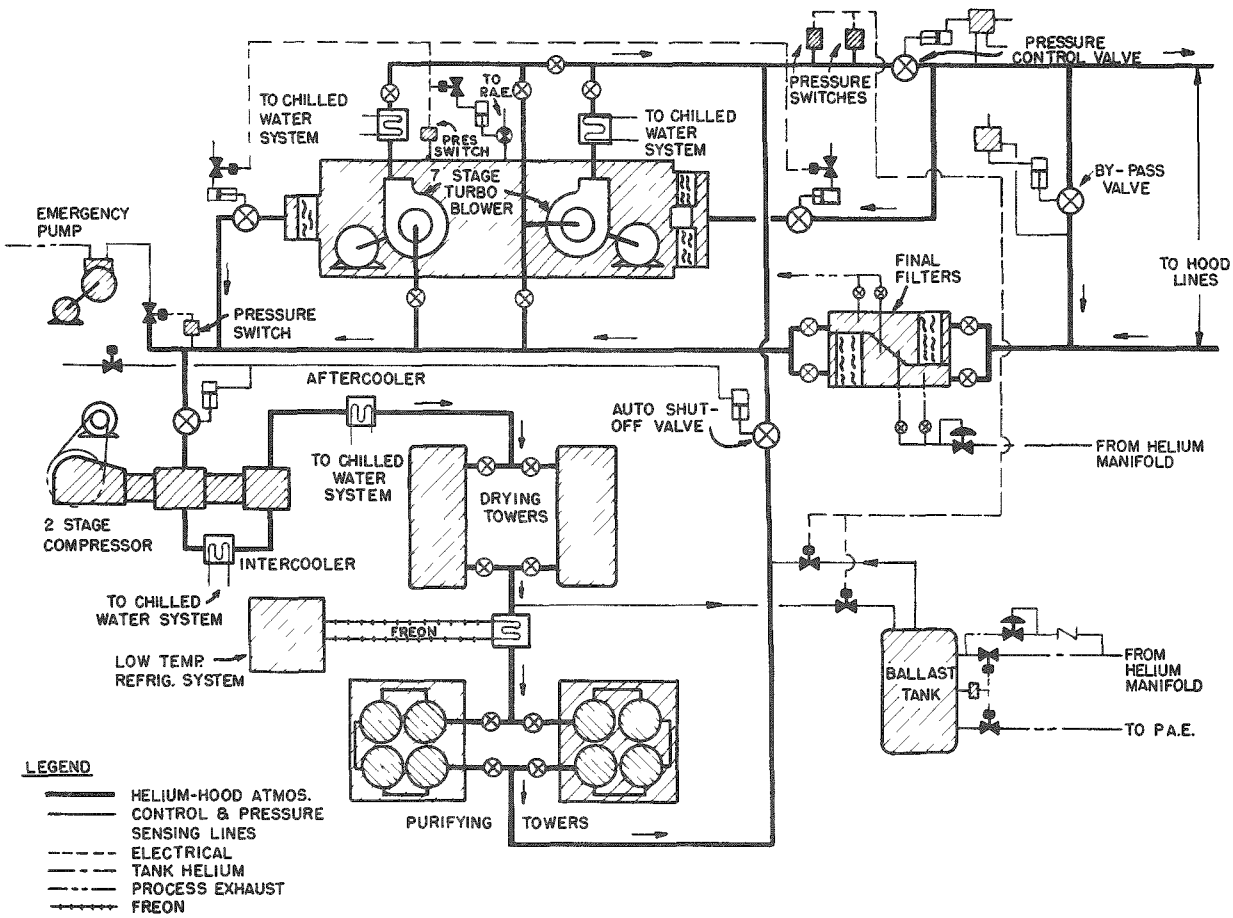

"Shakedown" Operations: A very large part of the "shakedown" work could not be done until all systems had been completed. This included adjustment and balancing of ventilation and hood pressure controls, helium filling of the hoods, the recirculating and purifying systems, and the first operational tests on these systems. Originally a period of three months was programmed for this work. Due to unforeseen difficulties, largely from failure of commercial equipment to meet specified performance, the period was extended to six months. The following major difficulties were encountered in the equipment as originally installed.

(1) Static Hood Pressure Controls

After approximately 2 months of work attempting to adjust and balance some 21 static pressure controllers, the controller manufacturer agreed to exchange them for a more elaborate industrial Type R-1051 controller. The last of these new controllers, operating air purge valves, were installed in November. They have been found reliable over a period of 2 to 3 months of operation, and it was thought to be safe to proceed with the filling of the hoods with helium.

(2) Helium-recirculating System

The helium system consists of a recirculating system and a purifying system. The recirculating system may be operated with all hoods valved off, by passing 100% through a bypass valve. The system was operated for a period of about 2 months prior to final filling. It functioned well. The turbo-blowers were found capable of delivering 2.3 times their rated capacity at 1/2 psi differential. It was necessary to shift the positions of static pressure tips and to revise the control of the gas saver-make-up tank, after which stable control was achieved. No further difficulty was experienced as the hoods were helium filled and placed "on line."

(3) Helium-purifying System

Considerably more difficulty has been experienced in the "shakedown" of the helium-purifying system. The system consists of a two-stage compressor, which compresses 110 cfm of helium to 150 psig, passes it through an aftercooler to synthetic zeolite drying towers from which it is piped through a direct-expansion freon coil to activated carbon towers at -60°F(-51°C) to -80°F(-62°C). A liquid nitrogen heat exchanger can be used to chill further the helium passing through the carbon towers during the startup period or when very dry pure helium is required.

To avoid frosting of the low-temperature stages, the system was operated for a period of two weeks without refrigeration. The carbon towers were pressure-vacuum cycled while the zeolite towers were regenerated with hot gas from the compressor. Several conditions were noticed: (a) the heat of compression was not sufficient for the rapid regeneration of the zeolite beds by using uncooled gas from the compressor, (b) the aftercooler gradually lost efficiency, and (c) valves between the drying towers started to leak and became difficult to

close or open. The insulation was stripped and the system opened. It was found that the 1/16-in. diameter "molecular sieve" material had entered the pipes and valves and plugged the aftercooler. This was apparently caused by fluidization of the beds during startup or closedown procedures.

Modifications made to correct the above situation were (a) installation of a $4\frac{1}{2}$ kw booster heater in the hot gas line, (b) repacking the zeolite drying towers with restraining filters above and below the beds, and (c) installation of a filter in the chilled gas line to protect the aftercooler and compressor. At the same time, a liquid nitrogen cold trap was installed in the vacuum lines from the carbon towers to prevent waterlogging of vacuum pumps and a hot line was installed to permit defrosting of either bank of carbon towers. The system was thoroughly cleaned and returned to operation by November 27. After one week of drying operation, the moisture into the purifying towers had been reduced to 7-15 ppm, allowing refrigeration systems to be operated without danger of frost plugging the system.

A continuous supervised run was started with refrigeration. At first all went smoothly, then there was a gradual increase of helium consumption. After 21 hours, helium consumption had reached 600 cfh. Leak detection showed leakage of helium past Teflon gaskets in flanges where temperatures were between 0°F(-18°C) and -62°F(-52°C). Refrigeration was stopped, and as the system rapidly warmed up under the flow of warm gas the leakage ceased. The operation was closed down pending investigation of this problem.

Teflon O-rings were chilled to -60°C in alcohol-dry ice mixtures and to -293°C in liquid nitrogen. They lost flexibility and became very hard at -60°C. After immersion in liquid nitrogen they would chime like a bell when tapped and shatter when dropped. The literature gave the coefficients of thermal expansion of Teflon as $55.0 \times 10^{-6}/°F$ and of the type 304 stainless steel as $9.6 \times 10^{-6}/°F$. It was reasoned that due to permanent set, inelasticity at low temperatures, and differential expansion, the O-rings contracted away from the stainless steel flange sealing surfaces and allowed leakage.

A pair of stainless steel flanges were made up to allow comparative testing of various gasket materials. A connection was made for pressurizing with helium. Materials tested were Teflon, copper ring gaskets, asbestos-filled copper gaskets, and silicone rubber gaskets. The metallic asbestos-filled and

Teflon gaskets were found to have similar characteristics. All would seal at room temperature and when heated to 400°F (204°C), but would fail when cooled in the alcohol-dry ice mixture. The silicone rubbers appeared to maintain flexibility over a greater range of temperature than the other gasket materials. One O-ring available at the laboratory maintained considerable flexibility down to -40°F(-40°C). Consultation with the manufacturer indicated that a new silicone rubber compound is available which maintains rubbery elasticity and serviceability between -130°F(-90°C) and +400°F(+204°C). Samples of this material are under test. It is expected that once the gasket material has been selected, two weeks will be required for replacing the gaskets and leak detecting the system. An additional two weeks will be required to bring the system back into service.

(4) Ventilation System Changes

Potentially dangerous pressure excursions resulted several times following power outages or emergency shutdown of the ventilation system. In one case, a 3 x 6 ft. duct collapsed and in several instances personnel were trapped in areas where doors were held so tightly against their jams by air pressure that they could not be opened. It was necessary to open all doors between areas and each area to the outdoors to start or stop the system. This was undesirable and to correct it a programmed and interlocked semi-automatic control center was designed and was installed in Basement B by the Plant Services Division. This control center will automatically restart the system without serious pressure excursions in various building zones even after a power outage.

(5) Fire Detection System

Approximately two man-months were required by staff and technicians to make the rate-of-rise fire detection system operable under hood operating conditions and with the pressure fluctuations of the building. As it was left by the installing subcontractor, it would trigger false alarms several times a day and yet would not always respond to a test fire. A new method of calibration was developed, using calibration instruments for ventilation controls, which allows precise setting of the sensitivity. Tap valves were installed to allow attachment of calibrating instruments and a supervisory switch was installed to allow disconnection of the Autocall while testing and while performing high temperature operations within the system.

Operating Manuals: Considerable effort has been expended in the preparation of operating manuals for the various systems and equipment lines. The manual on ventilation and pressure controls is complete. A manual on electrical systems is in preparation and work has begun on the writing of manuals for the process equipment lines, fire detection systems, and helium atmosphere systems. These will be used in training of operating personnel.

APPENDIX B - PUBLICATIONS AND REPORTS
JANUARY 1, 1959 - DECEMBER 31, 1959

Publications

Baskin, Y., Arenberg, C. A., and Handwerk, J. H., "Thoria Reinforced by Metal Fibers," Bull. Am. Cer. Soc. 38 (7) 345-348 (July 1959).

Bean, C. H., McCuaig, F. D., and Handwerk, J. H., "The Fabrication of the Fuel Elements for the Transient Reactor Test," Nuc. Sci. & Engr. Suppl. 2 (1) 47-48 (June 1959).

Blumenthal, Bernhard, "Plutonium," J. Metals 11 (2) 125-129 (February 1959).

Bruckner, W. H. and Myles, K. M., "Studies on the Susceptibility of Cathodically Protected Steel to Hydrogen Embrittlement," Corr. 15 591t-595t (November 1959). [Not based on ANL work]

Darby, J. B., Jr., Tomizuka, C. T., and Balluffi, R. W., "Effect of Simultaneous Torsional Strain on Self-Diffusion in Silver," Bull. Am. Phys. Soc. 4 171 (March 1959). [Not based on ANL work]

Draley, J. E., Ruther, W. E., DeBoer, F. E., and Youngdahl, C. A., "Measuring Equipment for Polarization Studies in Distilled Water," J. Electrochem. Soc. 106 490-494 (June 1959).

Draley, J. E., "Fluid Fuel Power Reactors," Trans. Am. Nuc. Soc. 2 (2) 46-47 (November 1959).

Draley, J. E., "Problems of Fuel Element Corrosion in Water," Nuclear Fuel Elements, ed. H. H. Hausner and J. F. Schumar, pp. 314-328. New York, Reinhold Publishing Corp. (1959).

Dwight, A. E., "CsCl-Type Equiatomic Phases in Binary Alloys of Transition Elements," Trans. AIME 215 283-286 (April 1959).

Dwight, A. E. and Beck, P. A., "Close-Packed Ordered Structures in Binary AB_3 Alloys of Transition Elements," Trans. AIME 215 976-979 (December 1959).

Foote, F. G., "Uranium and Uranium Alloy Fuel Elements," Nuclear Fuel Elements, ed. H. H. Hausner and J. F. Schumar, pp. 67-78. New York, Reinhold Publishing Corp. (1959).

Garrod, R. I. and Hart, R. K., "Transmission Specimen Holder for Electron Diffraction," J. Sci. Instr. 36 44 (1959). [Not based on ANL work]

Greenberg, Sherman, "Corrosion of Irradiated Uranium Alloys," Nuc. Sci. & Engr. 6 159 (August 1959).

Handwerk, J. H. and Noland, R. A., "Fabrication of Fuel Elements for the Borax-IV Reactor," Prog. in Nuc. Energy, Series V, Vol. 2, Metallurgy and Fuels. pp. 239-260, Pergamon Press, London (1959).

Handwerk, J. H. and Hill, D. C., "Ceramic Nuclear Fuels in the System UO_2-ZrO_2-CaO," Industrial Heating 26 (7) 1419 (1959).

Harada, Y., Baskin, Y., and Handwerk, J. H., "Calcination and Sintering Study of Thoria," Industrial Heating 26 (7) 1424 (1959).

Horak, J. A. and Kittel, J. H., "Irradiation Behavior of U-Fs and U-Pu-Fs Fast Reactor Fuels," Nuclear Metallurgy, Vol. VI. A Symposium on Effects of Irradiation on Fuel and Fuel Elements, pp. 35-38. New York (AIME) (1959).

Kehl, George L., Mendel, Eric, Jaraiz, Emilio, and Mueller, Melvin H., "Metallographic Identification of Inclusions in Uranium," Trans. A.S.M., 51 717-735 (1959).

Kingery, W. D., Pappis, J., Doty, M. E., and Hill, D. C., "Oxygen Ion Mobility in Cubic $Zr_{0.85}Ca_{0.15}O_{1.85}$," J. Am. Cer. Soc. 42 (8) 393-398 (1959). [Not based on ANL work]

Kittel, J. H., "Fuel Cycles; Irradiation and Thermal Stability," Proc. 1957 Fast Reactor Information Meeting, pp. 182-188. U.S. Govt. Printing Office, Washington, D.C. (1959).

Kittel, J. H. and Paine, S. H., "Engineering Decisions Based on Irradiation Experiments," Metal Prog. 76 (5) 119-122, 216 (November 1959).

Kittel, J. H. and Paine, S. H., "Effect of Irradiation on Fuel Materials," Nuc. Energy Engineer 13 301-305 and 357-360 (1959).

Kuczynski, G. C., Abernethy, L., and Allan, J., "The Chemical Aspects of the Sintering of Aluminum Oxide," Plansee Proceedings, 1958, High-Melting Metals, pp. 1-12, Metallwerk Plansee Ag., Reutte/Tyrol (1959).

Kuczynski, G. C., Abernethy, L., and Allan, J., "Sintering Mechanisms of Aluminum Oxide," Kinetics of High Temperature Processes, pp. 163-172, John Wiley & Sons, Inc., New York, New York (1959).

Macherey, R. E. and Bean, C. H., "Fabrication of Uranium Base Alloy Fuel Plates for the Experimental Boiling Water Reactor," Prog. in Nuc. Energy, Series V, Vol. 2, Metallurgy and Fuels. pp. 261-279, Pergamon Press, London (1959).

McGonnagle, W. J., "Suggests Nondestructive Test to Aid Nuclear Progress," Steel 144 (1) 281-282 (1959).

McGonnagle, W. J., Renken, C. J., and Myers, R. G., "Improved Nondestructive Testing by Eddy Currents," Electronics 32 (35) 42-43 (August 1959).

McGonnagle, W. J., "Non-Destructive Testing of Fuel Elements," Prog. in Nuc. Energy, Series V, Vol. 2, Metallurgy and Fuels, pp. 380-397, Pergamon Press, London (1959).

Misch, R. D. and Gunzel, F. H., Jr., "The Electrical Resistance of Oxide Films on Zirconium in Relation to Corrosion," J. Electrochem Soc. 106 15-20 (January 1959).

Neimark, L. A. and Kittel, J. H., "Irradiation Behavior of ThO_2-UO_2 Fuels," Nuclear Metallurgy, Vol. VI. A Symposium on Effects of Irradiation on Fuel and Fuel Elements, pp. 83-85. New York (AIME) (1959).

Nevitt, M. V. and Zegler, S. T., "Transformation Temperatures and Structures in Uranium-Fissium Alloys," J. Nuc. Materials 1 (1) 6-12 (1959).

Reinke, C. F. and Markheim, L. S., "The Disassembly and Sampling of an Irradiated EBWR Fuel Subassembly," Proc. 7th Hot Laboratories and Equipment Conf., April 5-10, 1959, Cleveland, Ohio. pp. 409-418. New York (ASME) (1959)

Rothman, S. J. and Fisher, E. S., "A Note on the Elastic Constants of Uranium," Nuc. Sci & Engr. 5 195-196 (March 1959).

Rothman, S. J. and Sobocki, L. J., "Precision Chuck and Chip Catcher for Sectioning Diffusion Samples," Rev. Sci. Instr. 30 201-202 (March 1959).

Schumar, James F., "Manufacture and Exposure History of Boiling Water Reactor Fuels," Proc. of 5th International Electronic & Nuclear Exposition and Congress, Atti del Congresso Scientifico, Vol. 1, pp. 169-187, Rome (1959).

Schumar, J. F., "Fabrication Techniques for Various Types of Fuel Elements," Nuclear Fuel Elements, ed. H. H. Hausner and J. F. Schumar, pp. 48-66. New York, Reinhold Publishing Corp. (1959).

Sidhu, S. S., Heaton, LeRoy, and Mueller, M. H., "Neutron Diffraction Techniques and Their Applications to Some Problems in Physics," J. App. Phys. 30 1323-1340 (September 1959).

Smith, K. F., "Irradiation of Uranium-Fissium Alloys and Related Compositions," Symposium on Radiation Effects on Materials, Vol. 3, pp. 136-144 (1958). [ASTM Spec. Tech. Pubn. No. 233.]

Smith, Karl F., "Development of Vanadium Alloys for Reactor Application. Part I. Evaluation," Reactive Metals, Vol. 2, pp. 403-414. Interscience Publishers, New York, N. Y. (1959).

Taraba, F. R. and Paine, S. H., "Empirical Formulae for Determining Thermal Neutron Flux Distributions in Finite Absorbing Cylinders," Nuc. Sci. & Engr. Suppl. 2 (1) 242-243 (June 1959).

Weil, Rolf, Rothman, Steven J., and Lloyd, Lowell T., "Preparation of Diffusion Couples by Cathodic Sputtering," Rev. Sci. Instr. 30 (7) 541-543 (July 1959).

Youngdahl, C. A. and DeBoer, F. E., "Analysis for Magnesium in High Purity Aluminum," Nature 184 54-55 (July 4, 1959).

Zegler, S. T. and Nevitt, M. V., "Some Properties of Uranium-Fissium Alloys," Nuc. Sci. & Engr. 6 (3) 222-228 (September 1959).

Reports

ANL-5364 Paine, S. H. and Brown, F. L., "Development of Remote Metallographic Equipment for the ANL Metallurgy Division," November 1959.

ANL-5372 Lloyd, L. T., "Recording Quartz Differential Dilatometer," July 1959.

ANL-5406 Kittel, J. H. and Paine, S. H., "Effects of High Burnup at Elevated Temperatures on Uranium-0.52 and 1.62 w/o Zirconium Alloys," August 1959.

ANL-5712 Kittel, J. H., "Preliminary Experiments on Irradiation Cycling and Partial Beta-Phase Irradiation of Uranium," April 1959.

ANL-5777 Chiswik, H. H. and Lloyd, L. T., "Some Aspects of the Beta to Alpha Transformation in Uranium: Metallographic Structure and Orientation Relationships," November 1959.

ANL-5861 Renken, C. J., Myers, R. G. and McGonnagle, W. J., "Status Report in Eddy Current Theory and Application," November 1958.

ANL-5872 Taraba, Frank R. and Paine, S. Hugh, "The Radial Distribution of Thermal Neutron Flux in Cylindrical Fuel Specimens During Neutron Irradiation," August 1, 1959.

ANL-5887 Mueller, M. H. and Knott, H. W., "Preferred Orientation in Rolled and in Recrystallized High-Purity Uranium Rod," April 1959.

ANL-5893 Beck, W. N., Renken, C. J., Myers, R. G., and McGonnagle, W.J., "Nondestructive Testing of EBR-I Mark III Fuel Elements and Components," May 1959.

ANL-5904 Brown, F. L., Paine, S. H., Fousek, R. J., and Armstrong, J.L., "An Automatic Polishing Machine for Remote Metallography," August 1959.

ANL-5927 Draley, J. E. and Ruther, W. E., "Corrosion Resistance and Mechanical Properties of Aluminum Powder Products," March 1959.

ANL-5935 Renken, C. J. and Myers, R. G., "A Double Pulse Eddy Current Testing System," June 1959.

ANL-5945 Taraba, F. R. and Paine, S. H., "The Longitudinal Distribution of Thermal Neutron Flux in Cylindrical Fuel Specimens During Irradiation," August 1959.

ANL-5951 McGonnagle, W. J., Beck, W. N., and Lapinski, N., "Inspection of Fuel Element Components and Fuel Elements for the Argonne Low Power Reactor," August 1959.

ANL-5958 Blumenthal, Bernhard, "Constitution of Low Carbon U-C Alloys," May 1959.

ANL-5966 Yario, W. R. and Lloyd, L. T., "Recrystallization of Heavily Cold-Rolled Uranium Sheet," May 1959.

ANL-5971 Rothman, S. J., Lloyd, L. T., Weil, R., and Harkness, A. L., "Self-Diffusion in Gamma Uranium," July 1959.

ANL-5972 Lloyd, L. T., "Thermal Expansion of Alpha-Uranium Single Crystals," June 1959.

ANL-5973 Carson, N. J., Jr., Morris, W. H., "Testing of Potential Bearing Materials in an Argon Atmosphere of Low Humidity," August 1959.

ANL-5988 Pokorny, George J. and Ayer, James E., "The Performance of a Special Differential Transformer and an Eddy Current Coil in a High Gamma Flux Environment," July 1959.

ANL-6001 Lloyd, L. T., "Recrystallization of Deformed Alpha-Uranium Single Crystals," July 1959.

ANL-6007 Dunworth, R. J. and Macherey, R. E., "Casting of a Uranium Shield for a Kilocurie Cobalt-60 Source," August 1959.

ANL-6015 Draley, J. E., Mori, S. and Loess, R. E., "Corrosion of 1100 Aluminum in Boiling H_2O and D_2O," July 1959.

ANL-6041 Beck, W. N., Kittel, J. H. and Brown, F. L., "Modification of CP-5 Fuel Assemblies for Fuel Capsule Irradiation Experiments," November 1959.

ANL-6048 Paine, S. H., Murphy, W. F. and Brown, F. L., "Examination of Jacketed Uranium Slugs from the Los Alamos Fast Reactor 'Clementine'," October 1959.

ANL-6053 Ruther, W. E. and Draley, J. E., "Corrosion of Aluminum-Uranium Alloys in High-Temperature Water," November 1959.

ANL-6059 Paine, S. H. and Murphy, W. F., "Examination of Irradiated Experimental NRU Fuel Rods," November 1959.

BNL-483 Kittel, J. H., "Effects of Irradiation on Thorium-Bearing Fuels," Thorium-U^{233} Symposium, January 9-10, 1958. p. 115 (December 1958).

Handwerk, J. H., "The Fabrication of Thoria and Thoria-Urania," pp. 113-114, ibid.

Schumar, J., "Fuel Preparation and Radiation Experience - Solid Fuels," pp. 189-190, ibid.

TID-7500 McGonnagle, W. J., "Gamma Counting for Measuring Uranium Content of Reactor Fuel Elements," Reactor Fuel Measurement Techniques Symposium, Michigan State University, Lansing, June 18-20, 1958. pp. 197-208 (January 1959).

TID-7559 (Pt. 1) McGonnagle, W. J., "Nondestructive Testing of Reactor Fuels," Fuel Element Conference Held at Gatlinburg, Tennessee, May 14-16, 1958. pp. 83-109 (August 1959).

Shuck, A. B., "Manufacturing Methods for the EBR, Mark I and Mark II Fuel Loadings," pp. 156-177, ibid.

Kittel, J. H. and Smith, K. F., "Irradiation Behavior of Uranium-Fissium and Uranium-Plutonium-Fissium Fast Reactor Fuels," pp. 203-212, ibid.

Noland, R. A., "Manufacture of Fuel Plates and Fuel Subassemblies for the Argonne Low-Power Reactor," pp. 233-244, ibid.

Kittel, J. H., "Irradiation Behavior of ThO_2-UO_2 Fuels," pp. 273-282, ibid.

Foote, F. G., "Fuels for Fast Breeder Reactors," pp. 290-291, ibid.

TID-7562 Noland, R. A. and Stone, C. C., "Welding of Uranium," Minutes of 7th Annual A.E.C. Welding Conference, Chicago, November 6-8, 1957. pp. 57-76 (1959).

Patents

Draley, J. E. and Ruther, W. E., "Nuclear Reactor Component Cladding Material," Patent No. 2,871,176 (1959).

Macherey, R. E., "Method of Working Beryllium," Patent No. 2,872,363 (1959).

Foote, F. G., "Thorium-Silicon-Beryllium Alloys," Patent No. 2,873,186 (1959).

VanThyne, R. J. and Smith, K. F., "Vanadium Alloys," Patent No. 2,886,431 (1959).

Walker, D. E. and Noland, R. A., "Method of Electropolishing Uranium," Patent No. 2,894,883 (1959).

Paine, S. H., "Jacketed Uranium Slugs and Method," Patent No. 2,894,889 (1959).

Zegler, S. T., "Method of Heat-Treating Uranium-Silicon Alloys, Patent No. 2,898,252 (1959).

Handwerk, J. H. and Bach, R. A., "Method of Preparing a Fuel Element for a Nuclear Reactor," Patent No. 2,900,263 (1959).

Noland, R. A. and Stone, C. C., "Method of Making Composite Fuel Elements," Patent No. 2,902,590 (1959).

Bean, C. H. and Macherey, R. E., "Method of Making Fuel Elements," Patent No. 2,915,815 (1959).